MULTISCALE MODELING OF CONJUGATED POLYMERS TOWARDS PREDICTING

THEIR MULTIFUNCTIONAL BEHAVIORS

A Dissertation
Submitted to the Graduate Faculty
of the
North Dakota State University
of Agriculture and Applied Science

By

Amirhadi Alesadi

In Partial Fulfillment of the Requirements
for the Degree of
DOCTOR OF PHILOSOPHY

Major Department:
Civil, Construction and Environmental Engineering

October 2022

Fargo, North Dakota

North Dakota State University
Graduate School

Title

MULTISCALE MODELING OF CONJUGATED POLYMERS
TOWARDS PREDICTING THEIR MULTIFUNCTIONAL BEHAVIORS

By

Amirhadi Alesadi

The Supervisory Committee certifies that this ***disquisition*** complies with North Dakota

State University's regulations and meets the accepted standards for the degree of

DOCTOR OF PHILOSOPHY

SUPERVISORY COMMITTEE:

Dr. Wenjie Xia

Chair

Dr. Dinesh Katti

Dr. Dmitri Kilin

Dr. Bakhtiyor Rasulev

Approved:

11/4/2022

Date

Dr. Xuefeng Chu

Department Chair

ABSTRACT

Easy processability, tunable mechanical and optoelectronic properties, and the endless possibilities of molecular modifications enable conjugated polymers (CPs) to be used in a wide range of lightweight, low-cost, and flexible organic electronic devices. However, despite the tremendous efforts in molecular engineering and improved electronic properties, the thermomechanical-structure-property relationship of these semiconducting materials is still less investigated. Predicting the thermal, mechanical, and photovoltaics (PV) properties of CPs is challenging due to heterogeneous chain architectures and diverse chemical building blocks. To address this critical issue, this dissertation aims to employ novel multiscale modeling and data-driven approaches to characterize the thermomechanical and optoelectronic properties of CPs. In particular, we utilize machine learning (ML) and scale-bridging molecular modeling techniques scaled from quantum mechanics simulations to force field all atomistic molecular dynamics (AA-MD) and coarse-grained (CG)-MD simulations to explore the multifunctional behavior of CPs. Validated by experimental measurements, our AA-MD and CG-MD simulations can capture glass transition temperature (T_g), elastic modulus, and strain-induced deformation mechanism of the CPs with varied side-chain lengths and backbone moieties. Furthermore, through the integration of ML, AA-MD simulations, and experiments, we propose a simplified but accurate predictive framework to quantify T_g directly from the geometry of the CPs' repeat unit. Next, first-principle calculations developed upon density functional theory (DFT) are utilized to quantify electronic configuration changes of CPs due to the charge injection. Finally, created upon *ab initio* excited state dynamics, we report a computational methodology to explore the PV performance of donor-acceptor organic bulk heterojunctions (BHJ). This computational framework facilitates screening of the best donor-acceptor molecules and narrows down the list of potential candidates to be used

in BHJ. We believe data-driven and multiscale modeling approaches established in this dissertation are important milestones for the design and structure-property prediction of CPs and organic BHJ, paving the way for developing the next generation of organic electronics.

DEDICATION

To the passengers of flight PS752.

To my loving parents Behrouz Alesadi and Parvin Amiri, who have sacrificed so much for me,
and without their love and support, none of this would have been possible.

To my wonderful wife, Sarah, for inspiration and loving support throughout this academic
journey.

TABLE OF CONTENTS

LIST OF TABLES

LIST OF FIGURES

LIST OF ABBREVIATIONS

AA..All-atomistic

AA-MD..All-atomistic molecular dynamics

AFM...Atomic force microscopy

BHJ ....Bulk heterojunction

CB ....Conduction band

CG..Coarse-grained

CG-MD ....Coarse-grained molecular dynamics

CP...Conjugated polymers

CT ....Charge transfer

D-A ....Donor-acceptor

DFT..Density functional theory

DMA ....Dynamic mechanical analysis

DPP ....Diketopyrrolopyrrole

DSC..Differential scanning calorimetry

DWF...Debye-Waller factor

FF ....Force field

GAFF ....General Amber force field

GET..Generalized entropy theory

HF ....Hartree-Fock

HOMO ....Highest occupied molecular orbital

HSE..Heyd-Scuseria-Ernzerhof

IR..Polarized Infrared

KS ....Kohn-Sham

LAMMPS...Large-scale atomic/molecular massively

LJ .... Lennard-Jones

LUMO .... Lowest unoccupied molecular orbital

MD .... Molecular dynamics

ML .... Machine learning

MSD .... Mean-squared displacement

NFA .... Non-fullerene acceptor

NPT .... Isothermal-Isobaric ensemble

NVT .... Canonical ensemble

P3HT .... Poly 3-hexylthiophene

PBC .... Periodic boundary conditions

PBE .... Perdew-Burke-Ernzerhof

PCE .... Power conversion efficiency

PV .... Photovoltaics

QSPR .... Quantitative structure-property relationships

T_g .... Glass transition temperature

VASP .... Vienna ab initio simulation package

VB .... Valence band

1. INTRODUCTION

1.1. Overview

Over the past decades, noticeable progress in performance-enhanced organic electronic devices such as organic photovoltaics (OPVs) and organic field-effect transistors (OFETs),[1–4] has been observed, rooted in the rapid development of conjugated polymers (CPs), especially recently emerged D-A type CPs.[5–8] CPs have drawn attention because of solution processability, structural tunability, good electrical performance, and mechanical compliance[9–15] compared to their inorganic counterparts (e.g., silicon). These semiconducting materials have shown great potential in developing next-generation electronics through molecular modification, for instance, soft and deformable CPs for wearable and biomedical devices[10,13] or thermal-stable CPs for automotive and aerospace industries.[16,17] However, a rational design of application-driven CPs requires the new fundamental knowledge of structure-property-morphology relationships to predict, control, and manipulate thermomechanics and optoelectronic properties of CPs. Due to the endless possibilities of molecular modifications, experimental measurement of the physical properties of any newly designed system is time-consuming, if not impossible.

To address this critical issue, multiscale modeling and data-driven approaches can be vital in developing material-by-design frameworks for CPs. To simulate the molecular structure of materials (e.g., polymer systems), two approaches can be utilized: classical Newtonian physical theories and quantum physics. The classical methods (e.g., force field molecular dynamics (FF-MD)) can simulate the polymer system at larger scales than quantum mechanics simulations. Indeed, the simpler physics theories used to describe these models and fewer degrees of freedom make them computationally efficient. These models are ideal for calculating polymers' thermomechanical and morphological properties.[18,19] However, classical physics models have no

understanding of the electronic structure of the materials and cannot simulate chemical reactions and any excited states. To address this and probe optoelectronic properties at the fundamental atomic level, first-principle calculations (i.e., quantum mechanics models) can play a vital role. These models are developed based on quantum physics principles and can provide an accurate and unbiased system representation. First-principle calculations provide beneficial insights into the fundamental electronic properties and PV performance of CPs.[20,21] However, developing first-principle methods requires enormous computational resources and can only be utilized to simulate small molecules.

Exploring the multifunctional behavior of complex chemical systems at different scales based on classical and quantum physics allows for acquiring the "best of both worlds," and can be a milestone in material discovery. The material community appreciates the importance of this computational methodology and awarded "The Nobel Prize in Chemistry 2013" to Martin Karplus, Michael Levitt, and Arieh Warshel for developing multiscale models of complex chemical systems.[22] Thus, this dissertation aims to utilize the aforementioned methods to explore the thermal, mechanical, dynamical, and optoelectronic properties of CPs. In the rest of this chapter, we will briefly review the utilization of multiscale modeling approaches in polymer discovery.

1.2. Force Field Molecular Dynamics

The past decade witnessed considerable computational efforts developed upon FF-MD that have been made to explore the fundamental roles of various molecular parameters in the complex behaviors of glassy polymers.[23–33] Generally, generic coarse-grained (CG)-MD models have been broadly utilized to probe structure-property relationships of polymers with different segmental structures qualitatively. Dudowicz and coworkers[24] explored the influence of the side chain length on the glass-transition behaviors of the branched polymers and found that increasing side-chain

length decreases glass transition temperature (T_g) of the polymer when a flexible side chain is grafted to a relatively stiff backbone. In a similar work, Chremos and Douglas[28] showed that the topological architecture has a significant impact on the self-diffusion coefficients of the polymer chains by comparing linear-chain and branched polymers having star, rings, and bottlebrush architectures. Moreover, several recent studies used CG-MD and have showed that the chain stiffness plays a significant role in influencing Young's modulus, relaxation dynamics, and glass-transition of polymers in which polymers with a higher backbone chain stiffness tend to exhibit lower dynamics and a higher T_g.[23,29] Similar trends in these properties were also observed for polymers with the same backbone chain but having different stiffness of the side chain at both bulk and nanoconfined states (e.g., thin films).[31,34–36]

However, despite those tremendous computational efforts on glassy polymers, effective CP-focused modeling approaches to predict the thermomechanical properties of these semiconducting materials have not yet been fully established. In the case of property calculations, all atomistic (AA)-MD simulations need to be developed. McMahon and coworkers[37] used AA-MD simulations to track and save the trajectory of the chain structures and then efficiently employed those conformations as input of first principle calculations to probe electronic structure, and study the effect of dynamic disorder on crystalline poly 3-hexylthiophene (P3HT). DuBay *et al.*[38] reparametrized OPLS force field for AA-MD simulations and showed an improved model to explore dihedral angle distributions, persistence lengths, and conjugation length distributions of poly[2-methoxy-5-(2′-ethylhexyloxy)-p-phenylene vinylene] (MEH-PPV) and P3HT systems. Another study was conducted by Lipomi group where AA-MD simulations were implemented to predict the nanoscale morphology and thermomechanical behavior of low-bandgap CPs and their blends with [6,6]-phenyl C_{71} butyric acid methyl ester (PCBM).[39] They calculated π-stacking

3

distances, T_g, and elastic modulus where the comparison to experimental measurements highlights the strength of MD simulations in determinization the role of molecular structure in morphology and mechanical properties of bulk heterojunction films. Despite these efforts on the studying multifunctional behavior of CPs, exploring segmental dynamics and thermomechanical behavior of the systems having different segmental structures still remains challenging, which is one of the main goals of this dissertation to be addressed.

1.3. Quantum Mechanics Simulations

For developing new functional materials, quantum mechanics is a powerful technique at the start point for targeted applications.[40] The physical laws employed in quantum simulations to describe the behavior of the materials are encapsulated in the Schrödinger equation.[41] However, a direct analytical solution to this equation is almost impossible for realistic materials due to the computing cost. To address this, density functional theory (DFT) was proposed by Hohenberg, Kohn, and Sham[42,43] which formulates the ground state solutions to the Schrödinger equation described as a problem of the charge density that must be minimized in energy. DFT models have provided accurate optoelectronic predictions in many classes of complex materials.[40]

DFT model have been broadly utilized to study the electronic configuration of diverse semiconducting polymers.[44–54] Yang and coworkers[55] showed that the DFT approach could properly estimate the band gap of the CPs having different molecular structures, where the hybrid functional indicated higher accuracy in predicting the energy gap. Zhang *et al.*[52] explored the band gap of different CPs, where the calculated theoretical band gaps show a good agreement with experimental data. Using time-dependent DFT (TD-DFT) models, the simulation successfully predicted the excitation energies and the maximal absorption wavelength of fluorene-based CPs,[56] in good agreement with experimental measurements. DFT and TD-DFT approaches with hybrid

4

functionals were also implemented to explore the doping process of the polypyrrole,[57] in which the computational results successfully predicted the experimental results. These recent studies confirm the applicability and strength of the DFT approach as a reliable computational approach to explore the design next generation of CPs. In this study, first-principle calculations developed upon DFT methods will be utilized to investigate the fundamental optoelectronic properties of newly designed CPs and the photovoltaic performance of organic bulk heterojunctions.

1.4. Machine Learning Methods

Developing high-performance materials using traditional trial-and-error methods relies on repetitive experimental and theoretical characterization approaches, which are often time-consuming and inefficient. To address this, a data-driven approach based on machine learning (ML) methods can be an efficient alternative.[58–60] Built upon molecular features obtained from first-principles calculations and experimental measurements, Tran and coworkers developed "Polymer Genome" as a web-based ML platform to provide near-instantaneous predictions of various polymer properties.[61] Although the model does not support network polymers, polymer blends, and copolymers yet, it opened up a pathway to approximate the properties of new polymers. In another work from the Ramprasad group,[62] ML methods based on genetic algorithm were employed to design polymers with targeted properties (i.e., high T_g and large bandgap). In CPs discovery, Nagasawa and coworkers conducted screening of conjugated molecules for organic photovoltaic (OPV) applications based on artificial neural network and random forest, where the model showed an improved accuracy for the power conversion efficiency classification.[63] Those successful implementation of ML models in the polymer discovery, mostly non-conjugated polymers, provokes the idea to develop predictive models for structure-properties relationship in

CPs. Thus, in this dissertation, we will propose a model which is supposed to predict T_g of CPs directly from chemical structure of building block.

1.5. Outlines

This dissertation aims to employ three different computational frameworks to investigate the thermomechanical and optoelectronic properties of CPs. AA-MD and CG-MD models are utilized to explore T_g, elastic modulus, deformation mechanism, and segmental dynamics. Then, based on a T_g dataset collected from experimental and computational measurements, a simplified ML model is developed to predict T_g directly from the chemical structure of the building block. Eventually, the DFT approach and ab initio dynamics are utilized to predict fundamental optoelectronic properties of CPs and characterize the photovoltaic performance of organic bulk heterojunctions. The rest of the dissertation is arranged as follows:

In Chapter 2, we review the multiscale molecular modeling methods used in this study. First, the basics of the FF-MD approach and details of utilized AA-MD and CG-MD simulations are reported. Then, the DFT approach and relevant computational details of first-principle simulations are reviewed. Chapter 3 aims to understand the glass-transition behavior of CPs based on experimental techniques and CG-MD simulations. In particular, we show how side chains and grafting density of the polymer chain influence T_g. In that chapter, using CG-MD simulations, the mobility of the polymer chains is studied to reveal further the origin of the role of the chain's chemical structure on T_g. In Chapter 4, we propose a simplified ML model to predict T_g directly from the chemical structure of the repeat unit. A diverse data set is utilized for training an ML model, collected from previously published literature, our collaborators' experimental measurements, and our AA-MD simulation calculations. Then, we use MD simulations to provide a physical interpretation of ML model outcomes. In the end, the predictive performance of the ML

model is examined by comparing the predicted values to our experimental and computational T_g measurements of novel high-performance CPs and acceptor units. In Chapter 5, we explore the mechanical properties and deformation mechanism of CPs. We utilize CG-MD simulations to examine the role of side chains in the mechanical performance (i.e., elastic modulus) of CPs and discuss our results in close comparison with experimental measurements. Then, we investigate how tensile deformation influences the chain alignment in polymer samples. Chapter 6 explores optoelectronic properties of diketopyrrolopyrrole (DPP)-based CPs via the DFT approach. First, fundamental electronic properties such as bandgap and absorption spectrum are calculated. Then, the influence of charge injection on the electronic configuration of the polymer system is studied. Finally, in Chapter 7, we report a computational framework to characterize photo-induced charge transfer of organic bulk heterojunctions via *ab initio* excited state dynamics. To this end, blends of DPP-based CP with non-fullerene (i.e., ITIC) and fullerene (i.e., PCBM) acceptor units are studied. That chapter aims to explore the possibility of having a computational framework to rank the photovoltaic performance of organic bulk heterojunctions to narrow down the list of potential donor-acceptor candidates. In Chapter 8, we summarize this study's key findings and present the dissertation's conclusion. Finally, we will further discuss promising paths in the areas mentioned above of research in the field of CPs and their multifunctional applications.

1.6. References

1. Yamashita, Y. *et al.* Mobility Exceeding 10 cm2/(V·s) in Donor-Acceptor Polymer Transistors with Band-like Charge Transport. *Chem. Mater.* **28**, 420–424 (2016).

2. Kim, G. *et al.* A thienoisoindigo-naphthalene polymer with ultrahigh mobility of 14.4 cm 2 /V·s that substantially exceeds benchmark values for amorphous silicon semiconductors. *J. Am. Chem. Soc.* **136**, 9477–9483 (2014).

3. Luo, C. *et al.* General strategy for self-assembly of highly oriented nanocrystalline semiconducting polymers with high mobility. *Nano Lett.* **14**, 2764–2771 (2014).

4. Meng, L. *et al.* Organic and solution-processed tandem solar cells with 17.3% efficiency. *Science (80-.).* **361**, 1094–1098 (2018).

5. Mei, J., Diao, Y., Appleton, A. L., Fang, L. & Bao, Z. Integrated materials design of organic semiconductors for field-effect transistors. *J. Am. Chem. Soc.* **135**, 6724–6746 (2013).

6. Sirringhaus, H. 25th anniversary article: Organic field-effect transistors: The path beyond amorphous silicon. *Adv. Mater.* **26**, 1319–1335 (2014).

7. Xue, X. *et al.* Oriented Liquid Crystalline Polymer Semiconductor Films with Large Ordered Domains. *ACS Appl. Mater. Interfaces* **7**, 26726–26734 (2015).

8. Gu, X., Shaw, L., Gu, K., Toney, M. F. & Bao, Z. The meniscus-guided deposition of semiconducting polymers. *Nat. Commun.* **9**, 534 (2018).

9. Root, S. E., Savagatrup, S., Printz, A. D., Rodriquez, D. & Lipomi, D. J. Mechanical Properties of Organic Semiconductors for Stretchable, Highly Flexible, and Mechanically Robust Electronics. *Chem. Rev.* **117**, 6467–6499 (2017).

10. Someya, T., Bao, Z. & Malliaras, G. G. The rise of plastic bioelectronics. *Nature* **540**, 379–385 (2016).

11.   Lipomi, D. J. & Bao, Z. Stretchable and ultraflexible organic electronics. *MRS Bull.* **42**, 93–97 (2017).

12.   Bao, Z. & Chen, X. Flexible and Stretchable Devices. *Adv. Mater.* **28**, 4177–4179 (2016).

13.   Oh, J. Y. & Bao, Z. Second Skin Enabled by Advanced Electronics. *Adv. Sci.* **6**, 1900186 (2019).

14.   Lipomi, D. J., Tee, B. C. K., Vosgueritchian, M. & Bao, Z. Stretchable organic solar cells. *Adv. Mater.* **23**, 1771–1775 (2011).

15.   Chortos, A., Liu, J. & Bao, Z. Pursuing prosthetic electronic skin. *Nat. Mater.* **15**, 937–950 (2016).

16.   Gumyusenge, A. *et al.* Semiconducting polymer blends that exhibit stable charge transport at high temperatures. *Science (80-.).* **362**, 1131–1134 (2018).

17.   Tran, D. T. *et al.* Effects of Side Chain on High Temperature Operation Stability of Conjugated Polymers. *ACS Appl. Polym. Mater.* acsapm.9b00999 (2019). doi:10.1021/acsapm.9b00999

18.   Alesadi, A. & Xia, W. Understanding the Role of Cohesive Interaction in Mechanical Behavior of a Glassy Polymer. *Macromolecules* **53**, 2754–2763 (2020).

19.   Zhang, S. *et al.* Toward the Prediction and Control of Glass Transition Temperature for Donor–Acceptor Polymers. *Adv. Funct. Mater.* **2002221**, 2002221 (2020).

20.   Alesadi, A., Fatima, F., Xia, W. & Kilin, D. First-Principles Study on the Electronic Properties of PDPP-Based Conjugated Polymer via Density Functional Theory. *J. Phys. Chem. B* **125**, 8953–8964 (2021).

21. Alesadi, A., Xia, W. & Kilin, D. Photo-Induced Charge Transfer of Fullerene and Non-Fullerene Conjugated Polymer Blends via Ab Initio Excited-State Dynamics. *J. Phys. Chem. C* **126**, 12015–12024 (2022).

22. Karplus, M. Development of multiscale models for complex chemical systems: from H+ H2 to biomolecules (Nobel lecture). *Angew. Chemie Int. Ed.* **53**, 9992–10005 (2014).

23. Dudowicz, J., Freed, K. F. & Douglas, J. F. Fragility of glass-forming polymer liquids. *J. Phys. Chem. B* **109**, 21350–21356 (2005).

24. Dudowicz, J., Freed, K. F. & Douglas, J. F. The glass transition temperature of polymer melts. *J. Phys. Chem. B* **109**, 21285–21292 (2005).

25. Xu, W. & Xia, W. Energy Renormalization for Coarse-Graining Polymers with Different Fragilities: Predictions from the Generalized Entropy Theory. *Macromol. Theory Simulations* 1900051 (2020).

26. Riggleman, R. A., Yoshimoto, K., Douglas, J. F. & de Pablo, J. J. Influence of confinement on the fragility of antiplasticized and pure polymer films. *Phys. Rev. Lett.* **97**, 45502 (2006).

27. Mangalara, J. H. & Simmons, D. S. Tuning polymer glass formation behavior and mechanical properties with oligomeric diluents of varying stiffness. *ACS Macro Lett.* **4**, 1134–1138 (2015).

28. Chremos, A. & Douglas, J. F. Influence of Branching on the Configurational and Dynamical Properties of Entangled Polymer Melts. *Polymers (Basel).* **11**, 1045 (2019).

29. Pan, D. & Sun, Z.-Y. Influence of chain stiffness on the dynamical heterogeneity and fragility of polymer melts. *J. Chem. Phys.* **149**, 234904 (2018).

30. Riggleman, R. A., Douglas, J. F. & de Pablo, J. J. Tuning polymer melt fragility with antiplasticizer additives. *J. Chem. Phys.* **126**, 234903 (2007).

31. Xie, S.-J., Qian, H.-J. & Lu, Z.-Y. The glass transition of polymers with different side-chain stiffness confined in free-standing thin films. *J. Chem. Phys.* **142**, 74902 (2015).

32. Delcambre, S. P., Riggleman, R. A., de Pablo, J. J. & Nealey, P. F. Mechanical properties of antiplasticized polymer nanostructures. *Soft Matter* **6**, 2475–2483 (2010).

33. Riggleman, R. A., Douglas, J. F. & de Pablo, J. J. Antiplasticization and the elastic properties of glass-forming polymer liquids. *Soft Matter* **6**, 292–304 (2010).

34. Santangelo, P. G. & Roland, C. M. Molecular weight dependence of fragility in polystyrene. *Macromolecules* **31**, 4581–4585 (1998).

35. Colucci, D. M. & McKenna, G. B. Fragility of polymeric liquids: correlations between thermodynamic and dynamic properties. *MRS Online Proc. Libr. Arch.* **455**, (1996).

36. Ngai, K. L. & Roland, C. M. Chemical structure and intermolecular cooperativity: dielectric relaxation results. *Macromolecules* **26**, 6824–6830 (1993).

37. McMahon, D. P. *et al.* Relation between microstructure and charge transport in polymers of different regioregularity. *J. Phys. Chem. C* **115**, 19386–19393 (2011).

38. DuBay, K. H. *et al.* Accurate force field development for modeling conjugated polymers. *J. Chem. Theory Comput.* **8**, 4556–4569 (2012).

39. Root, S. E., Jackson, N. E., Savagatrup, S., Arya, G. & Lipomi, D. J. Modelling the morphology and thermomechanical behaviour of low-bandgap conjugated polymers and bulk heterojunction films. *Energy Environ. Sci.* **10**, 558–569 (2017).

40. Jain, A., Shin, Y. & Persson, K. A. Computational predictions of energy materials using density functional theory. *Nat. Rev. Mater.* **1**, 1–13 (2016).

41. Schrödinger, E. An undulatory theory of the mechanics of atoms and molecules. *Phys. Rev.* **28**, 1049 (1926).

42. Kohn, W. & Sham, L. J. Self-consistent equations including exchange and correlation effects. *Phys. Rev.* **140**, A1133 (1965).

43. Hohenberg, P. & Kohn, W. Inhomogeneous electron gas. *Phys. Rev.* **136**, B864 (1964).

44. Siham, L., Bouchra, M., Latfa, L. & Ahmed, J. Electronic and photoelectronic properties of N-(5-indazolyl)-arylsulfonamides molecules: DFT/TD-DFT study. in *2020 IEEE 6th International Conference on Optimization and Applications (ICOA)* 1–6 (IEEE, 2020).

45. Vu, Q.-T. *et al.* DFT Prediction of Factors Affecting the Structural Characteristics, the Transition Temperature and the Electronic Density of Some New Conjugated Polymers. *Polymers (Basel).* **12**, 1207 (2020).

46. Kilina, S., Kilin, D. & Tretiak, S. Light-Driven and Phonon-Assisted Dynamics in Organic and Semiconductor Nanostructures. *Chem. Rev.* **115**, 5929–5978 (2015).

47. Vu, K. B. *et al.* Conjugated polymers: A systematic investigation of their electronic and geometric properties using density functional theory and semi-empirical methods. *Synth. Met.* **246**, 128–136 (2018).

48. Sun, H. & Autschbach, J. Electronic Energy Gaps for π-Conjugated Oligomers and Polymers Calculated with Density Functional Theory. *J. Chem. Theory Comput.* **10**, 1035–1047 (2014).

49. Mabrouk, A., Azazi, A. & Alimi, K. Molecular structure–property engineering of low-band-gap copolymers, based on fluorene, for efficient bulk heterojunction solar cells: A density functional theory study. *Polym. Eng. Sci.* **53**, 1040–1052 (2013).

50. Ferretti, A. *et al.* Ab initio complex band structure of conjugated polymers: Effects of hydrid density functional theory and GW schemes. *Phys. Rev. B* **85**, 235105 (2012).

51. Risko, C., McGehee, M. D. & Brédas, J.-L. A quantum-chemical perspective into low optical-gap polymers for highly-efficient organic solar cells. *Chem. Sci.* **2**, 1200–1218 (2011).

52. Zhang, L. *et al.* Calculation of band gap in long alkyl-substituted heterocyclic-thiophene-conjugated polymers with electron donor–acceptor fragment. *Sol. energy Mater. Sol. cells* **92**, 581–587 (2008).

53. Darling, S. B. Isolating the effect of torsional defects on mobility and band gap in conjugated polymers. *J. Phys. Chem. B* **112**, 8891–8895 (2008).

54. Gierschner, J., Cornil, J. & Egelhaaf, H. Optical bandgaps of π-conjugated organic materials at the polymer limit: experiment and theory. *Adv. Mater.* **19**, 173–191 (2007).

55. Yang, S., Olishevski, P. & Kertesz, M. Bandgap calculations for conjugated polymers. *Synth. Met.* **141**, 171–177 (2004).

56. Wang, J.-F. *et al.* Theoretical studies of the absorption and emission properties of the fluorene-based conjugated polymers. *Macromolecules* **37**, 3451–3458 (2004).

57. Ullah, H., Shah, A.-H. A., Bilal, S. & Ayub, K. Doping and dedoping processes of polypyrrole: DFT study with hybrid functionals. *J. Phys. Chem. C* **118**, 17819–17830 (2014).

58. Cai, J., Chu, X., Xu, K., Li, H. & Wei, J. Machine learning-driven new material discovery. *Nanoscale Adv.* **2**, 3115–3130 (2020).

59. Nantasenamat, C., Isarankura-Na-Ayudhya, C., Naenna, T. & Prachayasittikul, V. A practical overview of quantitative structure-activity relationship. (2009).

60. Liu, Y., Zhao, T., Ju, W. & Shi, S. Materials discovery and design using machine learning. *J. Mater.* **3**, 159–177 (2017).

61.   Doan Tran, H. *et al.* Machine-learning predictions of polymer properties with Polymer Genome. *J. Appl. Phys.* **128**, 171104 (2020).

62.   Kim, C., Batra, R., Chen, L., Tran, H. & Ramprasad, R. Polymer design using genetic algorithm and machine learning. *Comput. Mater. Sci.* **186**, 110067 (2021).

63.   Nagasawa, S., Al-Naamani, E. & Saeki, A. Computer-aided screening of conjugated polymers for organic solar cell: classification by random forest. *J. Phys. Chem. Lett.* **9**, 2639–2646 (2018).

2. MULTISCALE MOLECULAR MODELING FOR CONJUGATED POLYMERS

2.1. Introduction

The speed of technological innovations and demands for new materials is currently a tremendous challenge for the material engineering community due to the number of experimental procedures required to develop and examine any newly designed system. To address this critical issue, computer-aided molecular simulations can play a key role in boosting the materials' design process, particularly polymers. The emergence of high-speed computers facilities the utilization of molecular modeling approaches in different time and length scales based on physics and chemistry principles.[1] At the highest level of accuracy, first-principle *ab initio* calculations built upon theoretical principles and Schrodinger's equation can provide insight into the physical properties of materials at the fundamental electronic level.[2] However, these *ab initio* calculations are computationally expensive and are mainly aimed to explore fundamental optoelectronic properties at a limited time and length scale.[3]

One scale larger, all atomistic (AA) force field molecular dynamics (MD) simulations which are developed based on classical physics theories can increase computational efficiency by providing dramatically larger simulations length while preserving an acceptable level of accuracy.[4] These AA-MD models are wonderful choices to provide a quantitative investigation of the thermomechanical, morphological, and dynamical properties of polymer materials.[5] One step further, to improve the computational efficiency of AA-MD models and explore the systems at the larger time and length scales, simplified coarse-grained (CG) models are often required. CG models reduce the number of degrees of freedom by removing unessential structural features, while preserving the most essential atomic or molecular descriptors, such as segmental structure, shape and topology, and chemical interaction.[6–8] Thus, CG-MD approaches can play a vital role in

molecular modeling and simulations for the material science and engineering community. These largely simplified models are particularly appropriate to qualitatively explore the influence of different molecular parameters, such as cohesive energy or chain rigidity, on the physical behavior of polymers.[7,9–12]

This dissertation aims to employ scale-bridging computational approaches based on all the techniques mentioned above to understand the multifunctional behavior of conjugated polymers. First, we will use CG-MD and AA-MD force field simulations to probe the glass transition temperature, mechanical properties, and segmental dynamics of conjugated polymers. Then, at the fundamental electronic level, first-principle methods based on density functional theory (DFT) and *ab initio* excited-state dynamics will be implemented to investigate the optoelectronic properties and photovoltaic performance of these semiconducting materials. In the following sections, we will review the computational details of both force field and first-principle simulations.

2.2. Basics of Fore Field Molecular Dynamics Simulations

MD approaches are computer-aided simulation techniques to numerically solve the classical equations of motion, Newton's law, which for an atomic system is as follows:

$$m_i \frac{d^2 r_i}{dt^2} = f_i \quad \& \quad f_i = -\frac{\partial}{\partial r_i} U(r^N) \qquad i = 1, \dots, N \tag{1}$$

Here, f_i stands for the forces acting on the atoms, m_i is the atom mass, r_i is the position vector of atom i, and N is the number of atoms. $U(r^N)$ indicates the potential energy and depends on the position of the atoms in the system. Potential energy plays an essential role in MD simulations since forces are derived from the $U(r^N)$ as shown in equation (1). Determining the potential energy is the key difference between different force field methods. Then, one can solve the equation of motion by discretizing the equations in time. Many integration schemes are used in molecular dynamics for this purpose. The velocity Verlet Algorithm is one the most common methods which

have been performed to integrate Newton's equations of motion.[13] Through the Velocity Verlet

algorithm, positions are updated as follows:

$$r_i(t + \Delta t) = r_i(t) + v_i(t)\Delta t + \frac{1}{2}a_i(t)\Delta t^2 \tag{2}$$

where

$$v_i(t + \Delta t) = v_i(t) + \frac{1}{2}\big(a_i(t) + a_i(t + \Delta t)\big)\Delta t \tag{3}$$

This approach advances the coordinates and momenta over a timestep Δt.

2.2.1. All Atomistic Molecular Dynamics

For AA-MD simulations, we use the general Amber force field (GAFF), which is mainly

developed and parametrized for organic molecules composed of H, C, N, O, S, P, and halogens

atoms.[14] Utilizing GAFF, particular atom types are defined to describe specific chemical

environments accurately, such as conjugated single and double bonds, which is critically important

in the simulation of conjugated polymers. GAFF determines the total potential energy in the

following Hamiltonian:

$$E_{\text{total}} = \sum_{\text{bonds}} k_b(r - r_0)^2 + \sum_{\text{angles}} k_\theta(\theta - \theta_0)^2 +$$
$$\sum_{\text{dihedrals}} V_n[1 + \cos(n\phi - \gamma)] + \sum_{i>j}^{N}\left[\left(4\varepsilon_{ij}\left(\frac{\sigma_{ij}}{r_{ij}}\right)^{12} - \left(\frac{\sigma_{ij}}{r_{ij}}\right)^6\right) + \frac{1}{4\pi\varepsilon_0}\frac{q_i q_j}{r_{ij}}\right] \tag{4}$$

Here, k_b is force constant and r_0 stands for equilibrium bond length. Angle bending terms are then

parameterized by force constant k_θ in and an equilibrium angle value θ_0. The third term is the

usual Fourier-series expansion for torsional terms where V_n is the torsion barrier term, γ is the

phase angle, n is periodicity, and ϕ is the torsion angle. σ_{ij} and ε_{ij} are the Lennard-Jones

parameters and q_i and q_j are partial electronic charges. The Antechamber software from

AmberTools20[14] is used to perform GAFF atom typing, with the point charges derived through

the "gas" method. Then, a Matlab script converts GAFF topologies and coordinate files into the LAMMPS readable format.

2.2.1.1. All Atomistic Simulations Details

AA-MD simulations in this dissertation are carried out using the Large-scale Atomic/Molecular Massively Parallel Simulator (LAMMPS) software package.[15] The conjugated polymer models are initially built using Materials Studio software, followed by geometry optimization. Then, the Antechamber module of the AmberTools20 package[14] is employed for the atom typing and calculating atomic charges. To equilibrate the bulk systems, the total potential energy is first minimized using an iterative conjugate gradient algorithm,[16] followed by the equilibration of the bulk system under the isothermal-isobaric (NPT) ensemble at the melt state and then cooling down to the target temperature. An integration time step of $\Delta t = 1$ ns is implemented in all AA-MD simulations.

2.2.2. Generic Coarse-grained Molecular Dynamics

Generic CG-MD models can be effectively used for the simulation of polymers where the chemical structures of the molecules are simplified and represented by connecting a sequence of beads with springs.[17] In the case of conjugated polymers, generic CG-MD models can facilitate a parametric study on the influence of different molecular parameters, such as chain rigidity, grafting density, and cohesive energy, on the property of interest of conjugated polymers.

The force field components of the CG models are defined based on the contributions of the bonded and nonbonded interactions. To capture the nonbonded interactions, the standard 12-6 Lennard-Jones (LJ) potential function is utilized:

$$U_{\text{nonbonded}} = 4\varepsilon \left[\left(\frac{\sigma}{r}\right)^{12} - \left(\frac{\sigma}{r}\right)^{6} \right] \quad r < r_c \tag{5}$$

where σ and ε represent the units of energy and length, and the cutoff distance is $r_c = 2.5\sigma$. The cohesive interaction between CG beads is controlled via ε parameter, where for each pair of the CG beads in the backbones $\varepsilon = 1.0$, and the pairs of chain branching sites and pairs of the side-chains $\varepsilon = 0.5$. All quantities in CG modeling are expressed in reduced (or LJ) units. The potential energy of the bond stretching is defined through a harmonic bonding potential $U_{bond}(r) = k_b(r - r_0)^2$ where $r_0 = 0.99 \sigma$ is the equilibrium bond length and $k = 2500 \ \varepsilon/\sigma^2$ is the stiffness constant, which is consistent with previously investigated branched polymers.[18] The angular potential function, which controls the stiffness of the backbone and side chain, is defined via the cosine function $U_{angle}(\theta) = k_\theta[1 + cos(\theta)]$ where K_θ is the angular stiffness constant. For the angles in the backbone, the angular stiffness constant is $k_\theta = 1.0 \ \varepsilon$, for the angles between chain branching sites and backbone beads $k_\theta = 0.5 \ \varepsilon$ and for the angles in the side-chains $Kk_\theta = 0.2 \ \varepsilon$. All CG-MD simulations of the bulk polymer are performed using LAMMPS. The bulk systems of all models with different grafting densities consist of 100 chains, where the backbone of each chain is composed of 20 CG beads. All beads of the polymer chain are assumed to have the same mass m. Periodic boundary conditions (PBC) are applied in all three directions. An integration time step $\Delta t = 0.005\tau$ where $\tau = \sigma(m/\varepsilon)^{1/2}$ is implemented in all the simulations. To equilibrate the system, the total potential energy is first minimized using an iterative conjugate gradient algorithm.[16] Then, the equilibration of the bulk system is continued at the melt state at a high-temperature $T = 2.0$ under isothermal-isobaric (NPT) ensemble for the 10^6 time steps with the pressure ramp from the initial 10 to the final 5 in reduced units. Later, the system is further cooled down to the desired temperature with zero pressure for 1.5×10^6 time steps via the NPT ensemble before running for any property calculations.

For the sake of convenience, in the generic CG models, all quantities are often reported in reduced LJ units. For this reduced style, fundamental quantities mass (m), ε, σ, and Boltzmann constant k_B are set to the unit. The masses, distances, and energies are multiples of these fundamental values. Temperature is defined in units of ε/k_B, and time has the unit of $\left(\frac{m\sigma^2}{\varepsilon}\right)^{1/2}$. It should be noted that these reduced units can be transformed into laboratory measurements on units relevant to real materials.[19]

2.3. First-principle Simulations

The application of first-principle approaches, particularly DFT calculations, is rapidly growing for diverse materials modeling problems in materials science and engineering.[20] DFT has become a successful and efficient numerical approach for solving the Schrödinger equation that describes the quantum behavior of atoms and molecules. In this dissertation, the atomic models of quantum simulations are defined by the initial positions of each ion, $\vec{R}_I$. The electronic structure is calculated through the solution of self-consistent equation of DFT[21] via Vienna Ab initio Simulation Package (VASP).[22] This approach is developed based on a fictitious one-electron Kohn-Sham (KS) equation:

$$\left(-\frac{\hbar^2}{2m}(\nabla - \vec{k})^2 + 1/[\vec{r} - \vec{R}_I] + v[\vec{r}, \rho(\vec{r})]\right)\varphi_{i,\vec{k}}^{KS}(\vec{r}) = \varepsilon_{i,\vec{k}}\,\varphi_{i,\vec{k}}^{KS}(\vec{r}) \tag{6}$$

where $\rho(\vec{r})$ stands for electronic charge distribution, and $\varphi_{i,\vec{k}}^{KS}(\vec{r})$ are electronic states. The solutions of the Kohn-Sham equations are single-electron KS orbitals that depend on three spatial variables $\varphi_{i,\vec{k}}^{KS}(\vec{r})$. It should be noted that $\vec{k}$ indicates momentum sampling for those models that sampling is performed. Then, the solution of equation (6) is a set of one-electron momentum-dependent orbitals:

$$\varphi_{i,\vec{k}}^{KS}(\vec{r}) = e^{i\vec{k}.\vec{r}} \sum_{|\vec{G}| \leq \vec{G}_{cut}} C_{\vec{G},i,\vec{k}} \, e^{i\vec{G}.\vec{r}} \tag{7}$$

where $\vec{G}$ is reciprocal lattice vectors and $\vec{G}_{cut}$ stands for a cutoff sphere in reciprocal space. The total density of electrons has calculated the combination of the orbitals and the orbital occupation function $f_{i,\vec{k}}$.

$$\rho(\vec{r}) = \sum_{i,j,\vec{k},\vec{k'}} \rho_{i,j,\vec{k},\vec{k'}}^{eq} \varphi_{i,\vec{k}}^{KS^*}(\vec{r}) \varphi_{j,\vec{k'}}^{KS}(\vec{r}) \tag{8}$$

$$\rho_{i,j,\vec{k},\vec{k'}}^{eq} = \delta_{kk'} \delta_{ij} f_{i,\vec{k}} \tag{9}$$

$$f_{i,\vec{k}} = \begin{cases} 1 & i \leq HOMO(\vec{k}) \\ 0 & i \geq LUMO(\vec{k}) \end{cases} \tag{10}$$

where HOMO and LUMO stand for highest occupied molecular orbital and lowest unoccupied molecular orbital, respectively. Then, the total density provides the potential:

$$v[\vec{r}, \rho] = {}^{\delta}\!/\!_{\delta\rho} (E_o^{tot}[\rho] - T[\rho]) \tag{11}$$

The potential is described as a functional derivative of total energy to the variation of total density, which includes interactions of electrons with ions as well as three electron interactions as Coulomb, correlation, and exchange. In the case of hybrid functionals, The HSE functional benefits from the fraction of Fock exchange, a, at zero electron separation and a length scale, $1/\omega$, where the short-range Fock exchange is calculated as follows:

$$E_{XC}^{HSE} = aE_{XC}^{HF,SR}(\omega) + (1-a)E_X^{PBE,SR}(\omega) + E_X^{PBE,LR}(\omega) + E_X^{PBE} \tag{12}$$

The short-range Fock exchange is then computed via the spinful Kohn-Sham density matrix $\rho_{\sigma,\sigma'}(r,r')$:[23]

$$E_{XC}^{HF,SR}(\omega) = -\frac{1}{2} \sum_{\sigma,\sigma'} \int dr dr' \frac{\text{erfc}(\omega|r-r'|)}{|r-r'|} \times |\rho_{\sigma,\sigma'}(r,r')|^2 \tag{13}$$

while the long-range and remaining short-range exchange are determined from the exchange-hole formulation of PBE functionals.[24]

2.3.1. Ground State Observables

Momentum dispersion is presented as $\varepsilon_i(\vec{k})$ which is considered in z-direction of polymer model. The partial density of states for a given momentum $\vec{k}$ is computed as follow:

$$D_{\vec{k}}(\varepsilon) = \sum_i \delta\left(\varepsilon - \varepsilon_{i,\vec{k}}\right) \tag{14}$$

where $\varepsilon_{i,\vec{k}}$ represent the energy of a given orbital, and the index i runs overall calculated bands.

The Dirac delta function $\delta(\varepsilon - \varepsilon_{i,\vec{k}})$ is modeled using a Lorentzian $\delta(x) = \frac{1}{\pi}\frac{\sigma}{\sigma^2+x^2}$.

In the case of spin polarization (SP) DFT calculations, in addition to summations over bands, additional summations over spin up α and spin down β alignment should be considered.

$$D_{SP}(\varepsilon) = \sum_{i,\sigma} \delta\left(\varepsilon - \varepsilon_{i,\sigma}^{SP}\right) \tag{15}$$

The Dirac delta function is approximated as a Gaussian distribution to capture the thermal broadening.

The calculation of the absorption spectrum is based on the independent orbital approximation IOA, in which the optical property of the model is defined by matrix elements of electron-to-electron interaction on the basis of auxiliary Kohn-Sham orbitals.[25,26] Lowest energy peak of the computed absorption spectrum is an appropriate quantitative measure of the conductivity since they include the matrix element of the momentum.[27] The absorption spectrum of the current polymer model is calculated based on the consideration of momentum conservation $\Delta\vec{k} = 0$ via the following equation:

$$\alpha(\omega) = \sum_{\vec{k}} \alpha_{\vec{k}}(\omega) \tag{16}$$

which were formulated as the summation of partial spectra at a given value of momentum k.

$$\alpha_{\vec{k}}(\omega) = \sum_{ij} f_{ij,\vec{k}} \, \delta(\hbar\omega - |\varepsilon_{i,\vec{k}} - \varepsilon_{j,\vec{k}}|) \tag{17}$$

22

where $f_{ij,\vec{k}}$ is the oscillator strength between state i and j;

$$f_{ij,\vec{k}} = \frac{4\pi m_e \omega_{ij,\vec{k}}}{3he^2} \, |\vec{D}_{ij,\vec{k}}|^2 \tag{18}$$

and for a given value of $\vec{k}$ vector, $< \vec{D}_{ij,\vec{k}} >$ stands for the transition dipole moment.

$$< \vec{D}_{ij,k} > = \int \varphi_{i,\vec{k}}^{KS} \vec{r} \, \varphi_{j,\vec{k}}^{KS} d\vec{r} \tag{19}$$

The probability of electronic transition between states i and j, corresponding to the angular frequency ω of the incident light, implies the oscillator strength. The transition dipole correlates the spatial overlap between the pair of electronic states i and j and provides the matrix elements of the position operator. The delta function in equation (17) is approximated as a Lorentzian distribution to account for thermal fluctuations.

2.4. References

1. Ercolessi, F. A molecular dynamics primer. *Spring Coll. Comput. physics, ICTP, Trieste* **19**, (1997).

2. Marx, D. & Hutter, J. Ab initio molecular dynamics: basic theory and advanced methods. (2009).

3. Alesadi, A., Fatima, F., Xia, W. & Kilin, D. First-Principles Study on the Electronic Properties of PDPP-Based Conjugated Polymer via Density Functional Theory. *J. Phys. Chem. B* **125**, 8953–8964 (2021).

4. Salomon-Ferrer, R., Gotz, A. W., Poole, D., Le Grand, S. & Walker, R. C. Routine microsecond molecular dynamics simulations with AMBER on GPUs. 2. Explicit solvent particle mesh Ewald. *J. Chem. Theory Comput.* **9**, 3878–3888 (2013).

5. Alesadi, A. *et al.* Machine learning prediction of glass transition temperature of conjugated polymers from chemical structure. *Cell Reports Phys. Sci.* 100911 (2022).

6. Xia, W. *et al.* Energy-renormalization for achieving temperature transferable coarse-graining of polymer dynamics. *Macromolecules* **50**, 8787–8796 (2017).

7. Alesadi, A. & Xia, W. Understanding the Role of Cohesive Interaction in Mechanical Behavior of a Glassy Polymer. *Macromolecules* **53**, 2754–2763 (2020).

8. Xia, W. *et al.* Energy renormalization for coarse-graining polymers having different segmental structures. *Sci. Adv.* **5**, eaav4683 (2019).

9. Riggleman, R. A., Douglas, J. F. & de Pablo, J. J. Tuning polymer melt fragility with antiplasticizer additives. *J. Chem. Phys.* **126**, 234903 (2007).

10. Riggleman, R. A., Yoshimoto, K., Douglas, J. F. & de Pablo, J. J. Influence of confinement on the fragility of antiplasticized and pure polymer films. *Phys. Rev. Lett.* **97**, 45502 (2006).

11. Xu, W.-S. & Freed, K. F. Influence of cohesive energy and chain stiffness on polymer glass formation. *Macromolecules* **47**, 6990–6997 (2014).

12. Xu, W.-S. S., Douglas, J. F. & Freed, K. F. Influence of cohesive energy on relaxation in a model glass-forming polymer melt. *Macromolecules* **49**, 8355–8370 (2016).

13. Verlet, L. Computer" experiments" on classical fluids. I. Thermodynamical properties of Lennard-Jones molecules. *Phys. Rev.* **159**, 98 (1967).

14. Wang, J., Wolf, R. M., Caldwell, J. W., Kollman, P. A. & Case, D. A. Development and testing of a general Amber force field. *J. Comput. Chem.* **25**, 1157–1174 (2004).

15. Plimpton, S. Fast parallel algorithms for short-range molecular dynamics. *J. Comput. Phys.* **117**, 1–19 (1995).

16. Payne, M. C., Teter, M. P., Allan, D. C., Arias, T. A. & Joannopoulos, ad J. D. Iterative minimization techniques for ab initio total-energy calculations: molecular dynamics and conjugate gradients. *Rev. Mod. Phys.* **64**, 1045 (1992).

17. Kremer, K. & Grest, G. S. Dynamics of entangled linear polymer melts: A molecular-dynamics simulation. *J. Chem. Phys.* **92**, 5057–5086 (1990).

18. Chremos, A. & Douglas, J. F. A comparative study of thermodynamic, conformational, and structural properties of bottlebrush with star and ring polymer melts. *J. Chem. Phys.* **149**, 44904 (2018).

19. Cheng, S. & Robbins, M. O. Capillary adhesion at the nanometer scale. *Phys. Rev. E - Stat. Nonlinear, Soft Matter Phys.* **89**, 1–14 (2014).

20. Sholl, D. & Steckel, J. A. *Density functional theory: a practical introduction*. (John Wiley & Sons, 2011).

21. Hohenberg, P. & Kohn, W. Inhomogeneous electron gas physical review 136. *B864* (1964).

22. Kresse, G. & Furthmüller, J. Efficient iterative schemes for ab initio total-energy calculations using a plane-wave basis set. *Phys. Rev. B* **54**, 11169 (1996).

23. Moussa, J. E., Schultz, P. A. & Chelikowsky, J. R. Analysis of the Heyd-Scuseria-Ernzerhof density functional parameter space. *J. Chem. Phys.* **136**, 204117 (2012).

24. Perdew, J. P., Burke, K. & Ernzerhof, M. Generalized gradient approximation made simple. *Phys. Rev. Lett.* **77**, 3865 (1996).

25. Vogel, D. J., Kryjevski, A., Inerbaev, T. & Kilin, D. S. Photoinduced single-and multiple-electron dynamics processes enhanced by quantum confinement in lead halide perovskite quantum dots. *J. Phys. Chem. Lett.* **8**, 3032–3039 (2017).

26. Han, Y. *et al.* Photoinduced Charge Transfer versus Fragmentation Pathways in Lanthanum Cyclopentadienyl Complexes. *J. Chem. Theory Comput.* **8**, 4281–4296 (2017).

27. Kilin, D. S., Tsemekhman, K. L., Kilina, S. V, Balatsky, A. V & Prezhdo, O. V. Photoinduced Conductivity of a Porphyrin− Gold Composite Nanowire. *J. Phys. Chem. A* **113**, 4549–4556 (2009).

3. UNDERSTANDING THE GLASS-TRANSITION BEHAVIOR OF CONJUGATED POLYMERS

Semiconducting donor-acceptor (D-A) conjugated polymers (CPs) have attracted considerable attention in organic electronic and optoelectronic devices. However, a rational design rule for making CPs with desired physical behavior is currently lacking, which greatly limits the development of new polymers for advanced applications. A fundamental property that determines applications of CPs is glass transition temperature (T_g) which is still unknown for many newly designed CPs. Despite the obvious importance of glass-transition behavior, it is generally not well understood. In this chapter, with the help of our experimental collaborators, we first systematically design polydiketopyrrolopyrrole (PDPP)-based D-A polymers with varied alkyl side-chain lengths and backbone moieties. Then, experimental and computational measurements are developed to explore the influence of the side-chain length and grafting density on T_g of CPs.[1]

3.1. Introduction

Past decades have witnessed remarkable progress for performance-enhanced organic electronic devices like organic photovoltaics (OPVs) and organic field-effect transistors (OFETs),[2–5] owing to the rapid development of conjugated polymers (CPs), especially recently emerged D-A type CPs.[6–9] When compared with their inorganic counterparts (e.g., silicon), CPs exhibit solution processability, structural tunability, good electrical performance and mechanical compliance.[10–16] Thus, these semiconducting systems have shown great promise in next-generation electronics through molecular-level engineering, i.e., soft and deformable CPs for wearable and biomedical devices;[11,14] thermal-stable CPs for automotive and aerospace industries.[17,18] A rational design of application-driven CPs requires the new fundamental knowledge to predict, control and manipulate thermomechanical properties of D-A CPs.

Glass transition temperature, or T_g, is an important parameter that characterizes the onset of polymer chain motions. The determination of T_g for a polymer is vital for understanding and controlling its thermal and mechanical responses. However, the T_g for D-A CPs is hard to detect due to two main reasons. First, only a limited amount of samples (~ 100 mg) is available for a single batch of polymer because of synthetic challenges, making a bulk test difficult to perform using oscillatory shear rheometry,[19–21], and dynamic mechanical analysis (DMA).[22,23] Typically, a modified DMA test is applied where drop-casting polymer solutions prepare the sample onto a glass fiber mesh. Secondly, the semicrystalline nature and rigid polymer backbone of D-A CPs lead to negligible changes in specific heat capacity (ΔC_p) during glass transition, and thus a normal differential scanning calorimetry (DSC) test can hardly detect the backbone T_g.[24,25] To overcome this issue, alternating current (AC)-chip calorimetry[19,20] and fast-scanning DSC[26,27] are applied to determine the T_g of a thin film sample through high-frequency scan and heating/cooling rate, respectively.

Past efforts on the backbone/side-chain engineering of CPs have demonstrated a qualitative relationship between the polymer structure and the thermal/mechanical properties of CP thin films: stiffer backbones and shorter alkyl side-chains increase both the elastic modulus and T_g of polymers.[10,28–30] With the increased number of isolated thiophene units in the backbone of PDPP-based polymers, i.e., from PDPP-T to PDPP-T2 and PDPP-T3, a constant increase in the elastic modulus from 173 to 281 and 319 MPa has been observed from pseudo-free standing tensile test. Their corresponding T_g also rises from -3.96 to 11.95 and 18.98 °C, as tested by DMA.[28] For side-chain engineered isoindigo-based polymers, a steady decrease of elastic modulus from 550 to 250 MPa with increasing alkyl side-chain lengths from C6 to C10 is determined by AFM measurement.[29] Similarly, polyalkylthiophenes (P3ATs) with increasing alkyl side-chain lengths

have shown lower elastic modulus and T_g, as measured by buckling metrology and DSC, respectively.[30] Such a trend is also demonstrated by a modified coarse-grained model through comparing P3NT (poly(3-nonylthiophene-2,5-diyl))and P3DDT (poly(3-dodecylthiophene-2,5-diyl)), where a reduction in the predicted elastic modulus value from 990 to 780 MPa, and T_g value from 7 °C to -15 °C is shown.[31] Most recent work by Xie *et.al.* shows a simple linear predictive model by connecting the ratio of mobility between conjugated and non-conjugated atoms to CPs' T_g, while the effect of side-chain length on the polymer backbone T_g is not clearly captured.[21] Thus, a quantitative model is in need to predict the thermal and mechanical performances for D-A CPs with various side-chain structures.

Herein, we build a general relationship between the side-chain length, chain flexibility, and T_g to serve for the rational design of new D-A CPs and predict their glass-transition behavior. The PDPP-based D-A CP is utilized for demonstration due to its high charge mobility.[32] In addition, coarse-grained molecular dynamics simulations (CG-MD) are utilized to explore further the influence of the segmental structure of D-A CPs on the T_g at the fundamental molecular level. In particular, coarse-graining provides much improved computational efficiency to study influences of fundamental molecular parameters on the thermomechanical properties of polymers by removing unessential atomistic features of all-atomistic (AA) structures.[33–35]

Both experimental and computational results show a two-stage reduction T_g with increasing side-chain length: a rapid near-linear reduction followed by a slowly plateaued region. Next, an empirical mass-per-flexible bond model is proposed to connect the side-chain length to the flexibility of the entire polymer chain, where a linear T_g evolution with increasing chain flexibility is observed. Moreover, a backbone-engineered PDPP-based polymer is designed to elevate the backbone T_g, which verifies the observed side-chain length effect and the generality of

this model. Furthermore, the grafting density effect on T_g is investigated to shed light on the importance of side-chain weight fraction on polymer T_g. This work demonstrates the efficacy of the new model in precisely controlling the T_g and of PDPP polymers, and provides a rational way to tailor the performance of CPs for their desired applications.

3.2. Methods

3.2.1. Overview of CG-MD Simulations

The simulation details of CG-MD models are reported in Chapter 2, in which all simulations are performed via the LAMMPS software package.[36] The bulk systems of all models with different grafting densities consist of 100 chains, with the backbone of each chain composed of 20 CG beads. All beads of the polymer chain are assumed to have the same mass m. Periodic boundary conditions (PBC) are applied in all three directions. To measure the T_g of the polymer bulk, the simulation is run further under NPT ensemble with zero pressure for a wide range of the temperature. Then, the density of the bulk model is plotted versus the temperature, which exhibits two linear regimes, and the intersection point of these two lines marks the T_g.

3.2.2. Dynamic Mechanical Analysis (DMA)

A TA Q800 DMA is used to perform DMA measurements by a modified DMA method. Polymer solutions (5 mg/ml) are made and then drop-casted on top of a glass fiber mesh to prepare the samples.[22] The temperature corresponding to the peak of tan δ is determined as the backbone T_g. In strain-controlled mode, temperature ramp experiments are performed at a temperature range of -110 to $150\,°C$ and a heating rate of $3\,°C$/min with a fixed frequency of 1 Hz. The strain imposed is in the linear regime.

3.2.3. Grazing Incidence Wide-angle X-Ray Scattering (GIWAXS)

GIWAXS experiments are performed on beamline 11–3 at the Stanford Synchrotron Radiation Lightsource. Data are collected under helium environment with an incident beam energy at 12.7 keV and an incidence angle of 0.12°. The sample to detector distance is about 300 mm. Diffraction data analysis is performed using the Nika software package for Wavemetrics Igor, in combination with WAXStools.[37,38]

3.3. Results and Discussions

3.3.1. Molecular Design

In this study, we first aim to achieve fine-tuned thermal performance for D-A CPs through side-chain engineering. Four diketopyrrolopyrrole (PDPP)-based polymers are synthesized with systematically increased side-chain lengths from C2C6C8 (2-hexyl decyl) to C2C8C10 (2-octyl dodecyl), C2C10C12 (2-decyl tetradecyl) to C2C12C14 (2-dodecyl hexadecyl) on the DPP core (Figure 3.1A). Next, the side-chain effect on their thermal and performance is carefully investigated experimentally. To verify the experimental results and gain more insights, CG-MD simulation is employed to probe how side-chain length (M) and grafting density (f) influence T_g. Informed from the experiment, a generic bead-spring CG model is employed to preserve the essential structural features of the D-A CPs. Specifically, the CG model of each CP consists of three main components, a linear backbone chain (grey beads), a side-chain branching site (purple beads), and two side chains connecting the branching site to represent alkyl groups (cyan beads) per grafting (Figure 3.1B). Specifically, the side-chain length M is represented by the number of cyan beads, and grafting density f is determined by the following equation:

$$f = \text{number of grafted backbone beads / total number of backbone beads} \qquad (20)$$

Figure 3.1B and C show the snapshots of the polymer chain and the simulation box of the CG polymer model, respectively.
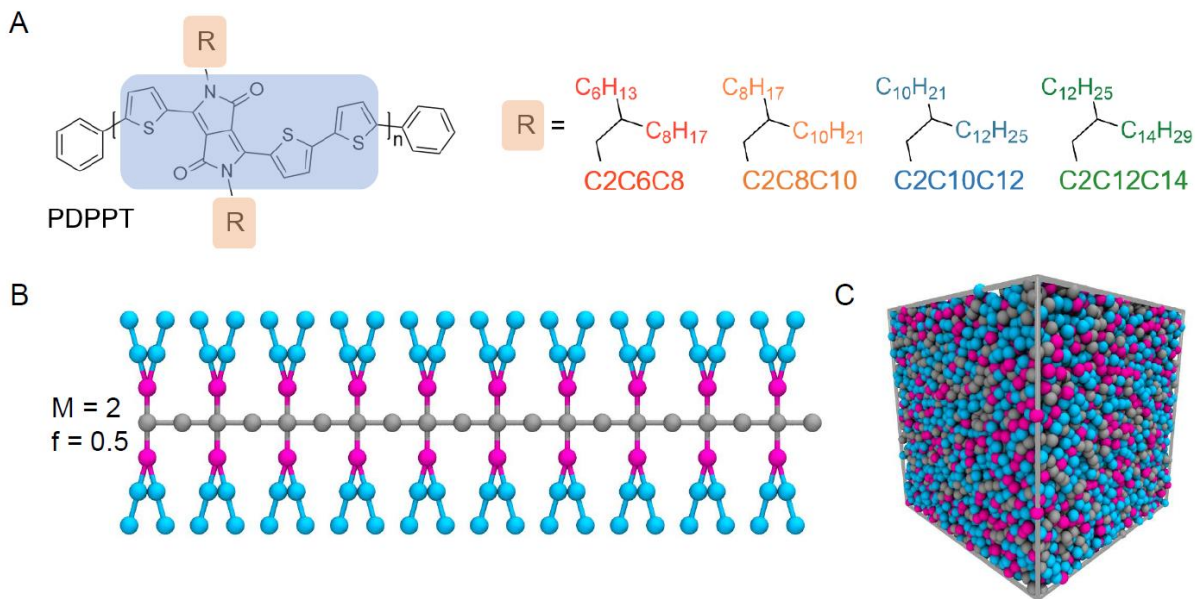
Figure 3.1. Molecular structure and computational molecular model of PDPPT-based polymers. (A) Chemicals structures of PDPPT-based conjugated polymers. R represents the side-chain groups attached to the DPP core. (B) The geometrical configuration of simulated polymers with and without branched side chains. The backbone of all chains is composed of 20 beads (shown in gray). M represents the number of simulated branched side-chain lengths (shown in blue). f represents the grafting density (the branching position is shown in red). (C) A snapshot of a coarse-grained model of the bulk polymer system.

3.3.2. Thermal Measurements

Firstly, a differential scanning calorimetry (DSC) is utilized to detect the difference in their thermal responses, where the T_g is not evident due to their rigid polymer backbones and insufficient cooling rate, while the melting temperature (T_m) shows a reduction with increasing side-chain length.[24] Such a trend is expected due to the increased weight fraction of low-T_g side chains in the polymer. Next, a substrate-supported DMA method is utilized to measure polymer T_g followed by previously reported procedures.[22,28,39] The glass transition information is extracted from a tan δ curve, where the main peak close to 0 °C corresponds to backbone relaxation and the peak shoulder

at around -40 °C represents side-chain T_g (Figure 3.2A).[22,28] It is observed that the backbone T_g decreases with increasing side-chain length, from 1.88 °C (PDPPT-C2C6C8), to -6.53 °C (PDPPT-C2C8C10), -10.31 °C (PDPPT-C2C10C12), and -13.26 °C (PDPPT-C2C12C14). Furthermore, an alternating current (AC)-chip calorimetry is applied to measure thin film (around 80 nm) T_g, where the same trend is observed despite different T_g values. This can be attributed to the technique difference and potential confinement effect on T_g measurement between different approaches.[19,40]
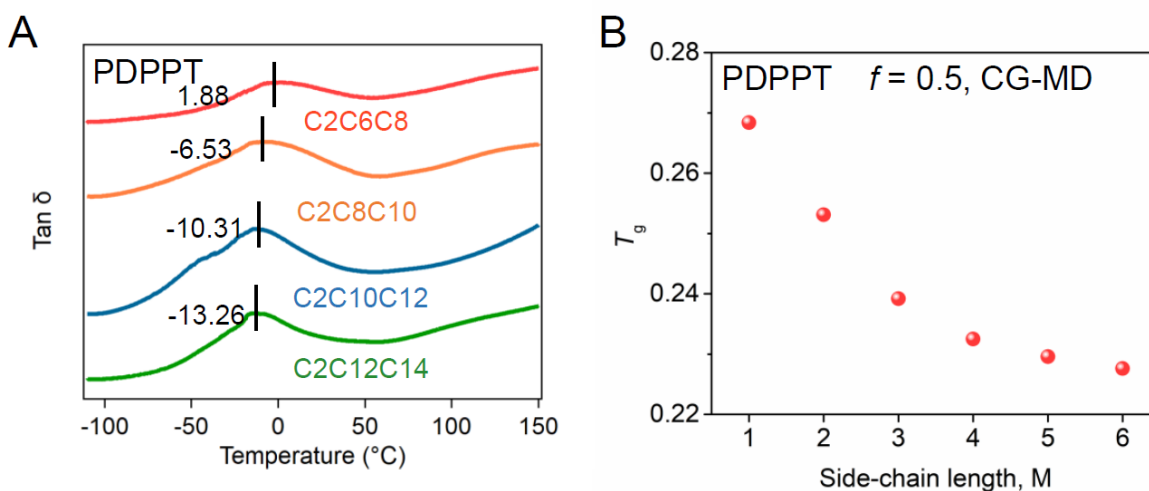
Figure 3.2. Experimental and simulation results of the thermal and mechanical properties based on PDPP-T polymers with various side-chain lengths. (A) Tan δ versus temperature curves extracted from DMA. (B) Simulated T_g versus side-chain length M. Coarse-grained molecular dynamics (CG-MD) simulation results are expressed using the reduced or (LJ) unit.

3.3.3. Molecular Dynamics Simulations

Next, we utilize CG-MD simulation to study systematically T_g of D-A CPs. As discussed from experimental results, side-chain groups are found to affect the thermal behaviors of polymers considerably. To gain more insights, CG-MD simulations are carried out to investigate the PDPPT models having a grafting density f of 0.5 and side-chain length varying from $M = 1$ to 6 (Figure 3.1B). Figure 3.2B indicates that the growth of the side-chain length M leads to a sharp decrease

in T_g of the bulk polymers. For polymer models with a side-chain length $M > 3$, T_g of the bulk model tends to reach a plateau – in other words, the reduction rate of T_g decreases with increasing M. These results obtained from CG-MD verify the experimental findings, demonstrating that the larger side-chain length leads to a more significant reduction in T_g.

Previous studies have explored the influence of segmental structure and side-chain groups on the glass formation of the polymers, such as mechanical properties, relaxation time, fragility and T_g.[35,41–49] Using the generalized entropy theory (GET), Dudowicz and coworkers[45] have predicted that the stiffnesses of side-chain groups and chain backbone can strongly impact the T_g as well as other characteristic temperatures associated with glass formation of the polymer. For polymers with a flexible backbone and stiff side-chain, the growth of side-chain length is found to increase T_g. However, when flexible side-chains are grafted to relatively stiffer backbones, increasing side-chain length leads to a reduction in T_g. This is largely consistent with the findings of the current study, as the backbone chain of the investigated model system has a relatively higher stiffness compared to the branched side chains. Similar observations have also been reported in the recent CG-MD study of the star polymers by Fan *et al.*,[50] who showed that increasing the arm length leads to a reduction in T_g as the number of arms exceeding a critical value.

3.3.4. Chain Flexibility Modeling

To quantify the influence of side-chain length on the T_g of D-A CPs, it is vital to understand the interplay between the side-chain length and the polymer chain flexibility. Thus, an empirical mass-per-flexible bond model, first introduced by Di Marzio and Schnider for the prediction of polymer T_g based on the number of mass-per-flexible bonds in the repeating unit is employed here, as shown by the following equation:

$$T_g = A \left(\frac{M}{b} \right) + C \tag{21}$$

where M is the molecular weight of one repeat unit, b is the number of flexible bonds, A and C are the specific constants representing the steric hindrance and intermolecular interactions.[51–53] Here, the number of "flexible bond" b, ranging from 0 to 1 will be assigned to each covalent bond in the repeating unit, where 0 represents for an absolutely restricted bond without any rotational or conformational entropy, and 1 stands for a freely rotated bond.

We first apply the model to the polythiophene polymers with varied side-chain lengths, where the T_g value is obtained from previous literature.[54] Figure 3.3A demonstrates the assignment of b to different bonds of poly(3-butylthiophene-2,5-diyl) (P3BT). For simplicity, the thiophene ring is given a b value of 0.5 due to its limited rotational entropy, so does the single bond connected to the ring structure, while the non-restricted C-C bond on the side-chain has a b value of 1. Thus, by plotting T_g with $\frac{M}{b}$, the influence of chain flexibility on the chain relaxation behavior is obtained, where a linear correlation is shown for polythiophenes (Figure 3.3B). To correlate chain flexibility with side-chain length, Figure 3.3C plots T_g versus the weight percent of the side chain (wt %), where a two-stage reduction is shown as the side chain takes up more of the polymer mass and gets closer to unity: a quick T_g drop at a lower side-chain weight fraction followed by a plateau region. This observation is in agreement with the CG-MD simulations above. Using this model, the T_g of PDPPT-based polymers with different side-chain lengths are also plotted versus mass-per-flexible bond in Figure 3.3D and E, where a similar linear fit is obtained. In Figure 3.3D, the b value for each individual bond was marked for the backbone while a sum of b was marked for the side chain. Next, we aim to apply the model to T_g prediction for new PDPPT-based polymers. Two new polymers with a side-chain length of C2C6C10 (2-hexyl dodecyl) and C2C10C10 (2-decyl dodecyl) are separately synthesized and tested. As shown in Figure 3.3E, the T_g of both

polymers agree with the linear trend. Figure 3.3F shows a steep reduction of T_g with increasing side-chain fraction without obvious saturation, which may suggest that the T_g of PDPPT-based polymers can be further lowered through increasing side-chain length.
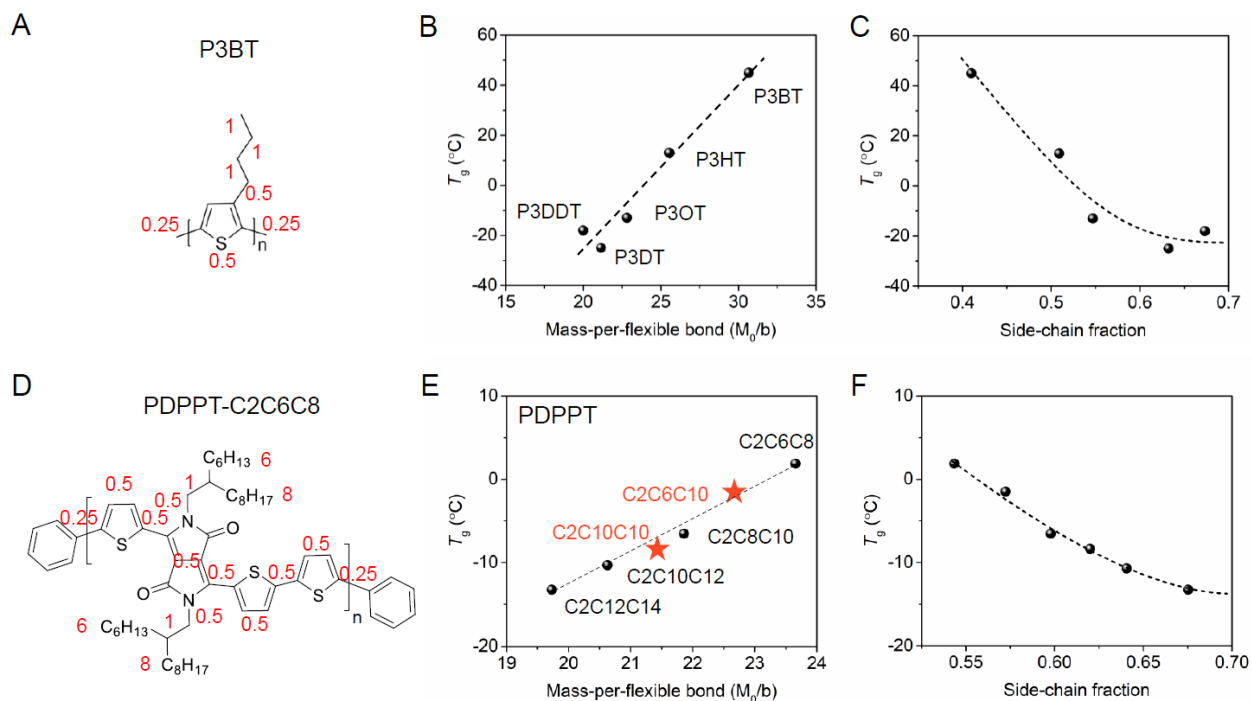
Figure 3.3. Applying mass-per-flexible bond model to conjugated polymers. (A-C) Polythiophenes. (D-F) PDPPT-based polymers. (A, D) Assignment of number of flexible bonds to polymers. (B, E) T_g over mass-per-flexible bond for polymers with different side-chain lengths. (C, F) T_g over side-chain weight fraction for polymers with different side-chain lengths.

3.3.5. Backbone Engineering

Besides side-chain engineering, the backbone of CPs is critical for controlling backbone dynamics. Upon introducing an additional high-T_g thiophene unit to the PDPPT backbone, PDPPT2 is purposely engineered for the validation of the proposed model; and to provide a designing method for high-T_g CPs. PDPPT2 with four different side-chain lengths are experimentally tested and computationally simulated using the same method mentioned above (Figure 3.4A). As shown in Figure 3.4C, the obtained T_g range expands broadly from 64.69 °C

(PDPPT2-C2C6C8) to 25.09 °C (PDPPT2-C2C8C10), 17.22 °C (PDPPT2-C2C10C12) and 1.38

°C (PDPPT2-C2C12C14). This trend closely follows the MD simulation result, where the T_g drops

with increasing M (Figure 3.4D). Importantly, the linear T_g-chain flexibility relationship is once

again captured by the mass-per-flexible bond model (Figure 3.4E). The capability of this model in

describing the structure-T_g relationship for different structures of CPs manifests its potential in T_g

prediction for other CPs. It is also noticeable that the slope in Figure 3.4E differs for PDPPT and

PDPPT2. Such a difference has been attributed to the intermolecular interactions and structural

steric hindrance.[53] However, due to the influence of side-chain length on both intermolecular

interactions (π-π stacking distance) and backbone T_g, these contributions are hard to deconvolute.
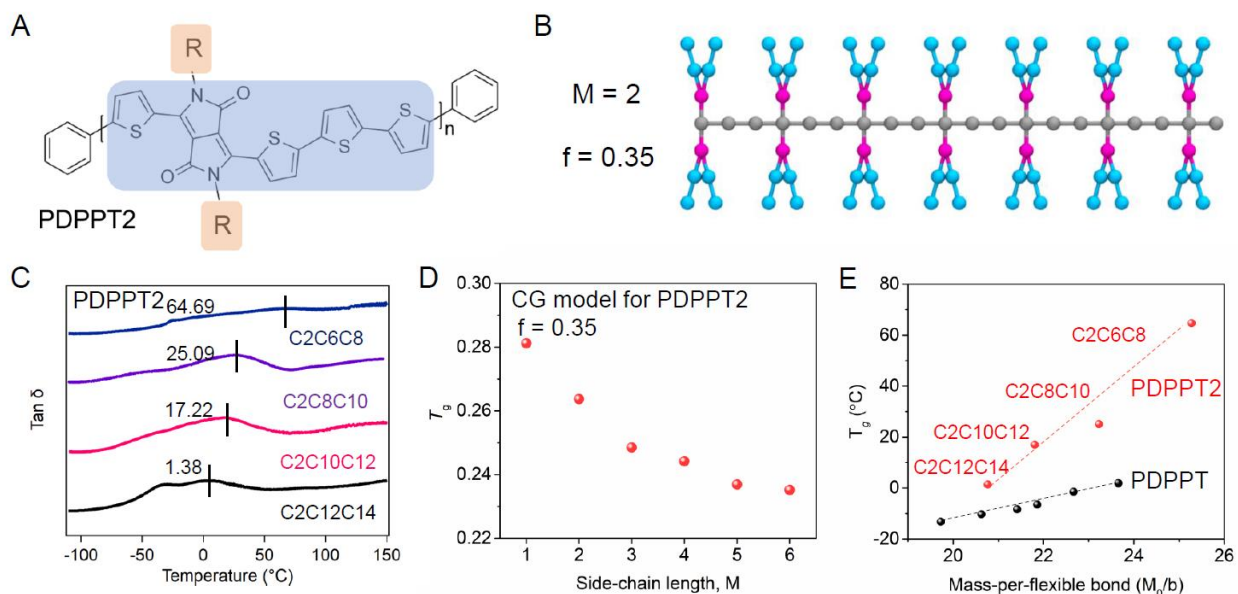
Figure 3.4. Experimental and simulation results of T_g for PDPP-T2 polymer with various side-chain lengths. (A) Chemical structure. (B) Geometrical configuration of simulated PDPPT2. (C) Tan δ versus temperature curves extracted from DMA. (D) Simulated T_g versus side-chain length M. (E) T_g over mass-per-flexible bond for polymers with different side-chain lengths.

To better understand glass transition, the effect of side-chain grafting density along the

polymer backbone is investigated through CG-MD simulations. Figure 3.5A shows the

representative topological configurations of simulated polymer models with varying grafting density f by adding more beads in between side-chain substituted backbone beads. Specifically, for $f = 0.2$ model, two potential geometries can be simulated, and only one is shown here due to their similar results. While the trend of T_g reduction with increasing side-chain length holds for all five models, the plateau region for $f = 0.15$ model appears at $M = 3$, but $f = 0.15$ model does not show a clear plateau up to $M = 6$ (Figure 3.5B). Similarly, the T_g drops at different rates with increasing grafting density for various side-chain lengths, where the low-M systems clearly show a steeper reduction but high-M systems are less affected. We attribute these observations to different "saturation limits" of side-chain length fractions for varied systems. In other words, polymer models with larger f (or M) tend to reach the plateaued T_g at smaller M (or f).
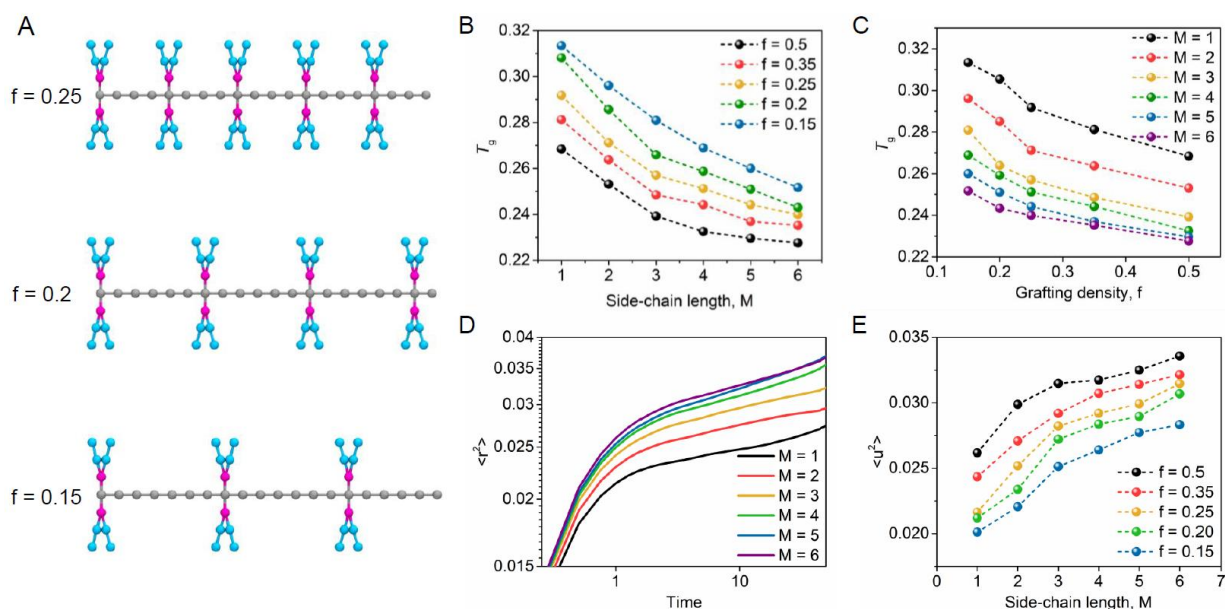
Figure 3.5. Simulation results of the grafting density effect on the T_g and dynamics of D-A CPs. (a) Topological configuration of simulated polymer chains with different grafting densities. (B) T_g versus side-chain length M for six polymers with different grafting densities f. (C) T_g versus grafting density f for polymers with different side-chain lengths M. (D) Segmental mean-squared displacement (MSD) of the polymer model with f of 0.35 grafting density for different side-chain lengths M. (E) Debye-Waller factor $\langle u^2 \rangle$ versus side-chain length M for polymers with different grafting densities f and side-chain lengths M.

To further explore the influence of the side-chain group on the glass transition nature of the current CG polymer model, we next calculate the Debye-Waller factor $\langle u^2 \rangle$, a fast-dynamic property that can be considered as a measure of the local free volume.[55,56] Experimentally, $\langle u^2 \rangle$ can be measured via X-ray and neutron scattering techniques.[57,58] Through MD simulations, $\langle u^2 \rangle$ could be obtained from calculations of mean-squared displacement (MSD) $\langle r^2(t) \rangle = \langle |r_i(t) - r_i(0)|^2 \rangle$ of the CG beads, where $r_i(t)$ is the position of the ith beads at time t and $\langle r^2(t) \rangle$ obtained from the average of all the CG beads. Here, $\langle u^2 \rangle$ is defined as the value of MSD at a caging time around 4 for the current model. Figure 3.5D shows the MSD as a function of time for the models with grafting f of 0.35 and different side-chain length at a temperature of 0.2. As it is expected, larger side-chain length M exhibits higher MSD values due to the enhanced mobility of chains. Furthermore, Figure 3.5E shows $\langle u^2 \rangle$ of the models with different grafting density and side-chain length. It is observed that as the fraction of side-chain beads in the bulk polymer model becomes larger, via increasing either M or f, $\langle u^2 \rangle$ tends to increase – a higher magnitude of $\langle u^2 \rangle$ indicates a greater local free volume associated with segmental mobility. This considerable influence of the grafting density and side-chain length on the T_g can thus be attributed to the enhanced local free volume created by the flexible side chains according to the well-known free volume argument of Fox and Loshaek.[59] However, this growth of the free volume with f and M can not be a universal trend for all glassy polymers. As evidenced previously,[45] the relative flexibility of the backbones and side-chain groups governs the side-chain length influence on the free volume and T_g. Current simulation results indicate that the structure of side-chain groups could be interpreted as an important parameter to control the T_g and mechanical properties of the D-A CPs, which inspires us to propose a physics-based empirical model to predict the T_g of CPs as described next.

Here, the quantitative mass-per-flexible bond model demonstrates a linear relationship between chain flexibility and polymer T_g. In the meantime, the CG-MD simulation study shows a two-stage T_g reduction with side-chain fraction until reaching a plateaued T_g. Moreover, as the side chain grafting density increases, the plateau T_g reduces without a crossing-over point. It should be noted that for a polymer with a sufficiently long side-chain length, the linear relationship built by the mass-per-flexible bond model may no longer be valid. This is because as the side chain length exceeds a threshold, the side chain becomes stiff enough that the number of flexible bonds per CH_2 moiety on the chain end slowly approaches 0. Similarly, we hypothesize that as the distance between the side-chain end and backbone reduces to a specific limit, the rigid backbone could restrict the side-chain flexibility and the backbone T_g will be less influenced by side-chain length. Thus it is tricky to attribute the number of the flexible bond to short-side chains.

While long and branched side chains are usually necessary for solubilization purposes, the proposed empirical model still provides theoretical limits and practical guidance to new polymer designs despite these limitations. For example, the T_g for PDPPT polymer has a lower limit of -37 °C and a high limit of 284 °C. Such understanding can help guide the selection of material applications from wearable electronics to thermal-stable OPVs. To build a new mass-per-flexible bond model for a different D-A CP system, it is required to experimentally measure the T_g of polymers with several side-chain structures. In the meantime, for backbone-engineered polymers with various soft or stiff moieties, the number of flexible bonds for the specific moiety can be tuned to fit the linear model. Similar studies along this line can refer to the effective atomic mobility theory recently proposed by Xie *et al*.[21] For the polymers reported here, although this theory captures the linear relationship between side-chain length and T_g, it does not provide a satisfactory prediction.

3.4. Conclusion

In summary, we develop a new model for predicting T_g of side-chain engineered D-A CPs. This model is tested and verified by using both P3ATs and PDPPT-based polymers, where the T_g of newly engineered PDPPT polymers can be predicted. CG-MD simulation further supports the experimental observations on the side-chain length dependence of polymer T_g, and provides insights into the influence of side-chain group and grafting density on chain mobility. Overall, this work presents multi-perspective T_g-controlling methods, and the polymers engineered here exhibit a wide T_g span over 80 °C. We expect these methods to guide the application-driven materials-by-design for D-A CP via molecular engineering, i.e., high T_g and stiff polymers, low T_g and soft polymers; as well as shed light on the future development of newly engineered D-A CPs with tailored thermal performance.

3.5. References

1. Zhang, S. *et al.* Toward the Prediction and Control of Glass Transition Temperature for Donor–Acceptor Polymers. *Adv. Funct. Mater.* **2002221**, 2002221 (2020).

2. Yamashita, Y. *et al.* Mobility Exceeding 10 cm2/(V·s) in Donor-Acceptor Polymer Transistors with Band-like Charge Transport. *Chem. Mater.* **28**, 420–424 (2016).

3. Kim, G. *et al.* A thienoisoindigo-naphthalene polymer with ultrahigh mobility of 14.4 cm 2 /V·s that substantially exceeds benchmark values for amorphous silicon semiconductors. *J. Am. Chem. Soc.* **136**, 9477–9483 (2014).

4. Luo, C. *et al.* General strategy for self-assembly of highly oriented nanocrystalline semiconducting polymers with high mobility. *Nano Lett.* **14**, 2764–2771 (2014).

5. Meng, L. *et al.* Organic and solution-processed tandem solar cells with 17.3% efficiency. *Science (80-.).* **361**, 1094–1098 (2018).

6. Mei, J., Diao, Y., Appleton, A. L., Fang, L. & Bao, Z. Integrated materials design of organic semiconductors for field-effect transistors. *J. Am. Chem. Soc.* **135**, 6724–6746 (2013).

7. Sirringhaus, H. 25th anniversary article: Organic field-effect transistors: The path beyond amorphous silicon. *Adv. Mater.* **26**, 1319–1335 (2014).

8. Xue, X. *et al.* Oriented Liquid Crystalline Polymer Semiconductor Films with Large Ordered Domains. *ACS Appl. Mater. Interfaces* **7**, 26726–26734 (2015).

9. Gu, X., Shaw, L., Gu, K., Toney, M. F. & Bao, Z. The meniscus-guided deposition of semiconducting polymers. *Nat. Commun.* **9**, 534 (2018).

10. Root, S. E., Savagatrup, S., Printz, A. D., Rodriquez, D. & Lipomi, D. J. Mechanical Properties of Organic Semiconductors for Stretchable, Highly Flexible, and Mechanically Robust Electronics. *Chem. Rev.* **117**, 6467–6499 (2017).

11. Someya, T., Bao, Z. & Malliaras, G. G. The rise of plastic bioelectronics. *Nature* **540**, 379–385 (2016).

12. Lipomi, D. J. & Bao, Z. Stretchable and ultraflexible organic electronics. *MRS Bull.* **42**, 93–97 (2017).

13. Bao, Z. & Chen, X. Flexible and Stretchable Devices. *Adv. Mater.* **28**, 4177–4179 (2016).

14. Oh, J. Y. & Bao, Z. Second Skin Enabled by Advanced Electronics. *Adv. Sci.* **6**, 1900186 (2019).

15. Lipomi, D. J., Tee, B. C. K., Vosgueritchian, M. & Bao, Z. Stretchable organic solar cells. *Adv. Mater.* **23**, 1771–1775 (2011).

16. Chortos, A., Liu, J. & Bao, Z. Pursuing prosthetic electronic skin. *Nat. Mater.* **15**, 937–950 (2016).

17. Gumyusenge, A. *et al.* Semiconducting polymer blends that exhibit stable charge transport at high temperatures. *Science (80-.).* **362**, 1131–1134 (2018).

18. Tran, D. T. *et al.* Effects of Side Chain on High Temperature Operation Stability of Conjugated Polymers. *ACS Appl. Polym. Mater.* acsapm.9b00999 (2019). doi:10.1021/acsapm.9b00999

19. Zhang, S. *et al.* Probing the Viscoelastic Property of Pseudo Free-Standing Conjugated Polymeric Thin Films. *Macromol. Rapid Commun.* **39**, (2018).

20. Xu, J. *et al.* Highly stretchable polymer semiconductor films through the nanoconfinement effect. *Science (80-.).* **355**, 59–64 (2017).

21. Xie, R. *et al.* Glass transition temperature from the chemical structure of conjugated polymers. *Nat. Commun.* **11**, 4–11 (2020).

22.   Sharma, A., Pan, X., Campbell, J. A., Andersson, M. R. & Lewis, D. A. Unravelling the Thermomechanical Properties of Bulk Heterojunction Blends in Polymer Solar Cells. *Macromolecules* **50**, 3347–3354 (2017).

23.   Balar, N. *et al.* The Importance of Entanglements in Optimizing the Mechanical and Electrical Performance of All-Polymer Solar Cells. *Chem. Mater.* **31**, 5124–5132 (2019).

24.   Qian, Z. *et al.* Glass Transition Phenomenon for Conjugated Polymers. *Macromol. Chem. Phys.* **220**, 1900062 (2019).

25.   Savagatrup, S. *et al.* Viability of stretchable poly(3-heptylthiophene) (P3HpT) for organic solar cells and field-effect transistors. *Synth. Met.* **203**, 208–214 (2015).

26.   Yang, S.-F. *et al.* Diketopyrrolopyrrole-Based Conjugated Polymer Entailing Triethylene Glycols as Side Chains with High Thin-Film Charge Mobility without Post-Treatments. *Adv. Sci.* **4**, 1700048 (2017).

27.   Martín, J., Stingelin, N. & Cangialosi, D. Direct Calorimetric Observation of the Rigid Amorphous Fraction in a Semiconducting Polymer. *J. Phys. Chem. Lett.* **9**, 990–995 (2018).

28.   Zhang, S. *et al.* The Critical Role of Electron-Donating Thiophene Groups on the Mechanical and Thermal Properties of Donor–Acceptor Semiconducting Polymers. *Adv. Electron. Mater.* **5**, 1–11 (2019).

29.   Chiang, Y. C. *et al.* Tailoring Carbosilane Side Chains toward Intrinsically Stretchable Semiconducting Polymers. *Macromolecules* **52**, 4393–4404 (2019).

30.   Savagatrup, S., Printz, A. D., Rodriquez, D. & Lipomi, D. J. Best of both worlds: Conjugated polymers exhibiting good photovoltaic behavior and high tensile elasticity. *Macromolecules* **47**, 1981–1992 (2014).

31.   Root, S. E., Savagatrup, S., Pais, C. J., Arya, G. & Lipomi, D. J. Predicting the Mechanical Properties of Organic Semiconductors Using Coarse-Grained Molecular Dynamics Simulations. *Macromolecules* **49**, 2886–2894 (2016).

32.   Chen, H. *et al.* Highly π-Extended Copolymers with Diketopyrrolopyrrole Moieties for High-Performance Field-Effect Transistors. *Adv. Mater.* **24**, 4618–4622 (2012).

33.   Potestio, R., Peter, C. & Kremer, K. Computer simulations of soft matter: Linking the scales. *Entropy* **16**, 4199–4245 (2014).

34.   Noid, W. G. Perspective: Coarse-grained models for biomolecular systems. *J. Chem. Phys.* **139**, 09B201_1 (2013).

35.   Xia, W. *et al.* Energy renormalization for coarse-graining polymers having different segmental structures. *Sci. Adv.* **5**, eaav4683 (2019).

36.   Plimpton, S. Fast parallel algorithms for short-range molecular dynamics. *J. Comput. Phys.* **117**, 1–19 (1995).

37.   Ilavsky, J. Nika: Software for two-dimensional data reduction. *J. Appl. Crystallogr.* **45**, 324–328 (2012).

38.   Oosterhout, S. D. *et al.* Mixing Behavior in Small Molecule:Fullerene Organic Photovoltaics. *Chem. Mater.* **29**, 3062–3069 (2017).

39.   Sharma, A. *et al.* Probing the Relationship between Molecular Structures, Thermal Transitions, and Morphology in Polymer Semiconductors Using a Woven Glass-Mesh-Based DMTA Technique. *Chem. Mater.* **31**, 6740–6749 (2019).

40.   Zhou, D., Huth, H., Gao, Y., Xue, G. & Schick, C. Calorimetric glass transition of poly(2,6-dimethyl-1,5-phenylene oxide) thin films. *Macromolecules* **41**, 7662–7666 (2008).

41. Xie, S.-J., Qian, H.-J. & Lu, Z.-Y. The glass transition of polymers with different side-chain stiffness confined in free-standing thin films. *J. Chem. Phys.* **142**, 74902 (2015).

42. Dudowicz, J., Freed, K. F. & Douglas, J. F. Direct computation of characteristic temperatures and relaxation times for glass-forming polymer liquids. *J. Chem. Phys.* **123**, 111102 (2005).

43. Dudowicz, J., Freed, K. F. & Douglas, J. F. The glass transition temperature of polymer melts. *J. Phys. Chem. B* **109**, 21285–21292 (2005).

44. Dudowicz, J., Freed, K. F. & Douglas, J. F. Fragility of glass-forming polymer liquids. *J. Phys. Chem. B* **109**, 21350–21356 (2005).

45. Dudowicz, J., Freed, K. F. & Douglas, J. F. Generalized entropy theory of polymer glass formation. *Adv. Chem. Phys.* **137**, 125 (2008).

46. Xia, W., Song, J., Hsu, D. D. & Keten, S. Side-group size effects on interfaces and glass formation in supported polymer thin films. *J. Chem. Phys.* **146**, 203311 (2017).

47. Hsu, D. D., Xia, W., Song, J. & Keten, S. Glass-transition and side-chain dynamics in thin films: explaining dissimilar free surface effects for polystyrene vs poly (methyl methacrylate). *ACS Macro Lett.* **5**, 481–486 (2016).

48. Xia, W. & Lan, T. Interfacial Dynamics Governs the Mechanical Properties of Glassy Polymer Thin Films. *Macromolecules* **52**, 6547–6554 (2019).

49. Xia, W., Song, J., Hsu, D. D. & Keten, S. Understanding the interfacial mechanical response of nanoscale polymer thin films via nanoindentation. *Macromolecules* **49**, 3810–3817 (2016).

50. Fan, J., Emamy, H., Chremos, A., Douglas, J. F. & Starr, F. W. Dynamic heterogeneity and collective motion in star polymer melts. *J. Chem. Phys.* **152**, 54904 (2020).

51. Schneider, H. A. & Di Marzio, E. A. The glass temperature of polymer blends: comparison of both the free volume and the entropy predictions with data. *Polymer.* **33**, 3453–3461 (1992).

52. Schneider, H. A. Polymer class specificity of the glass temperature. *Polymer.* **46**, 2230–2237 (2005).

53. Schut, J. *et al.* Glass transition temperature prediction of polymers through the mass-per-flexible-bond principle. *Polymer.* **48**, 6115–6124 (2007).

54. Chen, S. A. & Ni, J. M. Structure/properties of conjugated conductive polymers. 1. Neutral poly(3-alkythiophene)s. *Macromolecules* **25**, 6081–6089 (1992).

55. Starr, F. W., Sastry, S., Douglas, J. F. & Glotzer, S. C. What do we learn from the local geometry of glass-forming liquids? *Phys. Rev. Lett.* **89**, 125501 (2002).

56. Betancourt, B. A. P., Hanakata, P. Z., Starr, F. W. & Douglas, J. F. Quantitative relations between cooperative motion, emergent elasticity, and free volume in model glass-forming polymer materials. *Proc. Natl. Acad. Sci.* **112**, 2966–2971 (2015).

57. Bellissent-Funel, M. C., Filabozzi, A. & Chen, S. H. Measurement of coherent Debye-Waller factor in in vivo deuterated C-phycocyanin by inelastic neutron scattering. *Biophys. J.* **72**, 1792–1799 (1997).

58. Harada, J., Suzuki, H. & Hoshino, S. Neutron Scattering Study of Lattice Dynamics in CuBr. II. Anharmonic Effect on Debye-Waller Factor. *J. Phys. Soc. Japan* **41**, 1707–1715 (1976).

59. Fox, T. G. & Loshaek, S. Influence of molecular weight and degree of crosslinking on the specific volume and glass temperature of polymers. *J. Polym. Sci.* **15**, 371–390 (1955).

4. AN INTEGRATED STUDY TO PREDICT GLASS TRANSITION TEMPERATURE OF CONJUGATED POLYMERS

Glass transition temperature (T_g) is a fundamental property that governs the chain dynamics and thermomechanical properties of the conjugated polymers (CPs). Despite its vital role in the applicability of the CPs, it remains notably challenging to predict T_g of CPs due to the heterogeneous chain architectures and diverse chemical building blocks. Driven by this need, the chapter aims to present a predictive modeling framework to predict T_g for a wide range of CPs through the integration of machine learning (ML), molecular dynamics simulations, and experiments.[1]

4.1. Introduction

Semiconducting CPs are attractive organic electronic materials for various applications due to their unique properties such as easy processability,[2] tunable electrical performance, and mechanical flexibility with diverse chemistry.[3–10] Through the engineering of molecular structure and chain architecture, these organic semiconductors have shown great promise in advanced stretchable/flexible electronic devices and wearable electronics.[11–15] In particular, the mechanical behaviors of CPs are directly related to glass-transition temperature (T_g) that governs the dynamics and thermal performance of polymer chains. Despite tremendous efforts, design and prediction of T_g remain notably challenging for CPs due to their complex chain architecture associated with diverse "donor-acceptor" (D-A) chemical building blocks. The highly rigid backbone and semi-crystalline nature of CPs complicate tracking the heat flow and accurate assessment of glass transition.[16] More importantly, due to the endless possibilities of CPs' building blocks, experimental measurement of T_g for new designs of CPs can be time-consuming if not impossible. So far, only a limited number of CPs have been tested and reported for their T_g's through

experiments.[17] Hence, a computational predictive framework to predict T_g directly from the geometry of chemical building block, before any synthesis process, is profoundly advantageous for CPs in applications of the next-generation electronic devices.

Many physical parameters are found to play a vital role in influencing T_g of polymers, such as chain rigidity, intermolecular interactions, segmental structure, and chain topology.[17–24] Generally, T_g would raise by increasing the chain stiffness of polymer backbone due to the higher hindrance for translational and rotational motion;[18,25–27] consistently, for different CPs, T_g is found to be correlated to persistence length and rotational volume.[23,28,29] Alkyl side groups largely influence the chain mobility where increasing side-chain length causes T_g to drop and is expected to occupy a larger volume fraction among the polymer backbones. This increase in the free volume could be quantified in terms of the Debye-Waller factor at a picosecond time scale.[30] Our previous study has shown that an increase of the alkyl side-chain length of CPs leads to a higher Debye-Waller factor and mobility compared to the backbone, unraveling the origin of their decreasing influence on the T_g.[31] In addition, modifications in the topology of the polymer chain, e.g., changing the grafting density, have been found to considerably affect the T_g.[17,18,31] The coupled influence of these many structural/physical features provokes the idea to quantify T_g directly from the chemical building block and fingerprints by delineating the underlying "structure-property" relationship.

To address this issue, the cheminformatics-based Quantitative Structure-Property Relationship (QSPR) modeling approach has been utilized as a predictive computational framework that links the physicochemical properties of compounds to their chemical structure.[32] The QSPR aims to find a mathematical relationship between the target variable and molecular descriptors extracted from the molecules' chemical structure. QSPR methods have been

successfully employed to predict T_g of non-conjugated polymers with an appropriate level of confidence. Katritzky and coworkers[33] developed a four-parameter QSPR model with a R^2 of 0.928 for prediction the T_g values of 22 different linear-chain homopolymers and copolymers. On a larger dataset,[34] they developed a five-descriptor QSPR model where the predictive model showed an a R^2 of 0.946. However, despite the considerable performance of QSPR methodology, interpreting and quantifying a large number (i.e., over a few thousand) of molecular descriptors, e.g., molar refractivity, dipole moment, polarizability, and constitutional descriptors could be very challenging, limiting its practical usage for the community.

In recent years, machine learning (ML) algorithms have been increasingly employed to develop simplified surrogate models with excellent predictive capability.[35–37] By extracting molecular features directly from the geometry of the monomer, ML-based surrogate modeling could be advantageous over QSPR modeling by avoiding the aforementioned complexities of feature descriptors. If successful, such simplified models are much more desired for the experimental community to predict T_g for newly designed CPs before any synthesis process. More recently, Xie and coworkers[38] proposed a single-parameter-empirical model to predict T_g based on the mobility parameter of different functional groups of the repeat unit. Their model showed an excellent T_g prediction for 32 experimentally tested semi-flexible (mostly conjugated) polymers with alkyl side chains, where a root-mean-square error (*RMSE*) of 13 °C was observed. However, without any out-of-sample testing for validation, it is still questionable that such a simplified model is capable of T_g prediction over diverse CPs with a much-enlarged dataset.

Built upon recent efforts, in this study, we employ an integrated experimental-computational approach to predict T_g for a diverse set of over 94 polymers (mostly CPs) with a drastic differences in their chemical structures (i.e., backbones and side chains). As illustrated in

Figure 4.1, built upon the backward elimination technique and regression analysis, a surrogate ML model is proposed that takes the geometry of the chemical building blocks within a repeat unit as simplified molecular features to make the T_g prediction. In addition to the existing T_g data collected from the literature,[17] we perform dynamic mechanical analysis (DMA), differential scanning calorimetry (DSC) experiments, as well as molecular dynamics simulations (MD) to improve the diversity of the dataset, which is further used to train the predictive model and perform external validation. The simplified ML results reveal that T_g is strongly governed by the chemical structure of the key building block of the CPs. Furthermore, MD simulations allow us to gain valuable insights into the dynamic heterogeneity and chain dynamics at a fundamental molecular level, which is experimentally tested by performing quasielastic neutron scattering on CPs. Our study establishes an integrated predictive framework for T_g's of diverse CPs, paving the way for materials-by-design for high-performance CPs and relevant materials via molecular engineering.
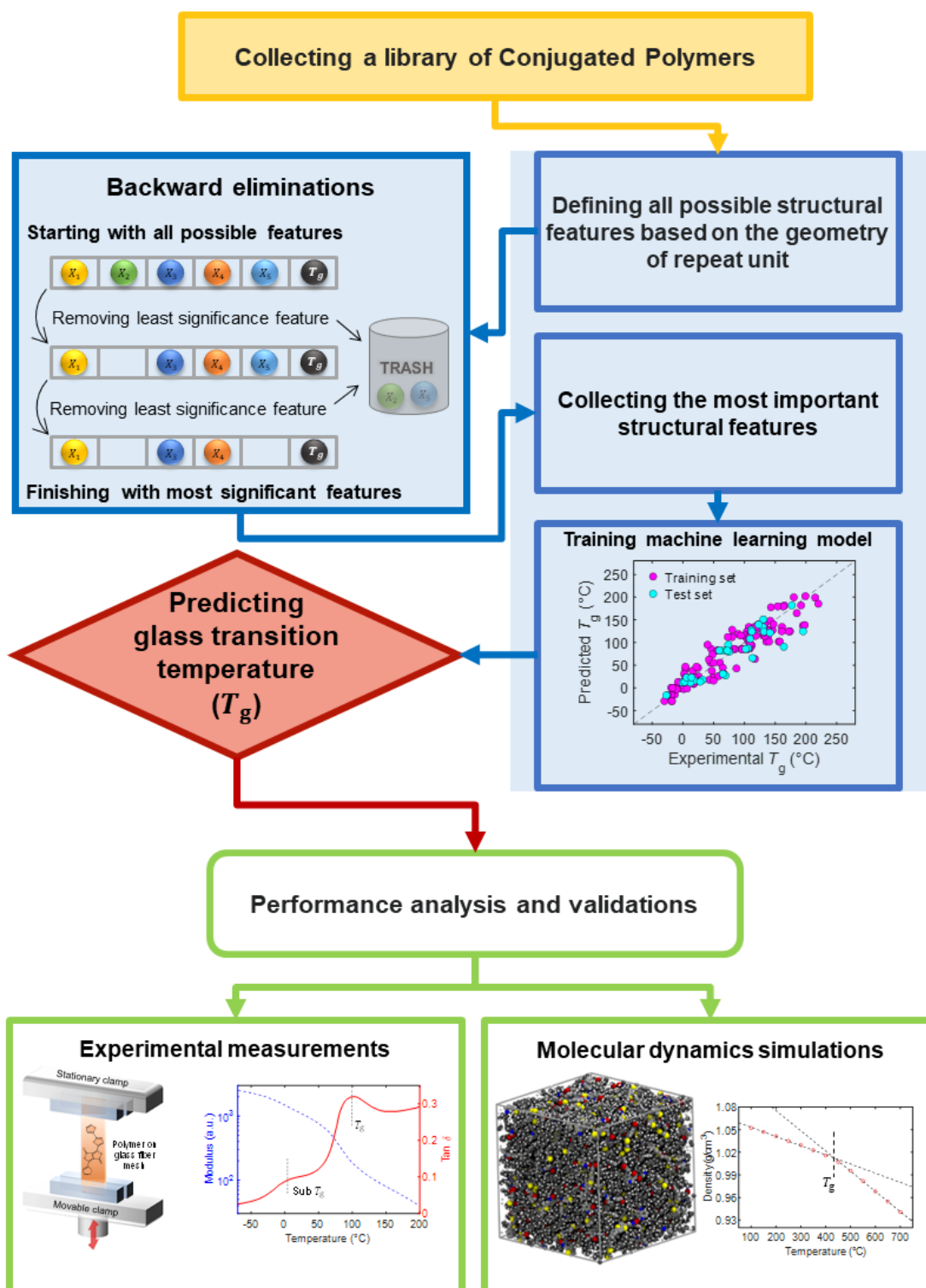
Figure 4.1. Flow chart of the current integrated machine learning framework, molecular dynamics simulations, and experimental techniques to predict glass transition temperature of conjugated polymers.

4.2. Results and Discussion

4.2.1. Predicting T_g From the Chemical Building Blocks

This section will introduce an ML-based surrogate model by employing the ordinary least squares (OLS) multiple linear regression algorithm. Among 154 collected T_g data points, 119 values are from previously published literature,[17,31,38] 17 from our experimental measurements (i.e., DMA and DSC), and 18 are carried out via MD simulations. It should be noted that for some CPs, multiple T_g values are reported from different groups and we consider all those data points in our ML model. Overall, we collect T_g data points of over 94 diverse polymers and acceptor units. Then, we define around 30 structural/molecular features directly from the geometry of the chemical building blocks within a repeat unit. Informed by the QSPR modeling,[18] these structural features can be categorized into four major groups, namely the side-chains, aromatic rings, different kinds of atoms, and double/triple bonds that are not part of aromatic rings. In particular, the aromatic rings features based on their chemical environment include isolated, fused, and bridged rings. After defining all features, a backward elimination[39] technique is utilized to perform the significance level test (i.e., significance is used to determine whether the relationship between features and T_g exists or not) and find the most important structural features that are closely correlated to T_g. In the end, six structural features are identified to develop the ML model for the prediction of T_g of diverse CPs. Accordingly, T_g is found primarily influenced by the side-chain fraction, number of isolated, fused, and bridged aromatic rings, number of halogenated atoms, such as "Fluorine" or "Chlorine", and number of double/triple bonds which are not part of aromatic rings. It should be noted that all aforementioned features are normalized by the total number of heavy atoms in the repeat unit (i.e., excluding hydrogens). The multiple linear regression model based on structural features can be expressed as follows:

$$T_g = \beta_0 + \sum \beta_i X_i, \qquad X_i = [NSC, NFCL, NDTB, NIR, NFR, NBR]/N \qquad (22)$$

where β_0 is a constant value, and β_i are contribution coefficients of each feature in the regression model. *N* is the total number of atoms in the repeat unit (excluding hydrogens). *NSC* stands for the number of Carbon atoms in the alkyl side chains; *NFCL* is the total number of "Fluorine" and "Chlorine" atoms in the monomer; *NDTB* is the number of double/triple bonds which are not part of aromatic rings; *NIR* is the number of free/isolated rings either in the backbone or side groups; *NFR* stands for the number of fused rings in which adjacent carbon atoms are shared; *NBR* is the number of bridged rings where adjacent rings are bridged via valence bonds. A list of these selected structural features, their descriptions, and example of relevant moieties is presented in Table 4.1.

Table 4.1. A list of selected structural features and their descriptions utilized in the machine learning model to predict the glass transition temperature of the conjugated polymer.
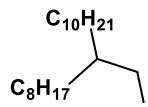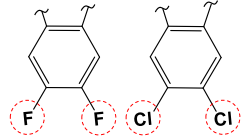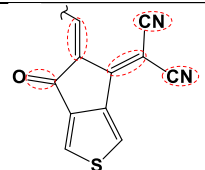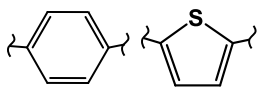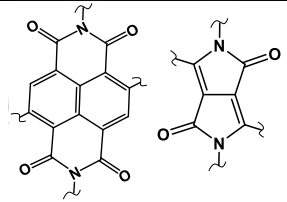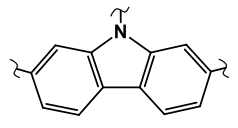
Feature names	Description	Example of chemical structure
NSC	Number of Carbon atoms in the alkyl side chains	
NFCL	Total number of "Fluorine" and "Chlorine" atoms in the repeat unit	
NDTB	Number of double/triple bonds which are not part of aromatic rings	
NIR	Number of isolated rings either in the backbone or side groups	
NFR	Number of fused rings in which adjacent carbon atoms are shared	
NBR	Number of bridged rings where adjacent rings are bridged via valence bonds	

Figure 4.2 shows a graphical illustration of different kinds of aromatic rings in representative CPs. To simplify the feature calculations consistently, four assumptions (or rules) have been made to count the number of aromatic rings, before training the ML model:

- There is no difference between different kinds of rings, for example, thiophene, phenyl, and pyrrole compounds are treated in the same way.

55

- If a ring is fused on one side and bridged on the other side, that compound would be counted twice, one for fused rings (*NFR*) and one for bridged rings (*NBR*) since those kinds of hindrances significantly increase the chain stiffness and subsequently T_g (see Y2 acceptor unit in Figure 4.2).

- The pentagonal rings with grafted side chains on the tip which bridges two adjacent compounds at both sides are not counted as any features, such as fused nor bridged. The examples of these rings excluded from the features are highlighted with a purple "X" label in Figure 4.2.

- The number of successive fused rings compounds is weighted differently before counting the overall *NFR* for each repeat unit. According to our collected data, when more than two rings are fused, T_g of CPs exhibits an excessive tendency to increase. To address this phenomenon, the weighted number of successive fused rings is calculated as $2 + w_a(n - 2)$ where n is the number of successive fused rings and w_a is a weighting factor, which needs to be determined. For example, for the PTB7-Th polymer in Figure 4.2, there are two fused rings groups: for those two fused thiophenes, the weighted number would be $2 + w_a(2 - 2) = 2$, implying that no weighting is needed when just two rings are fused; however, that phenyl ring fused to two thiophenes at both sides forms three successive fused rings which need to be weighted as $2 + w_a(3 - 2) = 2 + w_a$. Then, the weighted values of all fused groups will be summed to determine the value of *NFR* of that polymer. As another example for naphthalenediimide-based (NDI) polymers, four successive fused rings need to be weighted as $2 + w_a(4 - 2) = 2 + 2w_a$. Then, the optimum value of w_a is determined by evaluating the coefficient of determination (R^2) and root-mean-square error (*RMSE*)

of the ML models as a function of w_a, where the highest R^2 or lowest *RMSE* values

lead to $w_a = 3.5$ that will be used for training the ML model.
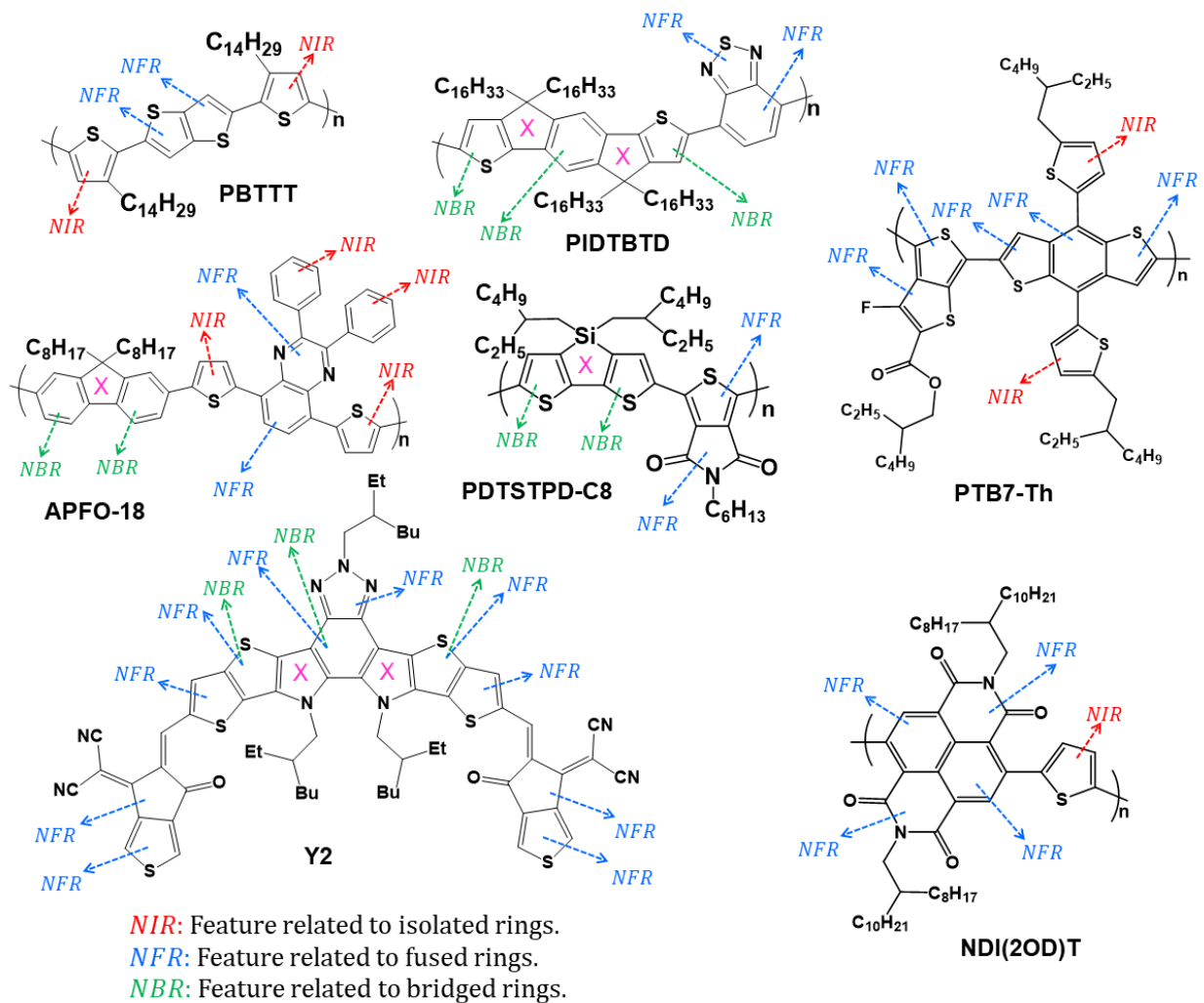
Figure 4.2. Graphical illustration of defining features related to the aromatic rings in the repeat unit of conjugated polymers. Features related to isolated rings (NIR), fused rings (NFR), and bridged rings (NBR) are shown in red, blue, and green fonts, respectively. Those rings with a purple "X" label are not counted as any features, such as fused nor bridged rings.

Then, the contribution of each feature (β_i) is determined by fitting the regression model to

the training set, and the ML model for T_g prediction can be described as follows:

$$T_g(\text{℃}) = 115.3 + \frac{-239.8\,NSC - 598.3\,NFCL + 170\,NDTB + 456.6\,NIR + 666.5\,NFR + 1323.9\,NBR}{N} \qquad (23)$$

A comparison between predicted T_g and experimental/computational values is presented in Figure 4.3A for both training and test sets. Despite having a very diverse library of CPs and acceptor units with different chemical structures, assessment of the model shows excellent predictive performance as measured by R^2 of 0.86 and *RMSE* of 22.4 °C for the training set. Furthermore, ML model prediction for the external validation of the test set yields R^2 of 0.83 and *RMSE* of 27.8 °C, showing a satisfactory performance based on an out-of-sample dataset. The evaluation of the results demonstrates that the trained ML model is capable of predicting T_g from the "simplified" features based on the geometry of a few chemical building blocks. In particular, for those high-T_g CPs with complex D-A units, such as NDI-based polymers, poly[(2,6-(4,8-bis(5-(2-ethylhexyl-3-fluoro)thiophen-2-yl)-benzo[1,2-b:4,5-b′]dithiophene))-alt-(5,5-(1′,3′-di-2-thienyl-5′,7′-bis(2ethylhexyl)benzo[1′,2′-c:4′,5′-c′]dithiophene-4,8-dione)] (PM6), poly[(2,6-(4,8-bis(5-(2-ethylhexyl-3-chlore)thiophen-2-yl)-benzo[1,2-b:4,5-b′]dithiophene))-alt-(5,5-(1′,3′-di-2-thienyl-5′,7′-bis(2ethylhexyl)benzo[1′,2′-c:4′,5′-c′]dithiophene-4,8-dione)] (PM7), as well as several other polymers and acceptor units with aromatic rings, our ML model shows an excellent agreement between predicted and measured T_g.
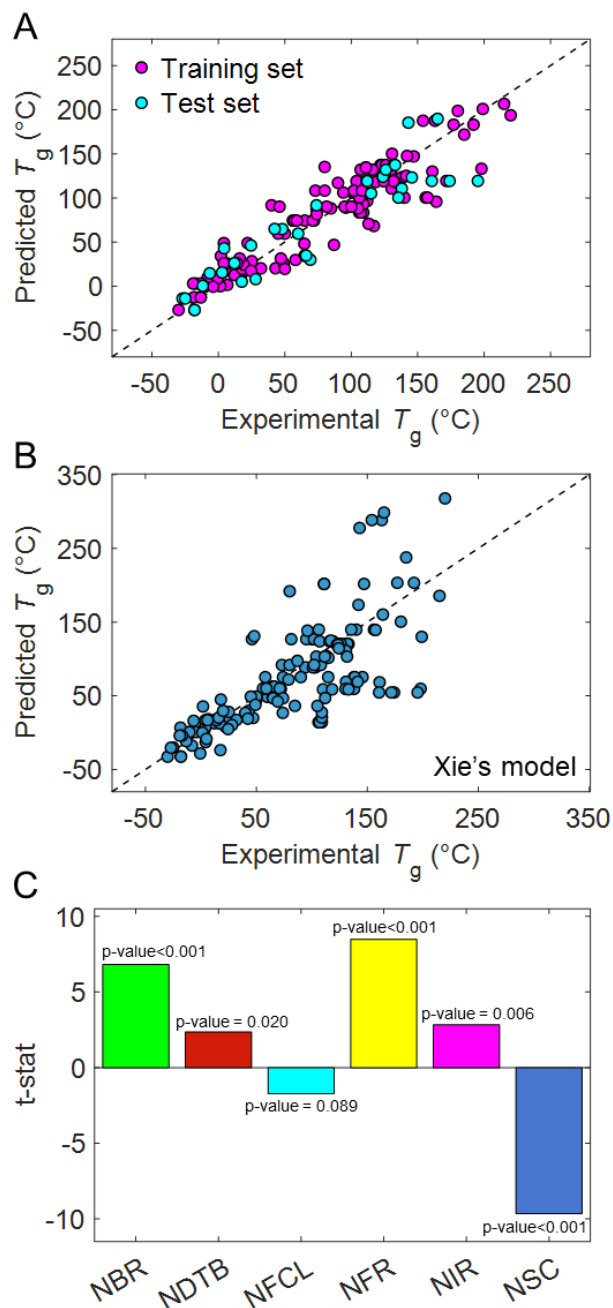
Figure 4.3. (A) Comparison between glass transition temperature (T_g) predicted by multiple regression model versus experimental and simulation values. 80% of the dataset is divided into the training set and 20% is preserved unknown from the model for out-of-sample testing. (B) Comparison between the T_g predicted by Xie's model versus experimental and simulation values of the whole dataset of conjugated polymers employed in this study. (C) The contribution of features in the regression model assessed by the value of the t-statistic. Large absolute values of t-statistic mean more noticeable contribution. Side chains and aromatic rings are found to have the dominant role to determine T_g. The p-value of each feature is reported inside the figure.

59

We next compare our model with a semi-empirical model recently developed Colby and Gomez group (i.e., we call it "Xie's model" here)[38] for the T_g predictions from the chemical structure. In Xie's model, they proposed a single adjustable mobility parameter ξ, defined as summation of assigned atomic mobility to each functional group in the repeat unit, to establish a quantitative relationship between T_g and chemical structures of about 30 CPs. To have a better comparison between these two models, we calculate Xie's mobility parameter ξ for the whole dataset utilized in this study and predicted T_g values are reported in Figure 4.3B. As it is indicated, despite an acceptable performance of Xie's model especially for lower T_g CPs, such as thiophene- and polydiketopyrrolopyrrole (PDPP)-based systems, it doesn't yield reliable prediction for the aforementioned high-T_g CPs as measured by a relatively low R^2 of 0.57 and large *RMSE* of 46.6 °C. There are three main differences between Xie's model and our ML approach: first, Xie and coworkers did not consider the influence of successive fused rings when more than two rings are fused, resulting in an underestimated prediction of T_g for CPs with a larger number of fused rings, such as NDI-based polymers; second, their model does demonstrate the reducing influence of halogen atoms on T_g of CPs; third, Xie's model is tested for a limited set of 32 semi-flexible polymers and mobility value ξ does not generalize to our diverse dataset, and as they discussed, modifications of ξ values for specific chemical structures may be needed to improve the predictive performance.

4.2.2. Relative Importance of Essential Structural Features

Based on the current developed ML model, we next discuss the relative importance and contribution of each structural feature to T_g prediction of diverse CPs and other complex polymers to better understand the physical roles of different chemical building blocks. For this purpose, the t-statistic parameter, defined as feature coefficient (β_i) normalized by its standard error, is

calculated as a measurement of the feature contribution. A larger t-statistic parameter implies the statistically significant contribution of that feature in which positive and negative sign of t-statistic is related to enhancing and reducing influence on T_g, respectively.

Side chains. As indicated in Figure 4.3C, the coefficient related to the side-chain fraction (*NSC*) shows the largest t-statistic that indicates its significant contribution where the negative value implies the reducing influence on T_g. To determine whether the current trend that we observe in our samples remains valid on the larger population, the p-value of each feature is calculated. The p-value assesses the null hypothesis if the feature does not correlate with the target variable (T_g) in which a p-values less than the significance level (i.e., 0.05) provide enough evidence to reject the null hypothesis over the entire population. For the side-chain fraction (*NSC*), a p-value less than 0.001 is calculated much below the significance level proofing this feature is statistically considerable. Previous efforts have shown that increasing the side-chain length decrease the T_g due to an increase in free volume associated with higher segmental mobility and governs localized relaxations (γ).[31,40,41] For instance, experimental results showed a reduction in the T_g and elastic modulus of DPP-based polymer with increasing the length of alkyl side-chains.[30] Consistent with experimental observations, this reducing influence of the alkyl side chains on T_g is captured well by our ML model.

Halogen atoms. Next feature that lowers T_g is the number of Fluorine and Chlorine atoms (*NFCL*) in the repeat unit. These halogen atoms are highly electronegative, being widely utilized recently to control the energy bandgap, and improve the power conversion efficiency of organic solar cells.[42] However, their influence on T_g is still remains ambiguous. It has been shown that the C-F bond can form intermolecular interaction with other atoms (e.g., phenyl-erfluorophenyl, C…H, F…F, and C–F…π_F),[43,44] which inherently can influence the thermomechanical properties

of the polymer.[21] Kroon and coworkers[45] showed that incorporation of two Fluorine atoms on the acceptor in poly[6,7-difluoro-2,3-bis(3-(octyloxy)phenyl)qui-noxaline-alt-thiophene] (TQ-F) drops T_g from 100 °C to 48 °C. For TQ-F, the incorporation of Fluorine atoms was found to slightly increase the torsion angle, which increases chain flexibility accompanied by backbone irregularity and thereby lowers T_g. Our MD simulations, also show a similar reducing trend of T_g for Y5 acceptor unit and its fluorinated and chlorinated versions (i.e., Y6 and Y7 units, respectively), where both Y6 and Y7 yield lower T_g values comparing to Y5. However, T_g of chlorinated version, Y7, is slightly larger than fluorinated Y6 unit. Similar trend for fluorinated PM6 and its chlorinated version (PM7) is also observed in our MD simulations – PM7 shows higher T_g value compared with PM6. This could be because of higher steric hindrance of Chlorine atoms relative to Fluorine as it was experimentally reported for a series of halogenated CPs.[42]

The current ML model is trained by the aforementioned available CPs data which include halogen atoms, and Figure 4.3C shows that their decreasing influence on T_g is predicted. However, due to limited data points, this feature slightly falls beyond the significance level test with a p-value of 0.089 larger than the threshold value. We decide to keep the current feature in the predictive model since it captures the T_g trend for halogenated organic semiconducting materials. With the development of new CPs with halogen atoms, the model can be further improved by having more experimental data in the future to train our model.

Double/triple bonds. The other feature that is found to noticeably contribute to the determination of T_g is the number of double/triple bonds (*NDTB*) in the repeat unit, which considers the influence of weakly mobile atoms. Vinylene, carbonyl, and nitrile groups are counted as *NDTB* in our ML model (see Y2 units in Figure 4.2 as an example). As the t-statistic parameter

shows in Figure 4.3C, the *NDTB* feature has a noticeably enhancing influence on T_g, where a small p-value of 0.028 indicates this feature passes the significance level test.

Aromatic rings. The structural features of aromatic rings (i.e., *NIR*, *NFR*, and *NBR*) in our predictive model are found to have a significant enhancing influence on T_g as they govern conformational rigidity of the CPs' backbone. As shown in Figure 4.3C, the *NIR* feature for the isolated rings exhibits a considerable contribution in the model prediction and successfully passes the significance level test where a small p-value of 0.006 is calculated. Hence, incorporating any isolated aromatic rings into the polymer backbone is expected to increase T_g. This is consistent with experimental studies, where the addition of the thiophene rings to the DPP-based CPs ended in an increased T_g.[31,46] The fused and bridged rings as labeled by *NFR* and *NBR* features, respectively, have the most significant positive contributions to T_g, where *NFR* feature yields a slightly larger contribution parameter (t-statistic). Both features have a very small p-value (less than 0.001), indicating a passed significance level test. Previous experimental studies also confirm this finding that presence of fused and bridged rings in the backbone largely correlates to stiffer CPs with larger T_g and modulus.[46–49]

4.2.3. Dynamical Heterogeneity of Diverse Chemical Structures

As the glass transition is primarily governed by the segmental relaxation dynamics and chain mobility, we next perform MD simulations, in conjunction with experiments, to better understand the fundamental roles of diverse chemical building blocks in the dynamics of CPs. Informed from the ML modeling and feature analyses, we focus on segmental dynamics of aromatic rings with different chemical configurations and side chains (i.e., the most influential structural features) of four representative CPs, (i.e., DPPT, poly[N-9′-heptadecanyl-2,7-carbazole-alt-5,5-(4′,7′-di-2-thienyl-2′,1′,3′-benzothiadiazole)] (PCDTBT), isoindigo (IID-2T), NDI-T)

(see Figure 4.4). Specifically, we evaluate the local Debye-Waller Factor $\langle u^2 \rangle$, a fast-dynamic physical property at a picosecond timescale,[50] by calculating mean-squared displacement (MSD) of the center of mass of each chemical group in MD simulations. In particular, $\langle u^2 \rangle$ can be experimentally measured via the quasi-elastic neutron scattering (QENS) technique, which is found to be closely related to the local free volume and mobility and be inversely related to the local molecular stiffness $(1/\langle u^2 \rangle)$,[30] we call it inversed local mobility here. Previously, QENS was broadly employed to study the dynamics of polycarbonate (PC) films,[51] non-conjugated polymers with alkyl side chains in bulk samples,[52,53] and polyalkylthiophenes CPs.[54–57]
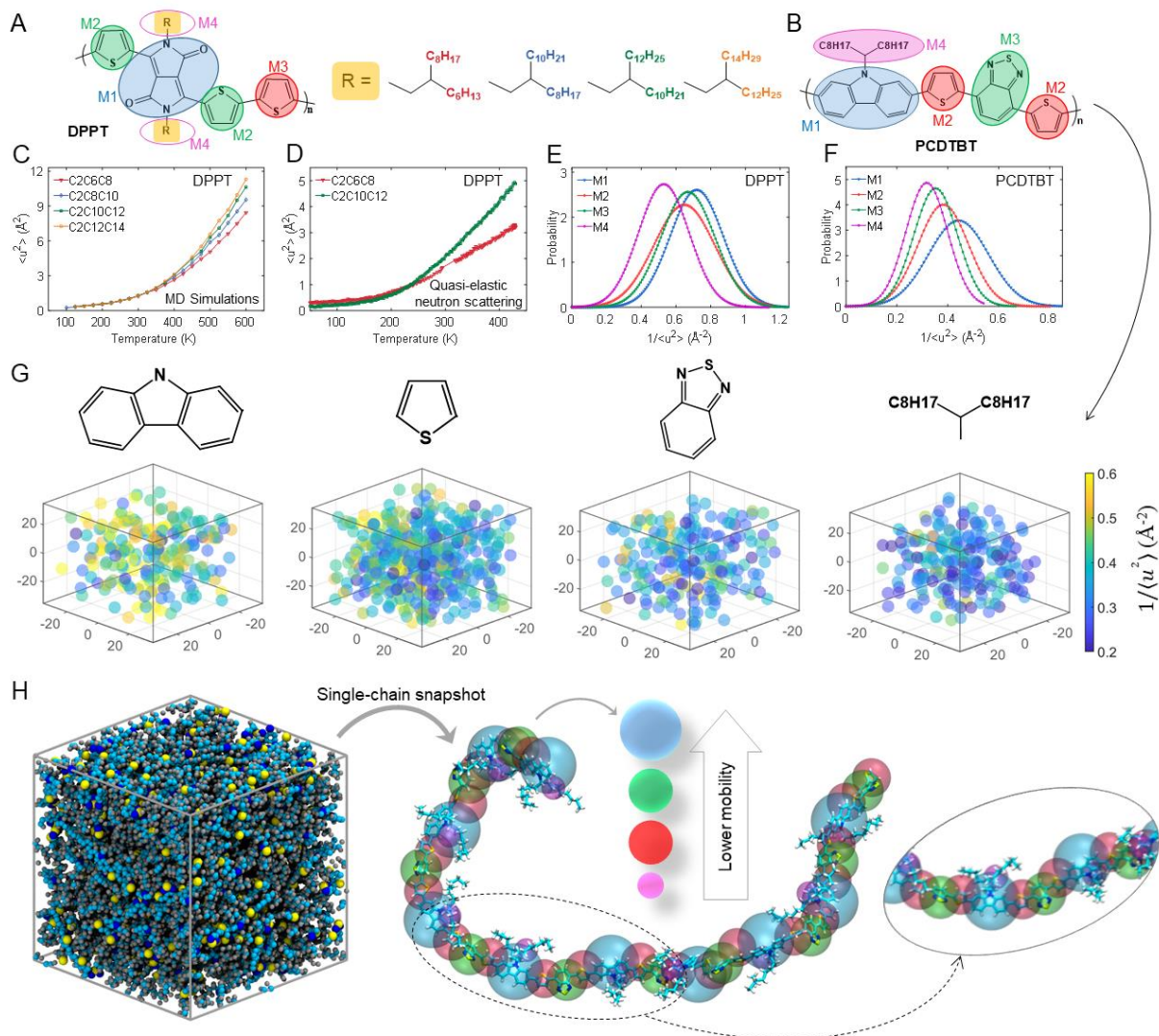
Figure 4.4. (A) Chemical structure of DPP-based polymer with four different side-chain lengths. (B) Chemical structure of PCDTBT polymer. (C) Mean-squared displacement (MSD) of the DPP-based polymers with varied alkyl side chains obtained by molecular dynamics (MD) simulations and (D) Quasielastic neutron scattering. (E) Normal distribution of inversed local mobility ($1/\langle u^2 \rangle$) of different functional groups of DPP-based polymers (C2C8C10) and (F) PCDTBT obtained by MD simulations. (G) Spatial distribution of $1/\langle u^2 \rangle$ of different functional groups of PCDTBT polymer. Each point represents the center of mass of the relevant functional group in the bulk system. Yellowish color means higher $1/\langle u^2 \rangle$ corresponding to lower mobility. The blueish color represents lower $1/\langle u^2 \rangle$ related to higher mobility. (H) A representative snapshot bulk simulation box and single-chain snapshot of PCDTBT polymer obtained by MD simulations. A larger transparent sphere illustrates higher $1/\langle u^2 \rangle$. To have more clear illustration, one repeat unit of the polymer chain is magnified.

Figure 4.4C shows the $\langle u^2 \rangle$ (i.e., local mobility) results for DPPT with different side-chain lengths from both MD simulations and the QENS measurement (by directly probing the dynamics of the hydrogen atoms due to its large incoherent scattering section). Both simulation and experimental results show that $\langle u^2 \rangle$ increases with temperature due to the enhanced segmental mobility upon heating; at a higher temperature above T_g (around 300 K), $\langle u^2 \rangle$ starts to deviate from a near-linear trend at a lower temperature. Another observation is that at a lower T, there is no significant difference of $\langle u^2 \rangle$ values for different alkyl side-chain lengths; however, above 350 K, the increase in side-chain length is found to increase $\langle u^2 \rangle$ and thus the chain mobility. This is consistent with our QENS measurement (Figure 4.4D), demonstrating that our MD simulations can capture segmental dynamics of CPs to a good approximation. Knowing the applicability of our MD calculations, below we focus on the local dynamics of each functional group at an elevated $T \approx 1.5\ T_g$ for different CPs.

Figure 4.4E shows the probability distribution of $1/\langle u^2 \rangle$, a measure of inversed local mobility, for four different building blocks of the DPPT polymers with C2C8C10 side chains, i.e., DPP core (labeled as M1 in blue), thiophene rings tied to DPP core (group M2 marked in green), isolated thiophene moiety that is not tied to DPP core (group M3 marked in red), and alkyl side chains (labeled as M4 in purple). Apparent Gaussian distribution of $1/\langle u^2 \rangle$ is observed for all four functional groups. The fused DPP unit (M1) shows a larger mean of $1/\langle u^2 \rangle$, implying that this compound indicates relatively lowest mobility among all functional groups in this polymer. In contrast, side chains (M4) exhibit the lowest mean of $1/\langle u^2 \rangle$ with a smaller standard deviation due to higher mobility of side chains. The thiophene rings in the DPPT monomer exhibit different inversed local mobility based on their chemical environment - thiophenes directly tied to the DPP core (M2) show a slightly higher mean in the distribution compared to M3 thiophenes. The MD

simulation results of segmental dynamics of the DPPT are largely consistent with our feature analyses in the ML model, where the fused rings yield a steeper increase in the T_g compared to the isolated rings. The observed lower inversed local mobility of the side chains is also in line with the negative contribution coefficient of the *NSC* feature in the ML model.

Figure 4.4F shows the distribution of $1/\langle u^2 \rangle$ of different chemical building blocks of PCDTBT having three different groups of aromatic rings. Similar to DPPT, it can be observed that CDT bridged unit (M1) show the highest mean value of $1/\langle u^2 \rangle$ with a larger mean of the distribution, while the side chains (M4) show the lowest value. Furthermore, fused BT (Benzothiadiazole) unit (M3) exhibits a higher mean of $1/\langle u^2 \rangle$ distribution compared with thiophene rings (M2), implying that M3 fused moiety has lower mobility than isolated rings (M2). This could be attributed to the fact that only the phenyl ring of the BT unit is tied to the backbone, and its current vertical orientation makes it easier for out-of-plane rotation, resulting in relatively higher mobility than isolated rings (M2). Our result again suggests that the local dynamics of the functional groups are largely dependent on the chemical environment.

Figure 4.4G shows the spatial distributions of $1/\langle u^2 \rangle$ of different functional groups of PCDTBT, confirms again that CDT bridged unit and side chains have the highest and lowest magnitude of inversed local mobility. Each point illustrates the center of mass of the relevant functional group in the bulk system with the color showing the magnitude of inversed local mobility $1/\langle u^2 \rangle$. Interestingly, the spatial distribution of $1/\langle u^2 \rangle$ reveals a reduced level of dynamical heterogeneity is clearly observed from M1 to M4 as their mobility increases, which reflects their packing efficiency at a molecular level, i.e., a higher level dynamical heterogeneity corresponds to a more frustrated molecular packing. Such dynamical heterogeneity associated with different chemical groups of PCDTBT is further illustrated in Figure 4.4H, where larger

transparent spheres illustrate higher local $1/\langle u^2 \rangle$. Similar dynamics behaviors are also observed for IID and NDI-based donor-acceptor CPs, where the fused rings (i.e., IID and NDI core) and side chains exhibit the highest and lowest magnitude of inversed local mobility, respectively. The MD simulation results of local dynamics corroborate findings of ML modeling that aromatic rings (i.e., *NIR*, *NFR,* and *NBR* features) and side chains (*NSC*) governs T_g prediction of CPs.

4.2.4. Application of ML Model for Predicting T_g of Conjugated Polymers

In this section, we test the ML model by applying it to predicting T_g's of representative CPs particularly related to organic solar cell applications. Device stability is a challenge that severely limits organic solar cells from being widely adopted to replace silicon ones and their inorganic counterparts. Through decades of optimizing the optoelectronic properties of narrow bandgap CPs together with non-fullerene acceptors (NFAs), remarkable progress has been made in organic photovoltaics (OPV) technology with the power conversion efficiency (PCE) reaching over 18%.[58–60] However, the long-term stability of OPV devices is one of the major hurdles that prevents this technology from being widely implemented, along with the lack of scalable manufacturing techniques to obtain ideal bulk heterojunction (BHJ) morphology. We expect our ML model developed here to potentially rationalize the stability issue and guide the development of the new CP materials.

We apply the model to the leading optoelectronic polymers and non-fullerene acceptors (See Figure 4.5 for their chemical structure) that were recently reported in high-performance solar cells. For the PM6, PM7, and PTB7 polymers, T_g value of 123.2 °C, 123.2 °C, and 91.7 °C are predicted by the ML model, respectively. By the help of our experimental collaborators (Gu group at the university of southern Mississippi), we further experimentally measure T_g for PM6 and PTB7 polymers and the results are shown in Figure 4.5 in which DMA and DSC techniques

indicate a T_g of 138.6 °C and 114.7 °C, respectively, for PM6 and a T_g of 73.8 °C for PTB7 (obtained by DMA). Both conventional and fast scanning calorimeter were employed to detect T_g for PM6, where the T_g values were consistent for both methods regarding the difference in cooling rates. In addition, MD simulations predict T_g value of 145.6 °C for the PM7 polymer close enough to T_g of 123.2 °C predicted by our ML framework. For the Y-Family NFAs, as indicated in Figure 4.5, T_g values predicted by ML model are found in a good agreement with those calculated by MD simulations. In addition, for other experimentally measured as well as simulated T_g results for different CPs employed in this study, listed in Figure 4.5, a good agreement is observed with ML prediction, implying the reliability of our predictive framework.
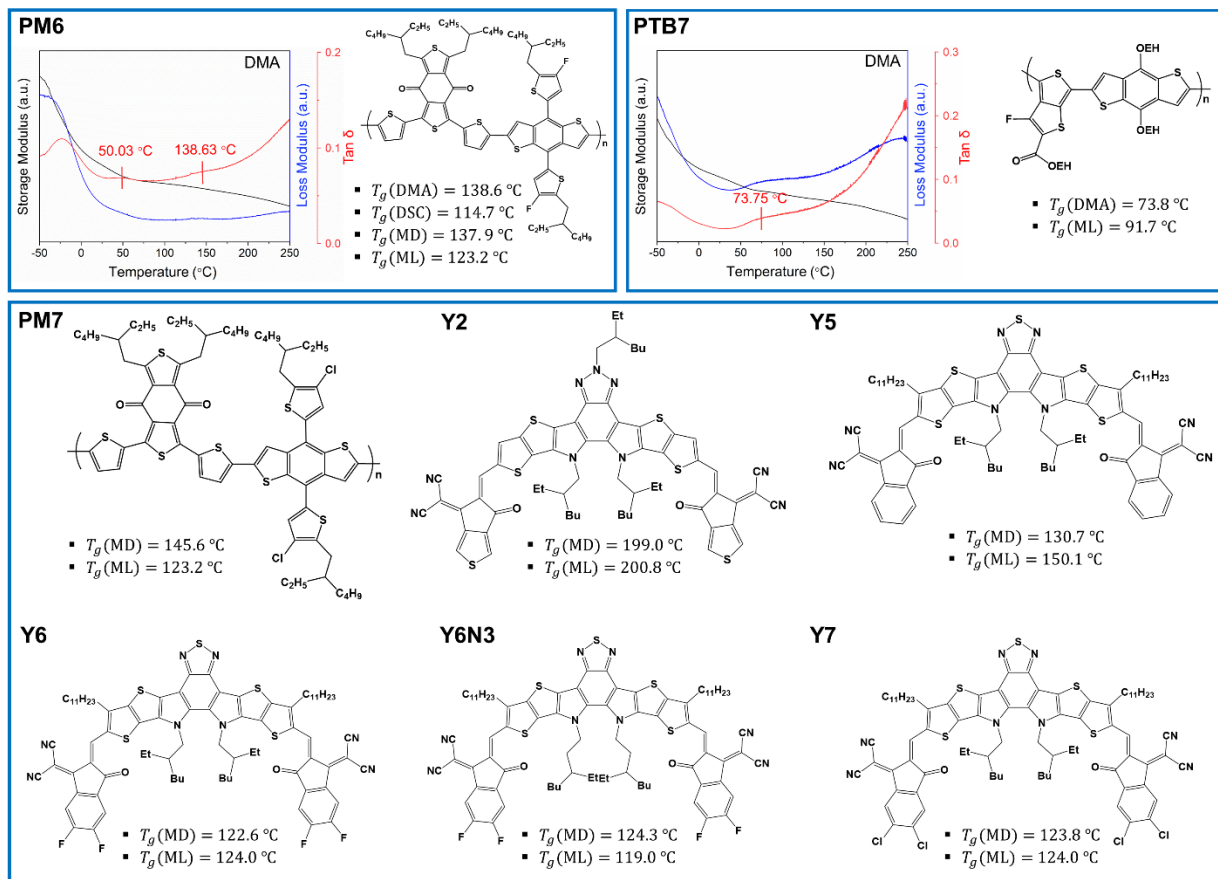
Figure 4.5. Chemical structures and glass transition temperature (T_g) of selected conjugated polymers and acceptor units with aromatic backbones and alkyl side chains. Results of T_g are obtained from molecular dynamics (MD) simulations, machine learning (ML) prediction, and available experimental techniques (DMA and DSC).

Based on our discovery here, all PM6, PM7, PTB7, and Y-family NFAs possess a relatively high T_g, as compared to other CPs with the operating temperature of the device at room temperature or up to 80 °C for most upper limit in inorganic cells. Although the T_g values for measured components are slightly higher than the operation temperature, thus CPs are limited in chain dynamics within the experimental time scale for device degradation. The observed PCE drop over time below T_g thus is highly likely due to changes in the interface property between the BHJ layer with electrodes, or due to the diffusion-limited cold-crystallization in either donor or acceptors. For the small molecules in Y-family NFAs, other researchers suggested this is possible.

70

In the case of tuning T_g, for example for the PM6, T_g could be improved by lowering the side chain length from 2-ethylhexyl to 2-ethylbutyl in order to raise T_g above 150 °C. Additional attention should also be paid to the role of cold crystallization with respect to T_g of both donors and acceptors, which have been discussed in previous studies.[61–64] In general, the practical usage of our ML model is to quantitatively estimate the unknown T_g for advanced D-A CP polymers used in organic solar cell field since T_g determines the dynamics of the possible cold crystallization occurred under operational conditions. Cold crystallization can form different polymorphs depending on the isothermal annealing temperature higher or lower than nominal T_g.[64] The polymorph formed at higher temperature normally impairs the performance, whereas the polymorph formed at lower temperature could improve performance presumably due to the stronger light absorption from the continuous aromatic structures.[63] However, the size of crystallite also influences the performance of organic solar cells that large size of crystallites tends to detrimental the performance and stability.[62] Therefore, the observed PCE drop over time below T_g thus is highly likely due to changes in the interface property between the BHJ layer with electrodes, or due to the large size of crystallites formed via diffusion limited cold-crystallization in either donor or acceptors.

4.3. Experimental and Computational Procedures

Materials. The materials for T_g measurements were purchased from Ossila Company, including F8BT, PTB7, PTB70Th, PM6, PCPDTBT, TFB, TQ1, NDI(2HD)T, NDI(2HD)2T, NDI(2OD)T, and NDI(2OD)2T.

Quasi-elastic Neutron Scattering. QENS measurements were performed using the Backscattering Spectrometer (BASIS)[65] at the Spallation Neutron Source (SNS) at Oak Ridge National Laboratory (ORNL). Time scales for BASIS range from 10 to1000 ps.[57] Elastic scan

measurements were carried out under vacuum to protect the material from degradation at high temperatures between 50 K and 450 K. Scattering data were reduced utilizing the DAVE software[66] to measure MSD.

Dynamic Mechanical Analysis. DMA measurements were carried out with a TA Q800 DMA by a modified DMA method.[31,67] For sample preparation, polymer solutions (5~10 mg/ml) were drop-casted on top of a glass fiber mesh. At a fixed frequency of 1 Hz, temperature ramp experiments with a heating rate of 3 °C min^{-1} were measured between −50 and 250 °C to measure the T_g of the materials.

Differential Scanning Calorimetry. DSC measurements were performed using both Mettler-Toledo fast scanning calorimeter (Flash DSC 2+) and conventional DSC (DSC 3+). The flash DSC was equipped with an ultra-fast standard chip with heating/cooling rates up to 4000 K/s, where the indium standard was used to calibrate the heat flow and temperatures at 10 K/min heating rate for conventional DSC. All measurements were done under nitrogen gas.

Dataset. The experimental values of T_g are collected from the previously published literature, including 119 data points.[17,31,38] To improve the diversity of the dataset, we further experimentally measured an additional 17 T_g data points of different CPs from either DMA and DSC measurements as well as 18 T_g obtained by MD simulations. These additional data cover newly designed high-performance CPs, allowing for the external validation and improvement of the model prediction. Overall, the dataset is composed of 154 data points of 94 polymers covering thiophene-, fluorene-, DDP-, bridged-, and fused-based CPs, newly designed non-fluorine acceptor units, and some non-conjugated polymers with aromatic rings in their backbone. The dataset is provided in the supporting information of our paper,[1] see Table S1 and Table S2.

ML-based surrogate model. Informed from the QSPR modeling and feature analyses, we use the aforementioned dataset of CPs to define the structural features based on the geometry (i.e., chemical building block) of the repeat unit. We first define all possible structural features, including the number of different atoms in the repeat units, bridged units, fused rings, free isolated rings, stiff bonds, heavy atoms, side-chain fraction, etc. Then, backward elimination,[39] a feature selection technique, is utilized to screen those structural features while building the regression models. To perform backward elimination, we introduce a significance level of 5% to test the null hypothesis for each feature based on the p-value.[68] The regression model is then fitted to the data set and the p-value of each feature is calculated, which determines whether the feature will generalize any population out of the current sample. Next, the feature with the highest p-value is removed from the predictive model, and the process iterates for the remaining features. This mechanism continues until all p-values of all remaining features in the dataset are less than the significance level. Then a regression model is trained to the selected feature to make a T_g prediction.

MD simulations. All-atomistic MD simulations of the 18 bulk CPs and acceptor units are carried out using the LAMMPS software package.[69] The interactions of the MD models are defined via the General Amber Force Field (GAFF), which was originally developed for organic molecules.[70] The CP models are initially generated using Materials Studio software, followed by geometry optimization. Then, the antechamber module of the AmberTools20 package[70] is utilized for atom typing and calculating atomic charges. The details of AA-MD simulations are reported in Chapter 2. To determine T_g of bulk CP, the simulation is run further under NPT ensemble to collect the density over a wide range of the temperature from 100 K to 800 K. The obtained density as a function of temperature can be fitted with linear lines at low temperature glassy and high

temperature melt regimes, where the intersection of fitted lines marks T_g. To measure the local mobility of moieties, MSD (i.e., a measurement of the deviation of position of atoms from the reference position over time) $\langle r^2(t) \rangle$ values are obtained for the center of mass functional groups of the repeat unit, $\langle r^2(t) \rangle = \langle |r_i(t) - r_i(0)|^2 \rangle$, where $r_i(t)$ is the position of the ith atoms at time t and $\langle r^2(t) \rangle$ is obtained from the average of all related functional groups. Then, Debye-Waller factor $\langle u^2 \rangle$, a fast-dynamic property at a picosecond time scale,[50] is defined at $t = 4$ ps for all models to quantify local mobility.

4.4. Conclusion

In this study, we establish a machine learning (ML) model to predict glass transition temperature (T_g) of conjugated polymers (CPs) from the chemical structure of the repeat unit. With 154 T_g values collected from diverse resources, a predictive model is developed where six functional groups in the repeat unit (i.e., side-chain fraction, isolated rings, fused rings, bridged rings, double/triple bonds, and halogen atoms) are identified as essential structural features. Among the selected feature, side chains and halogen atoms show a decreasing influence on T_g. The t-statistic parameter is employed to quantify the contribution of each structural feature in the prediction of T_g, where aromatic rings and side chains are found to have the most significant influence. In addition, our molecular dynamics (MD) simulations reveal that aromatic rings and side chains have the highest and lowest local mobility, respectively, unraveling their dominant role in the ML model. Our experimental measurements of T_g as well as those calculated by MD simulations confirm the noticeably accurate predictivity performance of our ML model for high-performance solar cell materials. We believe that the current ML framework provides an effective strategy to design the next generation of organic electronics with tailored chain dynamics.

4.5. References

1. Alesadi, A. *et al.* Machine learning prediction of glass transition temperature of conjugated polymers from chemical structure. *Cell Reports Phys. Sci.* 100911 (2022).

2. Gu, X., Shaw, L., Gu, K., Toney, M. F. & Bao, Z. The meniscus-guided deposition of semiconducting polymers. *Nat. Commun.* **9**, 534 (2018).

3. Root, S. E., Savagatrup, S., Printz, A. D., Rodriquez, D. & Lipomi, D. J. Mechanical Properties of Organic Semiconductors for Stretchable, Highly Flexible, and Mechanically Robust Electronics. *Chem. Rev.* **117**, 6467–6499 (2017).

4. Someya, T., Bao, Z. & Malliaras, G. G. The rise of plastic bioelectronics. *Nature* **540**, 379–385 (2016).

5. Lipomi, D. J. & Bao, Z. Stretchable and ultraflexible organic electronics. *MRS Bull.* **42**, 93–97 (2017).

6. Bao, Z. & Chen, X. Flexible and Stretchable Devices. *Adv. Mater.* **28**, 4177–4179 (2016).

7. Oh, J. Y. & Bao, Z. Second Skin Enabled by Advanced Electronics. *Adv. Sci.* **6**, 1900186 (2019).

8. Lipomi, D. J., Tee, B. C. K., Vosgueritchian, M. & Bao, Z. Stretchable organic solar cells. *Adv. Mater.* **23**, 1771–1775 (2011).

9. Chortos, A., Liu, J. & Bao, Z. Pursuing prosthetic electronic skin. *Nat. Mater.* **15**, 937–950 (2016).

10. Zhang, S. *et al.* Molecular Origin of Strain-Induced Chain Alignment in PDPP-Based Semiconducting Polymeric Thin Films. *Adv. Funct. Mater.* **31**, 2100161 (2021).

11. Oh, J. Y. *et al.* Intrinsically stretchable and healable semiconducting polymer for organic transistors. *Nature* **539**, 411–415 (2016).

12.   Wang, S. *et al.* Skin electronics from scalable fabrication of an intrinsically stretchable transistor array. *Nature* **555**, 83–88 (2018).

13.   Xu, J. *et al.* Highly stretchable polymer semiconductor films through the nanoconfinement effect. *Science (80-.).* **355**, 59–64 (2017).

14.   Xu, J. *et al.* Tuning Conjugated Polymer Chain Packing for Stretchable Semiconductors. *Adv. Mater.* 2104747 (2021). doi:10.1002/adma.202104747

15.   Maller, O. *et al.* Tumour-associated macrophages drive stromal cell-dependent collagen crosslinking and stiffening to promote breast cancer aggression. *Nat. Mater.* **20**, 548–559 (2021).

16.   Qian, Z. *et al.* Challenge and solution of characterizing glass transition temperature for conjugated polymers by differential scanning calorimetry. *J. Polym. Sci. Part B Polym. Phys.* **57**, 1635–1644 (2019).

17.   Qian, Z. *et al.* Glass Transition Phenomenon for Conjugated Polymers. *Macromol. Chem. Phys.* **220**, 1900062 (2019).

18.   Karuth, A., Alesadi, A., Xia, W. & Rasulev, B. Predicting glass transition of amorphous polymers by application of cheminformatics and molecular dynamics simulations. *Polymer.* **218**, 123495 (2021).

19.   Xie, S. J., Qian, H. J. & Lu, Z. Y. The glass transition of polymers with different side-chain stiffness confined in free-standing thin films. *J. Chem. Phys.* **142**, (2015).

20.   Xu, W.-S. & Freed, K. F. Influence of cohesive energy and chain stiffness on polymer glass formation. *Macromolecules* **47**, 6990–6997 (2014).

21.   Alesadi, A. & Xia, W. Understanding the Role of Cohesive Interaction in Mechanical Behavior of a Glassy Polymer. *Macromolecules* **53**, 2754–2763 (2020).

22. Xu, W.-S., Douglas, J. F. & Freed, K. F. Influence of cohesive energy on the thermodynamic properties of a model glass-forming polymer melt. *Macromolecules* **49**, 8341–8354 (2016).

23. Xiao, M. *et al.* Linking Glass-Transition Behavior to Photophysical and Charge Transport Properties of High-Mobility Conjugated Polymers. *Adv. Funct. Mater.* **31**, 1–11 (2021).

24. Zhao, H. *et al.* Manipulating Conjugated Polymer Backbone Dynamics through Controlled Thermal Cleavage of Alkyl Side Chains. *Macromol. Rapid Commun.* 2200533 (2022).

25. Xu, W.-S., Douglas, J. F. & Xu, X. Molecular Dynamics Study of Glass Formation in Polymer Melts with Varying Chain Stiffness. *Macromolecules* **53**, 4796–4809 (2020).

26. Cao, Z., Leng, M., Cao, Y., Gu, X. & Fang, L. How rigid are conjugated non-ladder and ladder polymers? *J. Polym. Sci.* **60**, 298–310 (2021).

27. Zhang, W., Gomez, E. D. & Milner, S. T. Predicting chain dimensions of semiflexible polymers from dihedral potentials. *Macromolecules* **47**, 6453–6461 (2014).

28. McCulloch, B. *et al.* Polymer chain shape of poly(3-alkylthiophenes) in solution using small-angle neutron scattering. *Macromolecules* **46**, 1899–1907 (2013).

29. Müller, C., Esmaeili, M., Riekel, C., Breiby, D. W. & Inganäs, O. Micro X-ray diffraction mapping of a fluorene copolymer fibre. *Polymer.* **54**, 805–811 (2013).

30. Pazmiño Betancourt, B. A., Hanakata, P. Z., Starr, F. W. & Douglas, J. F. Quantitative relations between cooperative motion, emergent elasticity, and free volume in model glass-forming polymer materials. *Proc. Natl. Acad. Sci. U. S. A.* **112**, 2966–2971 (2015).

31. Zhang, S. *et al.* Toward the Prediction and Control of Glass Transition Temperature for Donor–Acceptor Polymers. *Adv. Funct. Mater.* **2002221**, 2002221 (2020).

32. Katritzky, A. R. *et al.* Quantitative correlation of physical and chemical properties with chemical structure: Utility for prediction. *Chem. Rev.* **110**, 5714–5789 (2010).

33. Katritzky, A. R., Rachwal, P., Law, K. W., Karelson, M. & Lobanov, V. S. Prediction of polymer glass transition temperatures using a general quantitative structure-property relationship treatment. *J. Chem. Inf. Comput. Sci.* **36**, 879–884 (1996).

34. Katritzky, A. R., Sild, S., Lobanov, V. & Karelson, M. Quantitative Structure - Property Relationship (QSPR) correlation of glass transition temperatures of high molecular weight polymers. *J. Chem. Inf. Comput. Sci.* **38**, 300–304 (1998).

35. Doan Tran, H. *et al.* Machine-learning predictions of polymer properties with Polymer Genome. *J. Appl. Phys.* **128**, (2020).

36. Jackson, N. E., Webb, M. A. & de Pablo, J. J. Recent advances in machine learning towards multiscale soft materials design. *Curr. Opin. Chem. Eng.* **23**, 106–114 (2019).

37. Sivaraman, G. *et al.* A machine learning workflow for molecular analysis: application to melting points. *Mach. Learn. Sci. Technol.* **1**, 25015 (2020).

38. Xie, R. *et al.* Glass transition temperature from the chemical structure of conjugated polymers. *Nat. Commun.* **11**, 4–11 (2020).

39. Hocking, R. R. A Biometrics invited paper. The analysis and selection of variables in linear regression. *Biometrics* **32**, 1–49 (1976).

40. Chiang, Y. C. *et al.* Tailoring Carbosilane Side Chains toward Intrinsically Stretchable Semiconducting Polymers. *Macromolecules* **52**, 4393–4404 (2019).

41. Balar, N. *et al.* Resolving the Molecular Origin of Mechanical Relaxations in Donor–Acceptor Polymer Semiconductors. *Adv. Funct. Mater.* **32**, 2105597 (2021).

42.   Olla, T. *et al.* Benzothiadiazole Halogenation Impact in Conjugated Polymers, a Comprehensive Study. *Macromolecules* **52**, 8006–8016 (2019).

43.   Reichenbächer, K., Süss, H. I. & Hulliger, J. Fluorine in crystal engineering—"the little atom that could". *Chem. Soc. Rev.* **34**, 22–30 (2005).

44.   Desiraju, G. R. Crystal engineering: A holistic view. *Angew. Chemie - Int. Ed.* **46**, 8342–8356 (2007).

45.   Kroon, R. *et al.* New quinoxaline and pyridopyrazine-based polymers for solution-processable photovoltaics. *Sol. Energy Mater. Sol. Cells* **105**, 280–286 (2012).

46.   Zhang, S. *et al.* The Critical Role of Electron-Donating Thiophene Groups on the Mechanical and Thermal Properties of Donor–Acceptor Semiconducting Polymers. *Adv. Electron. Mater.* **5**, 1–11 (2019).

47.   Roth, B. *et al.* Mechanical properties of a library of low-band-gap polymers. *Chem. Mater.* **28**, 2363–2373 (2016).

48.   Lipomi, D. J., Chong, H., Vosgueritchian, M., Mei, J. & Bao, Z. Toward mechanically robust and intrinsically stretchable organic solar cells: Evolution of photovoltaic properties with tensile strain. *Sol. energy Mater. Sol. cells* **107**, 355–365 (2012).

49.   Li, Y., Tatum, W. K., Onorato, J. W., Zhang, Y. & Luscombe, C. K. Low elastic modulus and high charge mobility of low-crystallinity indacenodithiophene-based semiconducting polymers for potential applications in stretchable electronics. *Macromolecules* **51**, 6352–6358 (2018).

50.   Betancourt, B. A. P., Hanakata, P. Z., Starr, F. W. & Douglas, J. F. Quantitative relations between cooperative motion, emergent elasticity, and free volume in model glass-forming polymer materials. *Proc. Natl. Acad. Sci.* **112**, 2966–2971 (2015).

51.   Soles, C. L., Douglas, J. F., Wu, W., Peng, H. & Gidley, D. W. Comparative specular x-ray reflectivity, positron annihilation lifetime spectroscopy, and incoherent neutron scattering measurements of the dynamics in thin polycarbonate films. *Macromolecules* **37**, 2890–2900 (2004).

52.   Sakai, V. G. & Arbe, A. Quasielastic neutron scattering in soft matter. *Curr. Opin. Colloid Interface Sci.* **14**, 381–390 (2009).

53.   Gerstl, C. *et al.* Quasielastic Neutron Scattering Study on the Dynamics of Poly (alkylene oxide) s. *Macromolecules* **45**, 4394–4405 (2012).

54.   Obrzut, J. & Page, K. A. Electrical conductivity and relaxation in poly (3-hexylthiophene). *Phys. Rev. B* **80**, 195211 (2009).

55.   Guilbert, A. A. Y. *et al.* Temperature-dependent dynamics of polyalkylthiophene conjugated polymers: A combined neutron scattering and simulation study. *Chem. Mater.* **27**, 7652–7661 (2015).

56.   Zhan, P. *et al.* Side chain length affects backbone dynamics in poly (3-alkylthiophene) s. *J. Polym. Sci. Part B Polym. Phys.* **56**, 1193–1202 (2018).

57.   Wolf, C. M. *et al.* Assessment of molecular dynamics simulations for amorphous poly (3-hexylthiophene) using neutron and X-ray scattering experiments. *Soft Matter* **15**, 5067–5083 (2019).

58.   Meng, L. *et al.* Organic and solution-processed tandem solar cells with 17.3% efficiency. *Science (80-.).* **361**, 1094–1098 (2018).

59.   Wang, Z. *et al.* The coupling and competition of crystallization and phase separation, correlating thermodynamics and kinetics in OPV morphology and performances. *Nat. Commun.* **12**, 1–14 (2021).

60.   Liu, Q. *et al.* 18% Efficiency organic solar cells. *Sci. Bull.* **65**, 272–275 (2020).

61.   Hultmark, S. *et al.* Suppressing Co-Crystallization of Halogenated Non-Fullerene Acceptors for Thermally Stable Ternary Solar Cells. *Adv. Funct. Mater.* **30**, 2005462 (2020).

62.   Hu, H. *et al.* The Role of Demixing and Crystallization Kinetics on the Stability of Non-Fullerene Organic Solar Cells. *Adv. Mater.* **32**, 2005348 (2020).

63.   Marina, S. *et al.* Polymorphism in Non-Fullerene Acceptors Based on Indacenodithienothiophene. *Adv. Funct. Mater.* **31**, 2103784 (2021).

64.   Yu, L. *et al.* Diffusion-Limited Crystallization: A Rationale for the Thermal Stability of Non-Fullerene Solar Cells. *ACS Appl. Mater. Interfaces* **11**, 21766–21774 (2019).

65.   Mamontov, E. & Herwig, K. W. A time-of-flight backscattering spectrometer at the Spallation Neutron Source, BASIS. *Rev. Sci. Instrum.* **82**, 85109 (2011).

66.   Azuah, R. T. *et al.* DAVE: a comprehensive software suite for the reduction, visualization, and analysis of low energy neutron spectroscopic data. *J. Res. Natl. Inst. Stand. Technol.* **114**, 341 (2009).

67.   Sharma, A., Pan, X., Campbell, J. A., Andersson, M. R. & Lewis, D. A. Unravelling the Thermomechanical Properties of Bulk Heterojunction Blends in Polymer Solar Cells. *Macromolecules* **50**, 3347–3354 (2017).

68.   McClave, J. T. & Sincich, T. *Statistics*. (Pearson education, 2006).

69.   Plimpton, S. Fast parallel algorithms for short-range molecular dynamics. *J. Comput. Phys.* **117**, 1–19 (1995).

70.   Wang, J., Wolf, R. M., Caldwell, J. W., Kollman, P. A. & Case, D. A. Development and testing of a general Amber force field. *J. Comput. Chem.* **25**, 1157–1174 (2004).

5. MECHANICAL PROPERTIES AND STRAIN-INDUCED DEFORMATION MECHANISM OF CONJUGATED POLYMERS

Donor-acceptor (D-A) type semiconducting polymers have shown great potential for the application of deformable and stretchable electronics in recent decades. However, due to their heterogeneous structure with rigid backbones and long solubilizing side chains, the fundamental understanding of mechanical properties and their molecular picture upon tensile deformation are still less investigated. Utilizing both experimental and computational measurements, in this chapter, we first characterize the elastic modulus of diketopyrrolopyrrole (DPP)-based D-A polymer with varied side chains under tensile deformation. Then, the molecular orientation of polymer systems under tensile deformation is investigated, where the influence of side-chain length on their thermal and mechanical response is explored to facilitate an in-depth understanding of the deformation mechanism.[1,2]

5.1. Introduction

Flexible and wearable electronics that are conformable to soft surfaces like human skin have raised tremendous research attention.[3–6] Semiconducting polymers are unique species due to their high electrical performance, solution processability, and intrinsic mechanical stretchability.[7–11] Previously, many efforts have been made to improve their charge transport by enhancing the polymer chain alignment.[12–19] Both mechanical stretching and shear coating methods have shown promise in boosting the charge carrier mobility along the alignment direction for semiconducting polymers, especially on traditional conjugated polymers (CPs) like poly(3-hexylthiophene) (P3HT).[18–24] Strain-induced chain alignment, however, is still less explored for the emerging high-performance D-A type CPs with much rigid polymer backbones. The fundamental understanding

of the deformation-thermal/mechanical property-morphology-performance relationship is vital for the engineering of future wearable electronics.

Typical CPs have a semicrystalline nature with the backbone consisting of alternating single-and double-bonds, which enables both intra- and intermolecular charge transport. When compared with traditional semicrystalline polymer, i.e., polyethylene (PE), with a persistence length (l_p) of 7 ~ 9 Å that can easily fold, the backbone of P3HT with an l_p of 3 nm requires 7~8 consecutive thiophene rings in a *sync* conformation to turn 180°.[25–27] For D-A polymers with large fused rings on the backbone, they are even harder to bend (i.e., l_p (PDPPDTT) ≈ 8 nm).[28] Thus, the molecular picture of D-A polymer chains is more likely to be semi-rigid rods that are hard to entangle with each other.[29–31] Under a thin film state, a complex 3D heterogeneous microstructure is commonly demonstrated with three main characteristic domains: crystalline region, local aggregate, and amorphous region. The crystalline domain consists of layers of lamellae with flexible side chains serving as "spacer" in between. Inside of each lamella is stacked polymer backbones through interchain π-π interaction. Previous studies also suggest these crystalline domains are connected through "tie-chains" that can bear load and transport charges.[7,32–34] Local aggregates are also described, resulting from intrachain and interchain excitonic coupling, namely J- and H-aggregates, respectively.[35]

For PE with well-defined crystalline regions, the polymer chain deformation mechanism has been mostly studied through transmission electron microscopy (TEM), small-angle neutron scattering (SANS), and hard X-ray scattering (energy > 8 keV) including both small- and wide-angle X-ray scattering (SAXS/WAXS).[36–41] Specifically, TEM provides local atomic/nanometer-level resolution; WAXS is capable of analyzing averaged crystallite orientation, size, and packing distance at a similar size scale; SANS and SAXS can detect averaged long-range order ranging

from 1 nm to hundreds of nm. However, the scattering technique is limited to the detection of ordered crystalline regions. Spectroscopy, instead, can detect polymer chains in both amorphous and crystalline regions that are sensitive to atomic-level bond motion, twisting, or orientation based on the specific light characteristics. For example, polarized variable angle spectroscopic ellipsometry (VASE), polarized Infrared (IR) spectroscopy/Raman spectroscopy/Ultraviolet-visible (UV-vis) optical absorption spectroscopy, and near-edge X-ray absorption fine structure (NEXAFS) techniques have been applied to investigate polymer chain orientation upon shear/strain alignment.[13,17–22,42,43]

To better understand molecular mechanisms, computational techniques (i.e., molecular dynamics simulations) have been utilized to explore the complex behaviors of polymers. In particular, coarse-grained molecular dynamics (CG-MD) simulations allow for "bottom-up" investigations of polymer systems over a longer time and larger length scales,[44,45] by reducing degrees of freedom and eliminating non-essential atomistic details. Over the last few decades, the CG-MD approach has been broadly applied to explore the influences of fundamental molecular parameters on the thermomechanical behaviors of polymers.[46–52] The crystalline morphology of PE under uniaxial tension was explored via CG-MD, and it was shown that polymer chains tend to align in the deformation direction, where the large extension and orientation of the chains were found to affect the crystallization and facilitate the primary nucleation.[53] In another study, a CG-MD model was developed to predict the thermomechanical properties of poly(3-hexylthiophene) (P3HT) polymer,[20] of which the simulation findings were pointed out to be in good agreement with the experimental results. Accordingly, it was shown that the degree of backbone chain alignment in bulk conjugated P3HT polymer is increased as the applied uniaxial strain becomes larger.

Herein, we perform a detailed study on the mechanical properties and chain deformation mechanism for a series of side-chain engineered PDPP-based semi-flexible D-A polymers. We implement experimental measurements and CG-MD simulations to explore the fundamental mechanism of the macroscopic deformation process. Next, polarized UV-vis spectroscopy, NEXAFS, and atomic force microscopy (AFM) are applied to investigate the microstructural chain alignment upon thin-film deformation, which is further confirmed by the CG-MD simulations.

5.2. Methods

In this section, we review the details of experimental and computational techniques utilized in this dissertation. It should be noted that all experimental measurements are performed by our experimental collaborators (Gu group) at The University of Sothern Mississippi (USM).

5.2.1. Materials and Processing

All four PDPPT-based polymers are synthesized following previously reported methods.[54–56] The number-averaged molecular weight is measured by high-temperature gel permeation chromatography (HT-GPC) using trichlorobenzene as the eluent at 160 °C, polystyrene for calibration, viscometer, and light scattering as the detectors. All four polymers are dissolved in chlorobenzene with a concentration of 15 mg/ml upon stirring on the hot plate at 80 °C overnight. A commercially available water-soluble poly(sodium 4-styrenesulfonate) (PSS) is dissolved in deionized water and coated on the bare silicon wafer with a thickness of 30 nm. Then the solution is spin-coated on the PSS-coated silicon substrate at 1000 rpm/s to form a 100 nm thin film. The film thickness was measured by AFM.

5.2.2. Pseudo-free-standing Tensile Test

Dog-bone thin films with a gauge length of 8 cm and a width of 3 cm are fabricated by laser etching. Next, thin-film dog bones are floated on top of the water and stretched at a strain

rate of 5×10^{-4} s^{-1} using a previously described method.[56–58] At least six independent samples are measured for each CPs to provide statistically averaged mechanical properties. The elastic modulus is extracted from the slope of the linear fit of the stress-strain curve using the first 0.5% strain (elastic region). Next, thin-film samples being strained to various degrees are picked up from the water with a washer to form free-standing thin films.

5.2.3. Molecular Dynamics Simulations

The force field parameters of the CG models are determined based on the contributions of the bonded and non-bonded interactions. For the details of CG-MD simulations, readers are directed to Chapter 2. The cohesive energy between particles is regulated via ε parameter, where for each pair of the CG beads in the backbones $\varepsilon = 1.0$, and the pairs of the side groups $\varepsilon = 0.5$. All CG-MD simulations are performed using the Large-scale Atomic/Molecular Massively Parallel Simulator (LAMMPS) software package.[59] The bulk systems of the model are composed of 100 chains, where the backbone of each chain is composed of 30 CG beads and side-chain lengths. Periodic boundary conditions (PBC) are applied in all three directions, and an integration time step $\Delta t = 0.001\tau$ is performed in all simulations. For the equlibration of the system, the total potential energy is first minimized using iterative conjugate gradient algorithm.[60] Then, the equilibration of the bulk polymer model is continued starting at a high-temperature $T = 2.0$ under isothermal-isobaric (NPT) ensemble for the 10^6 time steps where the pressure linearly reduced from the initial 10 to the final 5 in reduced units. Next, the model is further cooled down to the target temperature via NPT under zero pressure for 1.5×10^6 time steps before running for any property calculations. The uniaxial tensile test is performed to obtain the deformation trajectory of the bulk polymer system at a temperature of 0.2 under a constant strain rate of 5×10^{-4}, which is consistent with previously investigated LJ polymer models.[61,62]

5.3. Results and Discussion

5.3.1. Mechanical Performance

In this work, four PDPPT-based D-A polymers with increasing side-chain lengths from C2C6C8 (2-hexyl decyl) to C2C8C10 (2-octyl dodecyl), C2C10C12 (2-decyl tetradecyl) and C2C12C14 (2-dodecyl hexadecyl) are synthesized followed by previously reported procedures (Figure 5.1A).[2] The experimentally-measured mechanical performance of these polymers is investigated using a pseudo-free standing tensile tester. The polymers are spin-coated into a thin film state with a similar thickness of 80 nm, then floated on top of the water to avoid the underlying substrate effect, followed by tensile testing at a fixed strain rate of 5×10^{-4} s^{-1}. Figure. 5.1B exhibits the complete engineering stress-strain curves for all four side chains, which show a clear difference in their viscoelastic behavior. With increased strain, an elastic region first appears, followed by yielding and strain hardening. Despite slightly different yield strain, the strain-hardening phenomenon for short side-chain polymers is more noticeable with a higher slope, or strain hardening modulus, which can be correlated with their lower chain mobility. In addition, the elastic modulus shows an obvious reduction with increasing side-chain length.
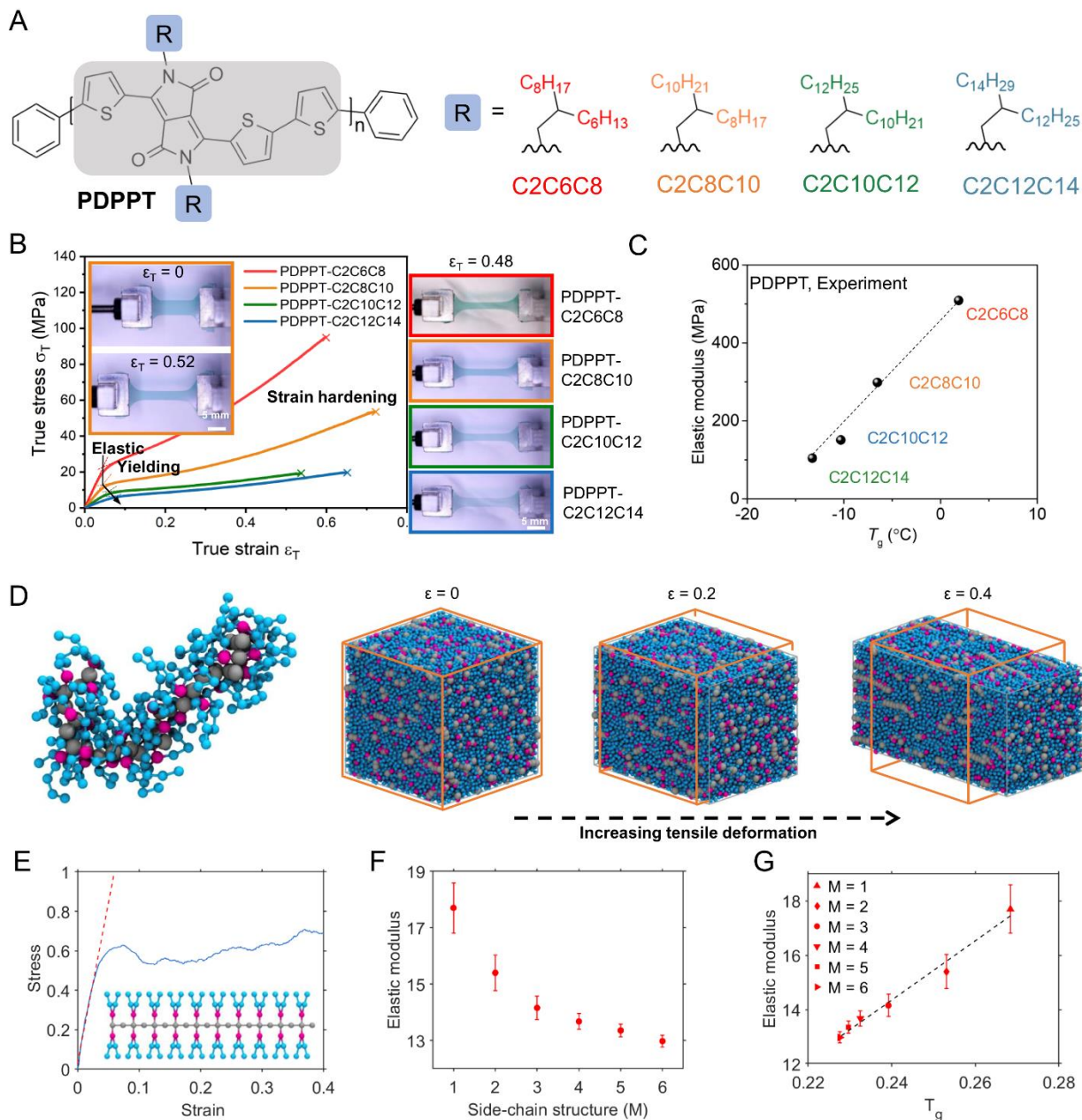
Figure 5.1. Molecular picture and characterization methods for PDPP-based polymers (PDPPT-C2C6C8, PDPPT-C2C8C10, PDPPT-C2C10C12, PDPPT-C2C12C14). (A) Schematics of PDPP polymers with different side-chain structures. (B) True stress-strain curves for four polymers and representative optical images for PDPPT-C2C8C10 under different strains. (C) Summary of experimental results of elastic modulus versus glass transition temperature (T_g). (D) Snapshots of a single representative chain and the CG bulk polymer model under deformation. (E) The stress versus strain curve for CG-MD simulations of $M = 2$ model. Red dashed line represents the linear regime. (F) Simulated elastic modulus versus side-chain length M. (G) Simulated T_g versus side-chain length M. CG-MD simulation results are expressed using the reduced or (LJ) unit.

This phenomenon implies the direct correlation of the mechanical response of D-A CPs to the thermal properties, which was explored in Chapter 4. As Figure 5.1C shows, the elastic modulus is linearly correlated to the glass transition temperature (T_g). On the other hand, the crack onset strain shows no dependence on the elastic modulus or the side-chain length. We hypothesize that such independence results from their molecular weight difference. For viscoelastic polymers, high mechanical deformation mostly relies on chain sliding; thus, the molecular weight plays an important role in determining the extent of elongation.[5] Here, the molecular weights of PDPPT-C2C6C8 (M_n = 88.5 kg/mol) and PDPPT-C2C8C10 (M_n = 76.6 kg/mol) are higher than those of PDPPT-C2C10C12 (M_n = 60.6 kg/mol) and PDPPT-C2C12C14 (M_n = 61.8 kg/mol). Impressively, the PDPPT-C2C8C10 polymer exhibits a record-high crack onset-strain of 105%. To our best knowledge, it is the highest deformability reported for pristine D-A CPs in the literature.

Then, CG-MD simulations are employed to systematically explore the mechanical properties of D-A CPs with varied side-chain lengths (M = 1 to 6) under tensile deformation (Figure 5.1D). An example of the stress-strain curve response of the CG-MD model is reported in Figure 5.1E where the dashed red line is fitted to the linear part of the smoothed curve. In the same manner as experimental results, as is indicated by Figure 5.1F, increasing the side-chain length M ended in a sharp drop in the elastic modulus of the bulk polymers. It should be mentioned that the results of the elastic modulus are obtained as the average of five different simulations with independent initial configurations and the error bars mark the standard deviation. Figure. 5.1G plots elastic modulus versus T_g for polymers with varying side-chain lengths, where a near-linear relationship between elastic modulus and T_g can be observed. The CG-MD results are in good agreement with our experimental findings, demonstrating that the larger side-chain length tends to reduce both elastic modulus and T_g.

5.3.2. Strain-induced Mechanical Alignment

To study polymer chain alignment, all four polymers are spun cast on the silicon substrate to fabricate thin films with a thickness of around 100 nm, followed by tensile testing on the water surface using a previously reported pseudo-free-standing tensile tester.[2,56–58,63] Figure 5.1B shows true stress (σ_T) vs. true strain (ε_T) curves of the four polymers, with optical images of PDPPT-C2C8C10 thin films at various strains highlighted to show the deformation behavior. It is observed that polymers with shorter side-chain lengths are easier to deform along the width direction. All four polymers demonstrated similar viscoelastic stress-strain behaviors with three regions: an initial linear elastic response, mechanical yielding, and strain hardening. Further plastic deformation led to permanent mechanical failure. It is also obsereved that fracture strain is not directly affected by the side-chain length while molecular weight effect was more dominant, as demonstrated in our previous publication.[56] The mechanical yielding point is not evident due to the smooth transition in the stress-strain curve and can only be extrapolated from the slope difference before and after yielding (Figure 5.1B). Interestingly, the strain softening behavior is not observed in any tensile tests, while it existed in most traditional polymers like polystyrene and PE.[64,65] The strain-softening behavior in polymer glass was attributed to mechanically generated disorder, while for semicrystalline PE, crystallographic deformations like chain slip, martensitic transformation, and potential cavitation are the main cause.[38–40] Thus, the lack of strain softening in PDPPs could result from their less mechanical disorder and a lower degree of crystallinity.[7]

Importantly, strain hardening is observed with continuously increased slope at around ε_T > 0.35, while increased side-chain length led to a lower slope. The degree of strain hardening can be represented by the strain hardening modulus G_R, which was reported to be affected by the distance between T_g and testing temperature (T - T_g); the entanglement density of the amorphous

phase; the existence of highly stretched and oriented chains.[64,66,67] On the other hand, the degree of crystallinity was found to play a negligible role in the G_R of semicrystalline polymers.[64,67,68] Due to the semi-flexible nature of D-A polymer chains, the traditional Gaussian network theory of entropic elasticity cannot be applied here. Instead, we performed temperature-dependent tensile tests on PDPPT-C2C8C10 at 20 ℃, 30 ℃, and 40 ℃ to investigate the temperature effect. To understand the effect of crystallinity, thermal annealed PDPPT-C2C8C10 under three temperatures (80 ℃, 140 ℃, and 200 ℃) are also tested. We observe that the strain hardening region was slightly affected at a higher testing temperature, while the degree of crystallinity shows a negligible influence. Thus, we hypothesize the various strain hardening behavior for these four side-chain engineered polymers is a result of the entanglement density effect: the entanglement density of amorphous chains decreases with increased volume taken by the solubilizing side-chains.

5.3.3. Morphological Experimental Measurements

After strain alignment, multimodal characterization methods are applied to aligned thin films to understand the molecular-level chain alignment mechanism in a transmission geometry (Figure 5.2). The sample is scooped out of the water with a hollow washer, followed by air drying. In addition to experiments, CG-MD simulations of tensile deformation are carried out to explore the chain alignment of CPs in a bulk system. Figure 5.1D shows a representative CG model of polymer chain informed by PDPP and several snapshots of the deformed simulation box at different strains. In this section, we first investigate the experimental measurements performed by our collaborators, the Gu group at USM. Then, we will discuss the computational techniques utilized to study chain alignment at the molecular level.
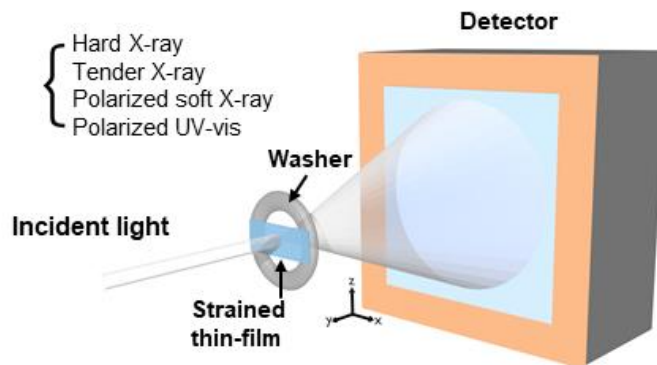
Figure 5.2. Schematic of multimodal morphological characterization tools on tensile strained thin films supported by a hollow washer.

Based on the abovementioned three tensile test regions, the molecular orientation is investigated by several morphological characterization tools at five strains: $\varepsilon_T = 0$, 0.18, 0.34, 0.47, 0.59. Transmission wide/small-angle hard/tender X-ray scattering, polarized UV-vis absorption spectroscopy, transmission NEXAFS, and atomic force microscopy (AFM) are applied to detect different regions of interest in the polymer thin film. Namely, bulk averaged crystallite orientation; bulk averaged whole chain orientation; chain orientation on thin-film surface. To provide a fair comparison of chain alignment and anisotropy determined by different techniques, a two-dimensional (2D) Herman's orientation parameter f is introduced by prescribing that chain orientation takes place in a 2D plane, owing to the semi-flexible nature of PDPPT polymer chains:

$$f = 2 < \cos^2\theta > -1 \tag{24}$$

where θ is the angle between polymer chain orientation direction and direction of interest. For clarity purposes, the molecular orientation of the PDPPT-C2C8C10 polymer is first discussed, followed by comparisons with the other three polymers.

5.3.3.1. Polarized UV-vis Optical Absorption Spectroscopy

As the orientation of polymer crystallites only represents a small fraction of the entire polymer film, it is vital to understand the chain deformation mechanism for amorphous polymer chains. A polarized optical spectroscopy technique was commonly performed to investigate polymer chain orientation based on the absorption anisotropy along/perpendicular to the strain direction.[18] Such anisotropy can be quantified by dichroic ratio R, which is the ratio of peak absorbance along with polarized light to the peak absorbance perpendicular to polarized light. In the meantime, 2D Herman's orientation parameter f can be calculated as:

$$f = \frac{R - 1}{R + 1} \tag{25}$$

Polarized UV-vis absorption spectroscopy had been widely applied to study the orientation of CP chains due to their characteristic emission peaks. Previously developed HJ-aggregate model successfully described that the competition between intra-and intermolecular coupling, which is sensitive to the nature and magnitude of disorder, leads to different J- and K-aggregate behavior.[35,69] Figure 5.3A indicates a schematic of the test setup, where the polarized light parallel and perpendicular to the strain direction can capture the motion of the entire chain. The absorption spectrum for PDPPT-C2C8C10 thin films under strain was plotted in Figure 5.3B, with the 0→0 and 0→1 transition occurring at 820 nm and 760 nm, respectively. Surprisingly, the degree of orientation for the whole chain is limited, with an f of 0.14 at $\varepsilon_T = 0.59$, which suggested the averaged anisotropy for strain-aligned polymer chains is pretty low (Figure 5.3C). Considering the high level of strain applied to the thin film, such low orientation is not expected, while one explanation could be that the deformation process for free-standing thin films involved substantial chain slippage. This observation is in contrast with previous literature demonstrating an f value of 0.5 obtained from polarized UV-vis at $\varepsilon_T = 0.59$ in stretch-aligned P3HT thin film supported by a

polydimethylsiloxane (PDMS) substrate.[19] Such a difference in f could come from two origins: 1. P3HT exhibited more than 50% crystallites; thus, the tie chains connecting these regions experienced a significant alignment, while the degree of crystallinity was low for PDPPT-based polymers;[70,71] 2. When bonded to the PDMS substrate, polymer thin films tended to align more uniformly along one direction with Poisson's ratio effect only along with the film thickness, while free-standing films experienced narrowing behavior along the width direction, leading to significant chain slippage without a high anisotropy. To prove the statement above, PDMS-supported PDPPT-C2C8C10 thin-films are prepared, and an orientation parameter f of 0.36 is detected at the same strain ($\varepsilon_T = 0.59$).
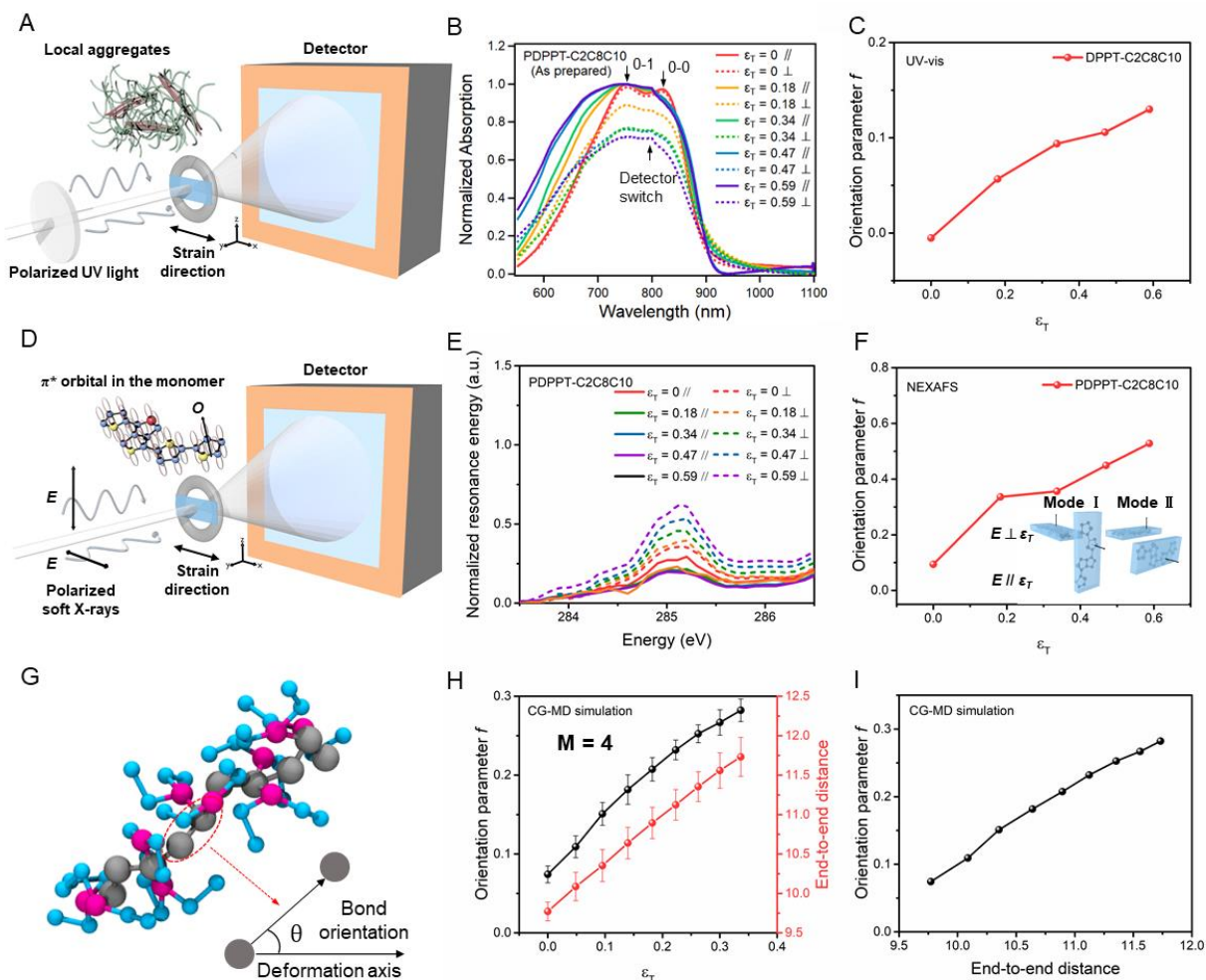
Figure 5.3. Characterization of chain orientation through UV-vis, polarized X-ray, and CG-MD simulation. (a-c) UV-vis absorption spectroscopy for PDPPT-C2C8C10 polymer under various strains. (a) Schematic of incident polarized UV light transmitted through polymer thin films. (b) 1D UV-vis absorption plot at different wavelengths. (c) Herman's orientation parameter f under strain. (d-f) NEXAFS experiment for PDPPT-C2C8C10 polymer under various strains. (d) Schematic of incident polarized soft X-rays transmitted through polymer thin films. E represents the electric field direction, and O represents the normal direction of the aromatic plane. (e) Normalized resonance energy under different incident energies for $E /\!/ \varepsilon_T$, and $E \perp \varepsilon_T$ direction. The peak at around 285.2 eV represents the 1s to π^* transition. (f) Herman's orientation parameter f under strain. The inset shows two polymer chain orientation modes, Mode I and Mode II, under strain. (g-i) CG-MD simulation for the M = 4 model. (g) Schematic of a single polymer chain with a defined angle between the bond and deformation directions. (h) Herman's orientation parameter f and end-to-end distance under strain. (i) Relationship between Herman's orientation parameter and end-to-end distance.

5.3.3.2. Transmission NEXAFS

The transmission NEXAFS technique is applied to supplement UV-vis spectroscopy by detecting the polymer backbone rotation for the entire chain. Different from tender X-rays using energy near the sulfur K-edge, soft X-rays with energy near the carbon K-edge can detect absorption signals from carbon atoms. Specifically, for CPs with multiple ring structures in the backbone, the C=C 1s→π* transition is a signature fingerprint that indicates the orientation of aromatic planes. Figure 5.3D demonstrates the electric field vector $\vec{E}$ for linearly polarized soft X-ray beam, as well as the 1s→π* transition dipole moment $\vec{O}$ perpendicular to the plane of the aromatic ring. The resonance intensity detected on the photodetector is proportional to the overlap between these two vectors:

$$I \propto |\vec{E} \cdot \vec{O}|^2 \propto \cos^2\theta \qquad (26)$$

where θ is the angle between $\vec{E}$ and $\vec{O}$. Thus, the dichroism of such transition can be used to determine the molecular orientation.[72,73] It should be noted that the orientation determined here only considers polymer chains with an aromatic plane that is parallel to the film thickness direction

Figure 5.3E implies the 1s→π* transition peak for strained PDPPT-C2C8C10 thin films, while the complete NEXAFS spectrum with an energy range from 0.27 keV to 0.4 keV, followed by previously reported procedures.[72] The parallel/perpendicular direction is referring to the angle between $\vec{E}$ and strain ε_T (Figure 5.3D). From the anisotropic peak resonance energy at 285.2 eV, an orientation parameter f can be calculated by $R = \frac{I_\perp - I_\parallel}{I_\perp + I_\parallel}$ (Figure 5.3F). Again, the unstrained film showed a non-zero f value of 0.09, which could be resulted from processing. Upon strain alignment, f continuously increases with ε_T until a moderate value of 0.53 at $\varepsilon_T = 0.59$, indicating an efficient backbone rotation mechanism where the majority of polymer chains have an aromatic

plane rotated with its normal $\vec{O}$ perpendicular to strain. Two primary rotation modes are also drawn in Figure 5.3F ($\vec{E} \parallel \varepsilon_T$ and $\vec{E} \perp \varepsilon_T$). For polymer chains in the crystalline region, mode I corresponds well with an increased population of Type III crystallites, while mode II is less preferred as judged by the (100) lamellar packing direction. On the contrary, mode II is more dominant than mode I for amorphous polymer chains due to the low degree of anisotropy found in UV-vis measurement.

5.3.3.3. *Atomic Force Microscopy*

The film surface morphology was investigated through AFM height images. Similar to previous publications, fiber-like structures can be observed all over the surface, while small, randomly shaped aggregates are also present.[74] Upon strain alignment, the fiber orientation is less visible due to the high mobility of polymer chains. The local aggregates, on the other hand, showed evident deformation with their shapes being elongated along the stretching direction. This observation provides direct evidence for thin-film alignment behavior.

5.3.4. CG-MD Simulation

By employing the CG-MD modeling, the orientation of the polymer chains is characterized by a 3D Herman's function:

$$f = \frac{3 < \cos^2\theta > -1}{2} \tag{27}$$

where θ is the formed angle between the bond vector in the polymer chain (backbone) and the deformation axial (Figure 5.3G). Then, the orientation factor f can be defined as an average of all CG backbone "bond" vectors' orientation values in the bulk simulation. Besides the orientation parameter, the end-to-end distance of the polymer backbone during deformation is examined, which is found correlated to the orientation factor. In this study, the molecular orientation of the CG model is presented for the CG bulk polymer model with a side-chain length (M) of 4 at different

strains. Figure 5.3H indicates that, as the tensile strain increases, the backbone chains tend to align in the deformation axial and exhibit a higher orientation parameter. Expectedly, the rise in the orientation parameter is accompanied by the increase in the end-to-end distance, shown in the right axis of Figure 5.3H. The orientation parameter and end-to-end distance are found to have a near-linear correlation, as shown in Figure 5.3I. The current results are consistent with the previous CG-MD studies[20] on the P3HT polymer and nanocellulose film,[75] where the backbone chains were found to align in the deformation axis by increasing the tensile strain.

5.3.5. Side-chain Length Effect

The side-chain effect is also investigated by performing the same measurements above on the other three PDPPT-based polymers with side chains of C2C6C8, C2C10C12, and C2C12C14, as well as computational calculations via CG-MD. Previous works have shown that side-chain length can significantly affect the thin film microstructure (crystallographic packing, aggregation behavior, degree of crystallinity) and the device's performance.[3,76–81] From hard X-ray scattering, we observe a similar influence on unstrained samples, i.e., longer side-chains led to higher lamellar packing distance, less visible (010) peak, distorted π-π stacking distance, and a lower degree of crystallinity (supplementary figures in our paper[1]). However, the side-chain length effect on crystalline domain orientation upon strain was not reported for D-A polymers. The f value for (100), (010), and amorphous peak at each strain is very close for all three polymers with longer side-chain lengths, while the orientation parameter of (010) and amorphous peak for the shortest side-chain polymer, PDPPT-C2C6C8 is higher than the others (Figure 5.4A-C). This "inconsistency" is attributed to the preferred edge-on morphology for PDPPT-C2C6C8 upon casting on the silicon substrate. At the same time, all three other polymers showed a preferred face-on morphology, as reported by our previous publication.[2] Once the thin film was floated from the

substrate, the predominant edge-on polymer chains with aromatic planes perpendicular to the substrate were susceptible to in-plane strain due to lamellar rotation.
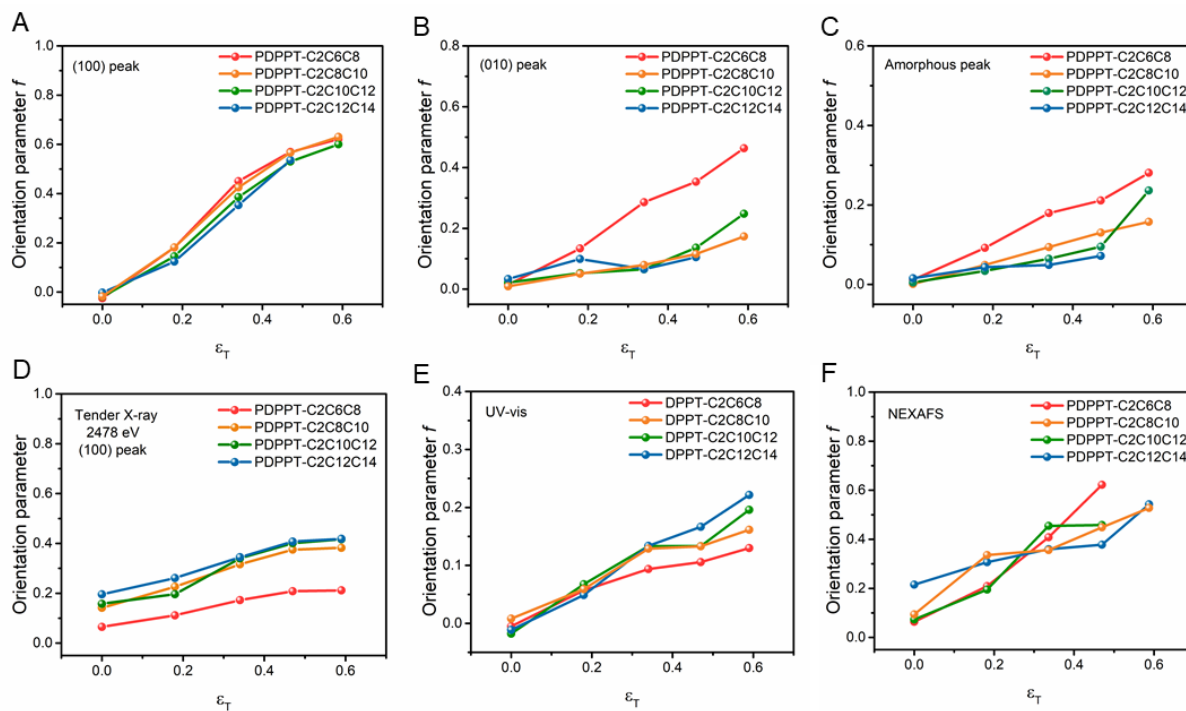
Figure 5.4. Side-chain length effect on Herman's orientation parameter f detected by different experimental techniques for PDPPT-based polymers. (A) (100) peak, (B) (010) peak, and (C) amorphous halo from wide-angle hard X-ray scattering. (D) (100) peak from wide-angle tender X-ray scattering at 2478 eV. (E) UV-vis absorption spectroscopy. (F) NEXAFS.

Similarly, the backbone orientation in polymer crystallites measured by tender X-ray scattering shows negligible dependence on the side-chain length (Figure 5.4D). On the other hand, the whole chain orientation detected by UV-vis spectroscopy presented slight dependence on side-chain length, whereas polymers with longer side chains exhibit a slightly higher degree of orientation (Figure 5.4E). At first glance, such observation is unexpected since one would imagine PDPPT-C2C6C8 polymer with a higher chain rigidity and T_g to be easier to align than the other three polymers. Considering the overall low degree of orientation for all DPPT-based polymer chains, we believe this is due to the "lubrication effect" from longer side chains that lowers the

energetic penalty barrier required for chain slippage in the amorphous phase. Both NEXAFS and AFM show the negligible influence of side-chain length on the backbone rotation behavior and fiber-like structure alignment, respectively (Figure 5.4F).

To further explore the side chain influence on the strain-induced CPs chain alignments at the molecular level, CG-MD simulations are employed. The simulated models can easily provide physical insight into the orientation mechanism of backbones and side chains separately (see Figure 5.5. Similar to experimental measurements, the side chain influence on the chain deformation mechanism is not dominant (Figure 5.5A-C). Simulation results indicate slight dependence on side-chain length at larger strains where longer side chains exhibit a slightly higher degree of orientation.
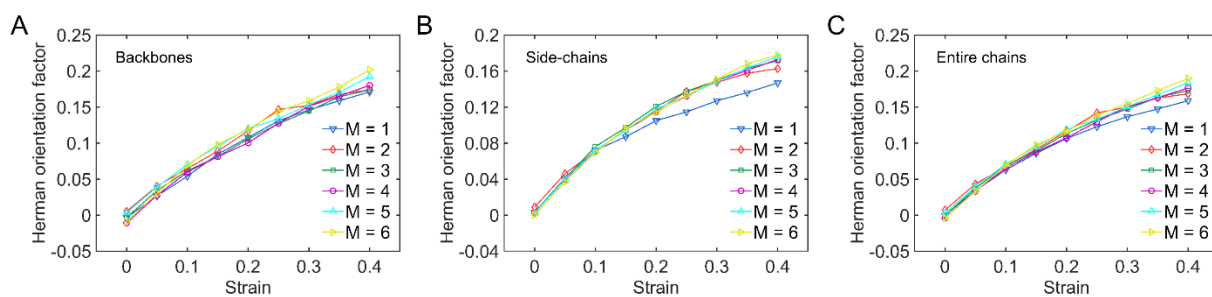
Figure 5.5. Side-chain length effect on Herman's orientation parameter f for (A) backbones, (B) side chains, and (C) entire chains of conjugated polymers detected by coarse-grained molecular dynamics simulations.

Furthermore, as it is indicated in Figure 5.5A and B, a more significant shift in the orientation parameter values is observed for the side chain at higher strains, compared to backbones orientation. This can occur due to differences in the rigidity of the backbones and side chains of CPs. Figure 5.6A and B show almost the same Gaussian-like distribution of the orientation parameters for the backbones of CG-MD models with different side-chain lengths, where increasing the tensile deformation increases the mean value of the distribution curve. Here,

the slight difference in the mean values of the distribution for $M = 6$ model can be occurred due to "lubrication effect" which is discussed in the previous discussion. However, a clear shift in the mean value and distribution of orientation parameters is observed for the side chains compared to those results for the backbones. As Figure 5.6C and D exhibit, upon deformation, a noticeable right-shifted trend in the distribution results is observed, which is rooted in the differences in chain rigidity.
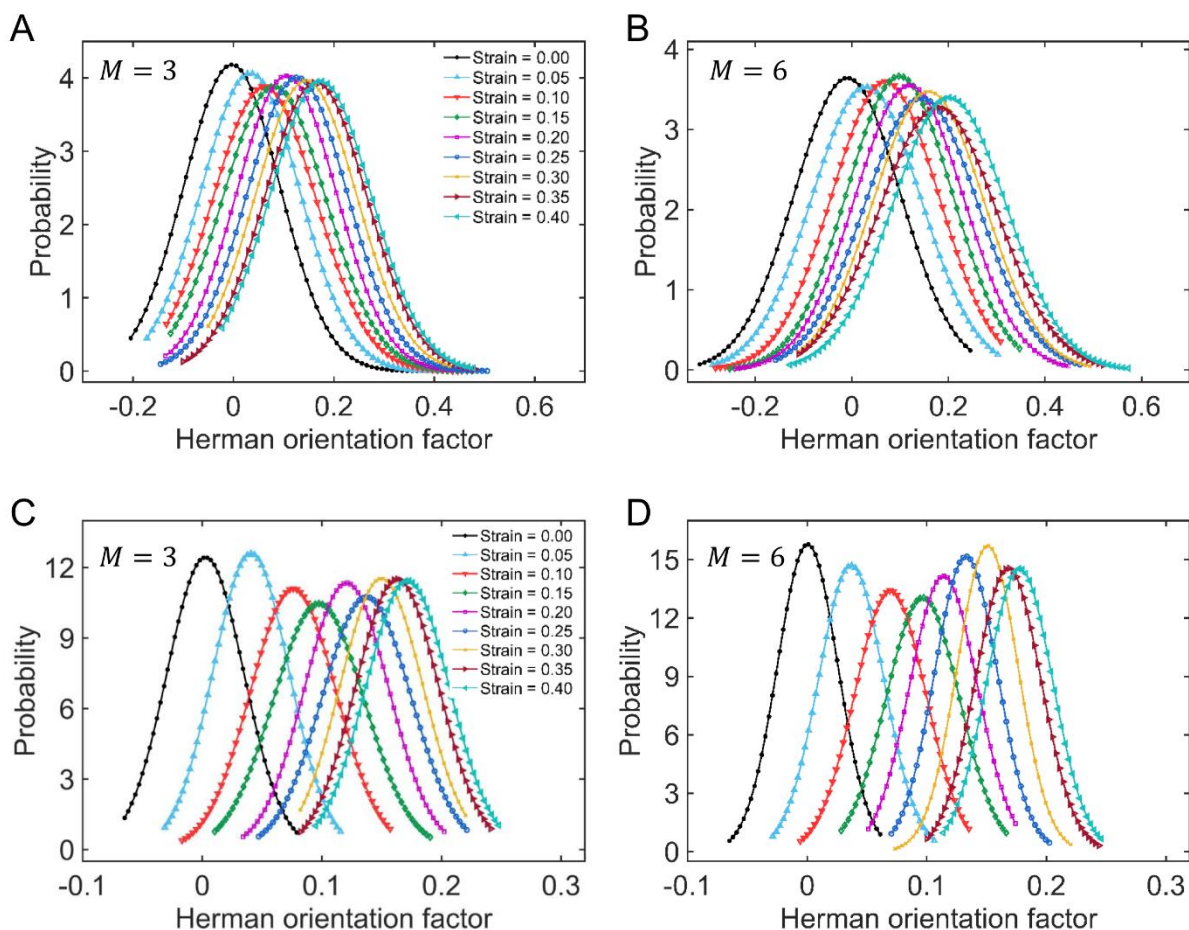
Figure 5.6. Normal distribution of Herman's orientation parameter for (A) backbones of $M = 3$ model, (B) backbones of $M = 6$ model, (C) side chains of $M = 3$ model, (D) side chains of $M = 6$ model of conjugated polymers calculated by coarse-grained molecular dynamics simulations.

5.3.6. Further Discussion on Deformation Mechanism of D-A Polymers

For the past decades, the chain deformation mechanism of PE had been thoroughly investigated due to its simple molecular structure and semicrystalline nature.[36–41] Detailed studies based on both tensile and compression tests showed that the deformation came from a synergic contribution of both rubbery amorphous and hard crystalline domains. The initial deformation mostly relied on amorphous components, such as interlamellar shear, interlamellar separation, and lamellar stack rotation, which were reversible to a large extent. Followed by the elastic response, mechanical yielding and strain softening occurred due to crystallographic deformations.[38–40] The further alignment would cause cavitation, lamellae fragmentation, and fibrillation coupled with the strain hardening behavior.[64,67,68] The degree of crystallinity significantly affected the contribution from crystalline and amorphous domains to deformation. The molecular picture upon deformation was different for P3HT polymer with relatively rigid backbones and a high degree of crystallinity; no strain softening, cavitation or fibrillation were observed.[57,82] Chen *et al.* proposed the deformation of P3HT associated with crystallographic slip along (010)[001] direction, while side-chain length could change the slip direction to (100)[001] for poly(3-dodecylthiophene) (P3DDT).[22]

In this work, PDPPT-based polymers, with a much more rigid backbone, exhibit a limited degree of crystallinity and sub-room-temperature T_g. Figure 5.7 shows the proposed chain alignment mechanism based on the abovementioned stress-strain behavior and molecular orientation. In region I, the initial elastic deformation is much shorter than that of PE; our previous publication had shown significant hysteresis behavior for both P3HT and PDPP-based polymers before $\varepsilon_T = 0.03$.[57] NEXAFS demonstrates a backbone rotation mechanism, suggesting the aromatic plane preferred to lie parallel to the strain direction (Figure 5.3F). Despite the highly

oriented crystallites, the whole chain orientation is limited, as shown by UV-vis, which is attributed to considerable chain slippage in the amorphous region. Thus, the deformation in region II mainly involved crystallite rotation with amorphous chain slippage (Figure 5.7B). In region III, the extent of lamellar rotation tends to reach a plateau with an $f = 0.65$, while both backbone rotation and whole chain orientation did not show obvious saturation. This observation can be explained by the relatively low degree of crystallinity in PDPPT-based polymers. The side-chain length effect on different crystallographic slip mechanisms observed between P3HT and P3DDT was not presented in PDPPTs. The pole figure analysis for (100), (010), and amorphous peak showed a similar crystallographic rotation mechanism for polymers with different side-chain lengths, while longer side chains provided a stronger lubrication effect and allowed for a higher f for the whole chain.
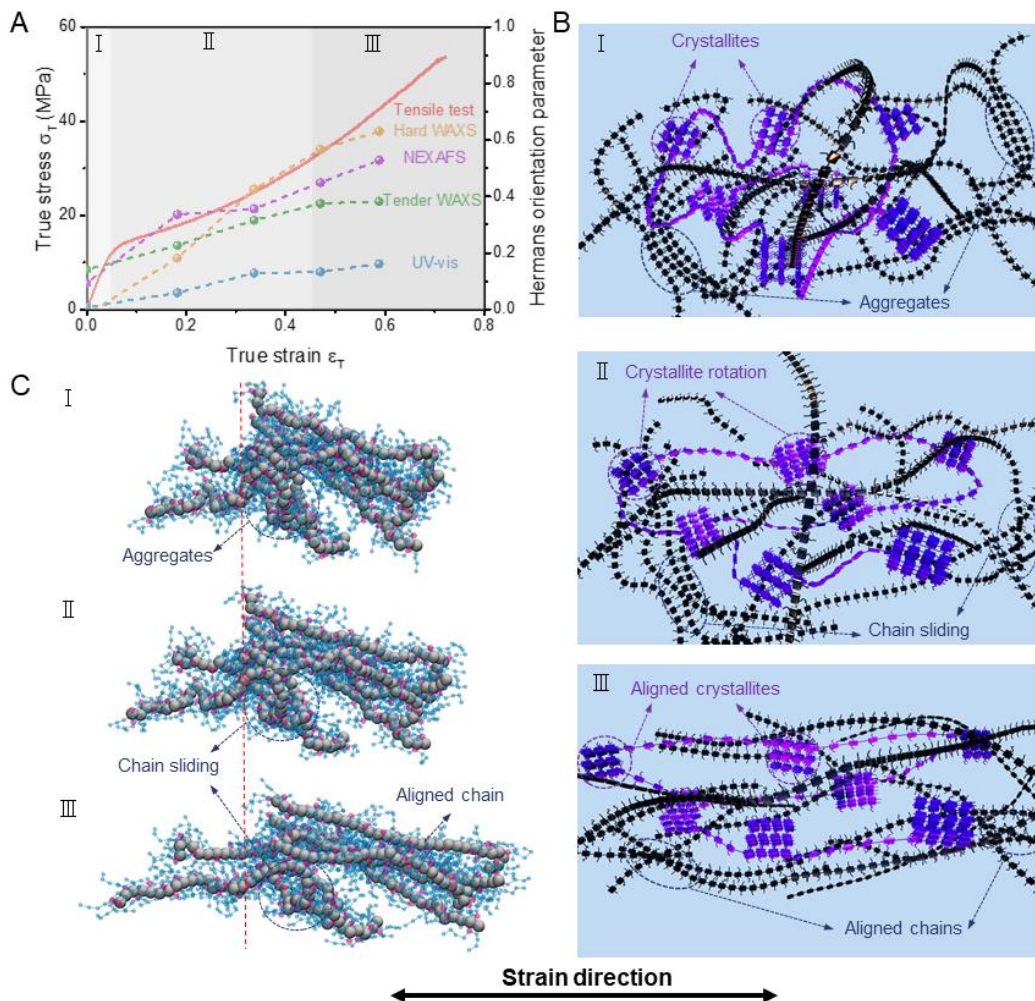
Figure 5.7. Chain alignment mechanism for PDPP-based polymers. (A) Stress-strain response and summarized Herman's orientation parameter for PDPPT-C2C8C10 polymer under strain. I: Initial elastic region; II: Yielding; III: Strain hardening. (B) Schematics of deformation mechanism, including crystallite orientation, chain alignment, and chain sliding. (C) Snapshots of polymer conformations showing the chain alignment and sliding during deformation in the bulk CG-MD simulations.

To further explore our experimental results via MD simulations, a CG model is utilized which mimics the essential structural features of the PDPPT-based polymer chain. Figure 5.7C shows different snapshots of a group of adjacent chains through the tensile simulation. Snapshots are presented for different applied strains of 0, 0.2, and 0.4 that are consistent with the probed three regions of stress-strain behavior obtained from the experimental results (Figure 5.7A). Before

deformation, the random orientation of the polymer chains is observed at zero strain. As the strain increases to 0.2 (region II), the applied deformation causes polymer chain-sliding, and chain-torsional motions ended in a higher alignment of the backbones in the deformation axial. As the tensile simulation proceeds and reaches the strain of 0.4, chains are largely extended and oriented to the deformation direction (region III), where backbone-sliding is found less restricted, and sliding motion becomes smoother due to the plastic behavior of the bulk system. This trend was presented quantitatively in Figure 5.3H, where extended chains at higher strains are found to have larger orientation parameters and end-to-end distances. The simulation result of the backbone orientation is in line with our experimental results, where the alignment slowly plateaus with increased deformation.

5.4. Conclusion

Developed upon experimental techniques and CG-MD simulations, we systematically explore the mechanical properties and chain deformation mechanism of PDPPT-based polymers and the thermomechanical-structure-property-morphology performance relationships. Both experiments and CG-MD simulations confirm the reducing influence of the side-chain length on the elastic modulus, in which the reducing trend is linearly correlated to T_g. Next, The macroscopic thin-film deformation is closely correlated with their microscopic origin through detailed molecular orientation analysis. Two primary strain-induced deformation mechanisms are addressed: highly oriented crystalline domains and substantial chain slippage in the amorphous domain. Specifically, the lamellar rotation is determined to be the main alignment pathway for crystallites, in which the backbone orientation is much lower due to the nonlinearity of PDPPT chains. Meanwhile, the backbone rotation is identified to be part of the whole chain deformation, with their aromatic planes rotated towards the parallel-to-strain direction. We believe such a

fundamental understanding of the chain deformation mechanism for PDPPT-based polymers can serve as a platform and provide more insights into the semi-rigid D-A polymer design for the application of stretchable electronics.

5.5. References

1. Zhang, S. *et al.* Molecular Origin of Strain-Induced Chain Alignment in PDPP-Based Semiconducting Polymeric Thin Films. *Adv. Funct. Mater.* **31**, 2100161 (2021).

2. Zhang, S. *et al.* Toward the Prediction and Control of Glass Transition Temperature for Donor–Acceptor Polymers. *Adv. Funct. Mater.* **2002221**, 2002221 (2020).

3. Oh, J. Y. *et al.* Intrinsically stretchable and healable semiconducting polymer for organic transistors. *Nature* **539**, 411–415 (2016).

4. Chortos, A., Liu, J. & Bao, Z. Pursuing prosthetic electronic skin. *Nat. Mater.* **15**, 937–950 (2016).

5. Root, S. E., Savagatrup, S., Printz, A. D., Rodriquez, D. & Lipomi, D. J. Mechanical Properties of Organic Semiconductors for Stretchable, Highly Flexible, and Mechanically Robust Electronics. *Chem. Rev.* **117**, 6467–6499 (2017).

6. Bao, Z. & Chen, X. Flexible and Stretchable Devices. *Adv. Mater.* **28**, 4177–4179 (2016).

7. Noriega, R. *et al.* A general relationship between disorder, aggregation and charge transport in conjugated polymers. *Nat. Mater.* **12**, 1038–1044 (2013).

8. Mei, J., Diao, Y., Appleton, A. L., Fang, L. & Bao, Z. Integrated materials design of organic semiconductors for field-effect transistors. *J. Am. Chem. Soc.* **135**, 6724–6746 (2013).

9. Paterson, A. F. *et al.* Recent Progress in High-Mobility Organic Transistors: A Reality Check. *Adv. Mater.* **30**, 1801079 (2018).

10. Vezie, M. S. *et al.* Exploring the origin of high optical absorption in conjugated polymers. *Nat. Mater.* **15**, 746–753 (2016).

11. Venkateshvaran, D. *et al.* Approaching disorder-free transport in high-mobility conjugated polymers. *Nature* **515**, 384–388 (2014).

12.   Gu, X., Shaw, L., Gu, K., Toney, M. F. & Bao, Z. The meniscus-guided deposition of semiconducting polymers. *Nat. Commun.* **9**, 534 (2018).

13.   Diao, Y. *et al.* Flow-enhanced solution printing of all-polymer solar cells. *Nat. Commun.* **6**, 7955 (2015).

14.   Zhao, Y. *et al.* Continuous Melt-Drawing of Highly Aligned Flexible and Stretchable Semiconducting Microfibers for Organic Electronics. *Adv. Funct. Mater.* **28**, 1705584 (2018).

15.   Persson, N. E., Engmann, S., Richter, L. J. & Delongchamp, D. M. In Situ Observation of Alignment Templating by Seed Crystals in Highly Anisotropic Polymer Transistors. *Chem. Mater.* **31**, 4133–4147 (2019).

16.   Park, K. S. *et al.* Tuning conformation, assembly, and charge transport properties of conjugated polymers by printing flow. *Sci. Adv.* **5**, eaaw7757 (2019).

17.   Wu, D. *et al.* Blade Coating Aligned, High-Performance, Semiconducting-Polymer Transistors. *Chem. Mater.* **30**, 1924–1936 (2018).

18.   O'Connor, B. *et al.* Anisotropic structure and charge transport in highly strain-aligned regioregular poly(3-hexylthiophene). *Adv. Funct. Mater.* **21**, 3697–3705 (2011).

19.   O'Connor, B. T. *et al.* Morphological origin of charge transport anisotropy in aligned polythiophene thin films. *Adv. Funct. Mater.* **24**, 3422–3431 (2014).

20.   Root, S. E., Savagatrup, S., Pais, C. J., Arya, G. & Lipomi, D. J. Predicting the Mechanical Properties of Organic Semiconductors Using Coarse-Grained Molecular Dynamics Simulations. *Macromolecules* **49**, 2886–2894 (2016).

21.   Awartani, O. M. *et al.* Anisotropic Elastic Modulus of Oriented Regioregular Poly(3-hexylthiophene) Films. *Macromolecules* **49**, 327–333 (2016).

22. Chen, H. *et al.* Deformation Mechanism of Poly(3-alkylthiophene) Studied by in Situ X-ray Scattering and Texture Analysis. *Macromolecules* **51**, 8306–8315 (2018).

23. Yasuda, T., Han, L. & Tsutsui, T. Fabrication of Stretch-Oriented Regioregular Poly(3-Hexylthiophene) film and Its Application to Organic Field-Effect Transistors. *J. Photopolym. Sci. Technol.* **22**, 713–717 (2009).

24. Heil, H., Finnberg, T., Von Malm, N., Schmechel, R. & Von Seggern, H. The influence of mechanical rubbing on the field-effect mobility in polyhexylthiophene. *J. Appl. Phys.* **93**, 1636–1641 (2003).

25. Ramachandran, R. *et al.* Persistence length of short-chain branched polyethylene. *Macromolecules* **41**, 9802–9806 (2008).

26. Mena-Osteritz, E. Superstructures of self-organizing thiophenes. *Adv. Mater.* **14**, 609–616 (2002).

27. McCulloch, B. *et al.* Polymer chain shape of poly(3-alkylthiophenes) in solution using small-angle neutron scattering. *Macromolecules* **46**, 1899–1907 (2013).

28. Kuei, B. & Gomez, E. D. Chain conformations and phase behavior of conjugated polymers. *Soft Matter* **13**, 49–67 (2017).

29. Tummala, N. R., Risko, C., Bruner, C., Dauskardt, R. H. & Brédas, J. L. Entanglements in P3HT and their influence on thin-film mechanical properties: Insights from molecular dynamics simulations. *J. Polym. Sci. Part B Polym. Phys.* **53**, 934–942 (2015).

30. Qin, J. & Milner, S. T. Tubes, topology, and polymer entanglement. *Macromolecules* **47**, 6077–6085 (2014).

31. Xie, R., Colby, R. H. & Gomez, E. D. Connecting the Mechanical and Conductive Properties of Conjugated Polymers. *Adv. Electron. Mater.* **4**, 1700356 (2018).

32. Mollinger, S. A., Krajina, B. A., Noriega, R., Salleo, A. & Spakowitz, A. J. Percolation, Tie-Molecules, and the Microstructural Determinants of Charge Transport in Semicrystalline Conjugated Polymers. *ACS Macro Lett.* **4**, 708–712 (2015).

33. Lustiger, A. & Markham, R. L. Importance of tie molecules in preventing polyethylene fracture under long-term loading conditions. *Polymer.* **24**, 1647–1654 (1983).

34. Men, Y., Rieger, J. & Strobl, G. Role of the Entangled Amorphous Network in Tensile Deformation of Semicrystalline Polymers. *Phys. Rev. Lett.* **91**, 095502 (2003).

35. Spano, F. C. & Silva, C. H- and J-Aggregate Behavior in Polymeric Semiconductors. *Annu. Rev. Phys. Chem.* **65**, 477–500 (2014).

36. Lin, L. & Argon, A. S. Structure and plastic deformation of polyethylene. *J. Mater. Sci.* **29**, 294–323 (1994).

37. Butler, M. F. *et al.* A Real-Time Simultaneous Small- and Wide-Angle X-ray Scattering Study of In-Situ Deformation of Isotropic Polyethylene. *Macromolecules* **28**, 6383–6393 (1995).

38. Butler, M. F., Donald, A. M. & Ryan, A. J. Time resolved simultaneous small- and wide-angle X-ray scattering during polyethylene deformation: 1. Cold drawing of ethylene-α-olefin copolymers. *Polymer.* **38**, 5521–5538 (1997).

39. Butler, M. F., Donald, A. M. & Ryan, A. J. Time resolved simultaneous small- and wide-angle X-ray scattering during polyethylene deformation—II. Cold drawing of linear polyethylene. *Polymer.* **39**, 39–52 (1998).

40. Butler, M. F., Donald, A. M. & Ryan, A. J. Time resolved simultaneous small- and wide-angle X-ray scattering during polyethylene deformation 3. Compression of polyethylene. *Polymer.* **39**, 781–792 (1998).

41. López-Barrón, C. R. *et al.* Molecular Alignment in Polyethylene during Cold Drawing Using In-Situ SANS and Raman Spectroscopy. *Macromolecules* **50**, 3627–3636 (2017).

42. Delongchamp, D. M., Kline, R. J., Fischer, D. A., Richter, L. J. & Toney, M. F. Molecular characterization of organic electronic films. *Adv. Mater.* **23**, 319–337 (2011).

43. Richter, L. J., Delongchamp, D. M. & Amassian, A. Morphology Development in Solution-Processed Functional Organic Blend Films: An in Situ Viewpoint. *Chem. Rev.* **117**, 6332–6366 (2017).

44. Potestio, R., Peter, C. & Kremer, K. Computer simulations of soft matter: Linking the scales. *Entropy* **16**, 4199–4245 (2014).

45. Noid, W. G. Perspective: Coarse-grained models for biomolecular systems. *J. Chem. Phys.* **139**, 09B201_1 (2013).

46. Riggleman, R. A., Yoshimoto, K., Douglas, J. F. & de Pablo, J. J. Influence of confinement on the fragility of antiplasticized and pure polymer films. *Phys. Rev. Lett.* **97**, 45502 (2006).

47. Dudowicz, J., Freed, K. F. & Douglas, J. F. Generalized entropy theory of polymer glass formation. *Adv. Chem. Phys.* **137**, 125 (2008).

48. Dudowicz, J., Douglas, J. F. & Freed, K. F. Advances in the generalized entropy theory of glass-formation in polymer melts. *J. Chem. Phys.* **141**, 234903 (2014).

49. Xu, W.-S. S., Douglas, J. F. & Freed, K. F. Influence of cohesive energy on relaxation in a model glass-forming polymer melt. *Macromolecules* **49**, 8355–8370 (2016).

50. Xia, W. *et al.* Energy renormalization for coarse-graining polymers having different segmental structures. *Sci. Adv.* **5**, eaav4683 (2019).

51. Alesadi, A. & Xia, W. Understanding the Role of Cohesive Interaction in Mechanical Behavior of a Glassy Polymer. *Macromolecules* **53**, 2754–2763 (2020).

52. Xia, W. *et al.* Energy renormalization for coarse-graining the dynamics of a model glass-forming liquid. *J. Phys. Chem. B* **122**, 2040–2045 (2018).

53. Lavine, M. S., Waheed, N. & Rutledge, G. C. Molecular dynamics simulation of orientation and crystallization of polyethylene during uniaxial extension. *Polymer.* **44**, 1771–1779 (2003).

54. Zhang, X. *et al.* Molecular packing of high-mobility diketo pyrrolo-pyrrole polymer semiconductors with branched alkyl side chains. *J. Am. Chem. Soc.* **133**, 15073–15084 (2011).

55. Bijleveld, J. C., Verstrijden, R. A. M., Wienk, M. M. & Janssen, R. A. J. Copolymers of diketopyrrolopyrrole and thienothiophene for photovoltaic cells. *J. Mater. Chem.* **21**, 9224–9231 (2011).

56. Zhang, S. *et al.* The Critical Role of Electron-Donating Thiophene Groups on the Mechanical and Thermal Properties of Donor–Acceptor Semiconducting Polymers. *Adv. Electron. Mater.* **5**, 1–11 (2019).

57. Zhang, S. *et al.* Probing the Viscoelastic Property of Pseudo Free-Standing Conjugated Polymeric Thin Films. *Macromol. Rapid Commun.* **39**, (2018).

58. Liu, Y. *et al.* Directly Measuring the Complete Stress-Strain Response of Ultrathin Polymer Films. *Macromolecules* **48**, 6534–6540 (2015).

59. Plimpton, S. Fast parallel algorithms for short-range molecular dynamics. *J. Comput. Phys.* **117**, 1–19 (1995).

60. Payne, M. C., Teter, M. P., Allan, D. C., Arias, T. A. & Joannopoulos, ad J. D. Iterative minimization techniques for ab initio total-energy calculations: molecular dynamics and conjugate gradients. *Rev. Mod. Phys.* **64**, 1045 (1992).

61.   Toepperwein, G. N., Riggleman, R. A. & de Pablo, J. J. Dynamics and deformation response of rod-containing nanocomposites. *Macromolecules* **45**, 543–554 (2012).

62.   Toepperwein, G. N., Schweizer, K. S., Riggleman, R. A. & De Pablo, J. J. Heterogeneous segmental dynamics during creep and constant strain rate deformations of rod-containing polymer nanocomposites. *Macromolecules* **45**, 8467–8481 (2012).

63.   Zhang, S. *et al.* Tacky Elastomers to Enable Tear-Resistant and Autonomous Self-Healing Semiconductor Composites. *Adv. Funct. Mater.* **2000663**, 2000663 (2020).

64.   Van Melick, H. G. H., Govaert, L. E. & Meijer, H. E. H. On the origin of strain hardening in glassy polymers. *Polymer.* **44**, 2493–2502 (2003).

65.   Chen, K. & Schweizer, K. S. Theory of yielding, strain softening, and steady plastic flow in polymer glasses under constant strain rate deformation. *Macromolecules* **44**, 3988–4000 (2011).

66.   Zou, W., Moghadam, S., Hoy, R. S. & Larson, R. G. Multiscale Modeling of Sub-Entanglement-Scale Chain Stretching and Strain Hardening in Deformed Polymeric Glasses. *Macromolecules* **52**, 9248–9260 (2019).

67.   Haward, R. N. Strain Hardening of Thermoplastics. *Macromolecules* **26**, 5860–5869 (1993).

68.   Schrauwen, B. A. G., Janssen, R. P. M., Govaert, L. E. & Meijer, H. E. H. Intrinsic deformation behavior of semicrystalline polymers. *Macromolecules* **37**, 6069–6078 (2004).

69.   Spano, F. C. The Spectral Signatures of Frenkel Polarons in H- and J-Aggregates. *Acc. Chem. Res.* **43**, 429–439 (2010).

70. Balko, J., Lohwasser, R. H., Sommer, M., Thelakkat, M. & Thurn-Albrecht, T. Determination of the Crystallinity of Semicrystalline Poly(3-hexylthiophene) by Means of Wide-Angle X-ray Scattering. *Macromolecules* **46**, 9642–9651 (2013).

71. Kim, J. S. *et al.* Tuning Mechanical and Optoelectrical Properties of Poly(3-hexylthiophene) through Systematic Regioregularity Control. *Macromolecules* **48**, 4339–4346 (2015).

72. Nahid, M. M., Gann, E., Thomsen, L. & McNeill, C. R. NEXAFS spectroscopy of conjugated polymers. *Eur. Polym. J.* **81**, 532–554 (2016).

73. Watts, B., Swaraj, S., Nordlund, D., Lüning, J. & Ade, H. Calibrated NEXAFS spectra of common conjugated polymers. *J. Chem. Phys.* **134**, (2011).

74. Li, Y., Sonar, P., Murphy, L. & Hong, W. High mobility diketopyrrolopyrrole (DPP)-based organic semiconductor materials for organic thin film transistors and photovoltaics. *Energy Environ. Sci.* **6**, 1684–1710 (2013).

75. Li, Z., Liao, Y., Zhang, Y., Zhang, Y. & Xia, W. Microstructure and dynamics of nanocellulose films: Insights into the deformational behavior. *Extrem. Mech. Lett.* **50**, 101519 (2022).

76. Zhao, Y., Liu, J., Li, X., Lu, Y. & Wang, S. Q. How and Why Polymer Glasses Lose Their Ductility Due to Plasticizers. *Macromolecules* **50**, 2024–2032 (2017).

77. Wang, G. J. N. *et al.* Inducing Elasticity through Oligo-Siloxane Crosslinks for Intrinsically Stretchable Semiconducting Polymers. *Adv. Funct. Mater.* **26**, 7254–7262 (2016).

78. Root, S. E., Alkhadra, M. A., Rodriquez, D., Printz, A. D. & Lipomi, D. J. Measuring the Glass Transition Temperature of Conjugated Polymer Films with Ultraviolet-Visible Spectroscopy. *Chem. Mater.* **29**, 2646–2654 (2017).

79.   Mok, J. W. *et al.* Network-Stabilized Bulk Heterojunction Organic Photovoltaics. *Chem. Mater.* **30**, 8314–8321 (2018).

80.   Wang, G.-J. N. *et al.* Tuning the Cross-Linker Crystallinity of a Stretchable Polymer Semiconductor. *Chem. Mater.* **31**, 6465–6475 (2019).

81.   Zheng, Y. *et al.* An Intrinsically Stretchable High-Performance Polymer Semiconductor with Low Crystallinity. *Adv. Funct. Mater.* **29**, 1905340 (2019).

82.   Rodriquez, D. *et al.* Comparison of Methods for Determining the Mechanical Properties of Semiconducting Polymer Films for Stretchable Electronics. *ACS Appl. Mater. Interfaces* **9**, 8855–8862 (2017).

6. FIRST-PRINCIPLES STUDY ON THE ELECTRONIC PROPERTIES OF PDPP-BASED CONJUGATED POLYMER

This chapter focus on computational predictions of the bandgap and absorption spectrum of a one-dimensional periodic model of the diketopyrrolopyrrole (DPP)-based conjugated polymer (CP) (or PDPP3T) as a function of electronic configuration changes due to charge injection. We employ density functional theory (DFT) to explore the ground state and excited state electronic properties and optical properties influenced by charge injection. We utilize the Heyd-Scuseria-Ernzerhof (HSE06) and Perdew-Burke-Ernzerhof (PBE) functionals to predict the bandgap and compute the absorption spectrum.[1]

6.1. Introduction

Over the last decades, the development of donor-acceptor (D-A) type semiconducting CPs [2–6] has prompted considerable progress in organic electronic devices such as organic photovoltaics (OPVs) and field-effect transistors (OFETs).[7–11] It has been shown that CPs exhibit excellent solution processability, structural tenability, good optical and electrical properties, and tunable mechanical compliance compared to their inorganic counterpart silicon.[12–20] Among the CPs, DPP-based polymer (or PDPP3T) has been increasingly utilized in the semiconductor industry due to its high charge mobility,[21] which makes it a promising material candidate in a wide range of applications such as flexible-wearable and biomedical devices. In particular, PDPP3T shows relatively high and balanced charge carrier mobilities for both electrons and holes accompanied by an extended optical absorption near the infrared (IR) region.[22] Despite considerable experimental and computational efforts, the ground state and influence of the injection of charge carriers on the electronic structures of this particular semiconducting polymer is less investigated at the atomistic level.

The charge carrier density and conductivity of semiconducting CPs can be modified via p- or n-type doping (charge injection).[23] Through the doping process (or injection of charge carriers), appropriate impurities with desired electronic properties can be added to donate an electron to the lowest unoccupied molecular orbital (LUMO) for n-type doping or to get rid of an electron from the highest occupied molecular orbital (HOMO) for p-type doping.[24,25] Besides, in the case of injection of the charge carriers, the polymer is not doped via chemicals; instead, the polymer is oxidized or reduced by adding or withdrawing electrons, respectively.[26,27] The applications of semiconductors in various devices can be expanded by tuning the energy of the bandgap to achieve tailored performance.[28] For instance, in photovoltaic cells, a low bandgap increases visible light absorption, carrier mobility, and raises the photogenerated electron-hole pair separation.[29] Therefore, it is crucial to understand the effect of charge injection on the electronic performance of CPs at a fundamental level. For this purpose, DFT approach, one of the most popular computational methods used in modern quantum-chemical modeling materials, can be used to probe their fundamental electronic structures.[30,31] Besides the appropriate accuracy, computational costs of DFT calculations are relatively low compared to traditional methods, such as the exchange only Hartree-Fock (HF) theory.

The Hohenberg-Kohn theorems[32] indicate that the ground state and properties of a many-electron system could be a unique functional of the electron density. In the standard DFT calculations, the nonlocal form of the many-electron Fock exchange energy is computed by integrating a local energy density per electron, described by the local electron density and its derivatives.[33,34] One of the most common usages of these semi-local functionals is the Perdew-Burke-Ernzerhof (PBE) model,[35] which was later improved by incorporating its exchange energy with a fraction of the exact nonlocal Fock exchange energy,[36] producing hybrid functionals such

117

as PBE0[37] upon the generalized gradient approximation (GGA).[38] Among these hybrid functionals, Heyd-Scuseria-Ernzerhof (HSE) screened-Coulomb hybrid density functionals[39–43] take advantage of the short-range HF exchange and avoid computationally expensive long-range exchange. These short-range exchange HSE functionals have shown an appropriate performance to precisely capture the bandgap of semiconducting materials.[33,44,45] For this reason, in the current study, we employed both PBE and HSE hybrid functionals to take advantage of computationally efficient and precise DFT techniques to explore the electronic structure of the current CP model.

Recently, the DFT approaches have been broadly utilized to explore the electronic properties of diverse semiconducting polymers.[46–56] Yang and coworkers[57] showed that the DFT approach can properly estimate the bandgap of the CPs having different molecular structures, where the hybrid functional indicated higher accuracy to predict the energy gap. Another DFT study was done on exploring the bandgap of several CPs,[54] where the calculated theoretical bandgaps show a good agreement with experimental data. In a time-dependent DFT (TD-DFT) study, the simulation successfully predicted the excitation energies and the maximal absorption wavelength of fluorene-based CPs,[58] which were validated by the experimental measurements. DFT and TD-DFT approaches with hybrid functionals were performed to probe the doping process of the polypyrrole,[59] in which the computational results successfully predicted the experimental results on the doping phenomenon. These recent studies have demonstrated that the DFT approach can be utilized as a reliable computational assessment of optoelectronic properties of CPs before experimentally performing a multistep synthesis of these semiconductors. In addition, in the case of polymer materials, the periodicity of the DFT computational model is considerably advantageous for the numerical treatment of polymer structures. Although sampling of the Brillouin zone via an infinite number of k-points is challenging for these periodic DFT systems, it

can provide suitable convergence to experimental data. An explicit account of momentum dispersion is a typical technique for 1D periodic models, such as semiconductor nanowires.[60–63]

In the present study, we first explore the ground state properties of the PDPP3T CP using the DFT approach and a one-dimensional single-chain periodic model. Specifically, the PBE and HSE06 hybrid functionals are employed to predict the bandgap and absorption spectrum of the system. A basic definition of conductivity and a classification of the materials such as conductors, insulators, and semiconductors is based on the value of the bandgap. A small bandgap will allow charge carriers to be promoted from occupied to unoccupied orbitals by thermal excitation or acceleration gained via external voltage AC or DC.[64] We developed our conclusion based on bandgap calculations followed by computing absorption spectrum and charge density distribution. To improve the reliability of our periodic polymer system, the results of bandgaps and absorption spectra are numerically treated via *k*-point sampling over the wide range points of the Brillouin zone. Additionally, the influences of the charge-carrier injection phenomenon, i.e., mimicking n-type and p-type doping, on the conductivity and absorbance of the polymer model are investigated, which shows that doping plays a critical role in the electrical properties of the semiconductors.[65] We further explore the model system's excitation by evaluating the triplet states' electronic properties. Then, the influence of nuclear re-organization (i.e., promotion of the electrons from HOMO to LUMO) on the energy of the bandgap is studied to understand how the bandgap of the new excited state is changed after geometry optimization. The predictive modeling framework established through our study lends valuable insights into the optoelectronic properties of the PDPP3T CPs at both ground and excited states, providing design guidelines for the synthesis and processing of novel organic semiconducting materials to achieve tailored performance.

6.2. Methods

Theoretical methods are logically organized into three sections: ground state DFT, computational details, and ground state observables. Some common statements are included in the description for consistency of notations.

6.2.1. Ground State DFT

In the current study, the atomic model is defined by the initial positions of each ion, $\vec{R}_I$. The electronic structure is calculated through the solution of self-consistent equation of density functional theory (DFT)[66] via Vienna Ab initio Simulation Package (VASP).[67] This approach is developed based on a fictitious one-electron Kohn-Sham (KS) equation. The basic details of the DFT approach and exchange-correlation functionals used in this section are explained in Chapter 2.

6.2.2. Charge Injection

To study the influence of charge-carrier injection on the optoelectronic properties of the current CP model, we consider two additional configurations with different numbers of electrons. The solution of the electronic structure and total energy depends on the number of electrons $N = \int \rho(\vec{r}) \, d\vec{r}$. For the negatively charged system, we perform a DFT model with two more electrons ($N^{\text{Anion}} = N^{\text{Neutral}} + 2$) by setting the control parameter of "NELECT" to 626 in the VASP software to determine the total number of electrons in the system. By default, the total number of valence electrons in the neutral system was $N^{\text{Neutral}} = 624$. In the same manner for the positively charged system ($N^{\text{Cation}} = N^{\text{Neutral}} - 2$), "NELECT" is set to 622 having a hole-injected DFT model with two fewer electrons. For each model, the geometry of the system is fully optimized after the charge injection before any characterization. It should be noted that, In the case of the

manually modified value of the "NELECT" parameter of the charge-injected polymer systems, an

additional neutralizing homogeneous background charge is applied by VASP.[68–70]

6.2.3. Triplet State

In the case triplet state, the total number of electrons can be different for spin α and β,

where $N_\alpha = \int \rho_\alpha(\vec{r}) \, d\vec{r}$ and $N_\beta = \int \rho_\beta(\vec{r}) \, d\vec{r}$ are the number of α-electrons and β-electrons,

respectively. The sum of $N_\alpha + N_\beta$ should be equal to the total number of electrons, and the

difference $\Delta N = N_\alpha - N_\beta$ is often referred as spin polarization parameter in the DFT calculations.

If we set the $\Delta N = 2$, the total spin quantum number is $S = \Delta N/2 = 2/2 = 1$. Then, the

multiplicity of the energy level is defined as $m = 2S + 1 = 2 \times 1 + 1 = 3$ which is required for

a triplet quantum state. In our DFT model, we perform triplet spin state calculations by setting the

parameters of "ISPIN $= 2$", and "$NUPDOWN = \Delta N = 2$" in the VASP program, based on the

spin state of the lowest energy of optimized geometry.

6.2.4. Manual Occupancy

Promoting two electrons from HOMO to LUMO, is related to change the population

pattern for KS orbitals, maintaining close shell and singlet spin configuration. To mimic the

vertical excitation, two electrons are promoted from HOMO to LUMO, where the contribution of

each KS orbital to the total density of the system is defined via occupation numbers $\rho(\vec{r}) =$

$\sum_i f_i \varphi_i^{KS^*}(\vec{r}) \varphi_j^{KS}(\vec{r})$. This initial excitation occurs between orbitals a and b described by the

density matrix $\rho_{ij}^{(a,b)} = \delta_{ij}(f_i - \delta_{ia} - \delta_{ib})$ where δ is the Kronecker delta symbol and $f_i =$

$\begin{cases} 1 & i \leq HOMO \\ 0 & i \geq LUMO \end{cases}$. To perform this, we define the manual occupancy by setting the "FERWE"

parameter in the VASP program to artificially set up the non-Aufbau occupancies for examining

excited states beyond the lowest-energy state of symmetry occupancy. After the promotion of the electrons, the geometry of the polymer system is optimized before any property calculation.

6.2.5. Periodic Model

The atomistic model of the CP is shown in Figure 6.1. The periodic model consists of the monomers which are connected upon approximately 180° rotation relative to each other to make adjacent thiophene groups more stable and preserve the linear structure of the backbone, while the same-oriented successive monomers exhibit curvature of the backbone within the conjugated plane.[71] The chemical structure is generated by the Materials Studio package pre-optimized via force field calculations. The backbone of the periodic model is stretched in the z-direction where the cell size in that direction is calculated to keep the system at the minimum total energy state. The side groups of C_6H_{13} and C_8H_{17} are grafted to both sides of the monomer. Figure 6.1B shows the geometrically optimized structure of the polymer model.
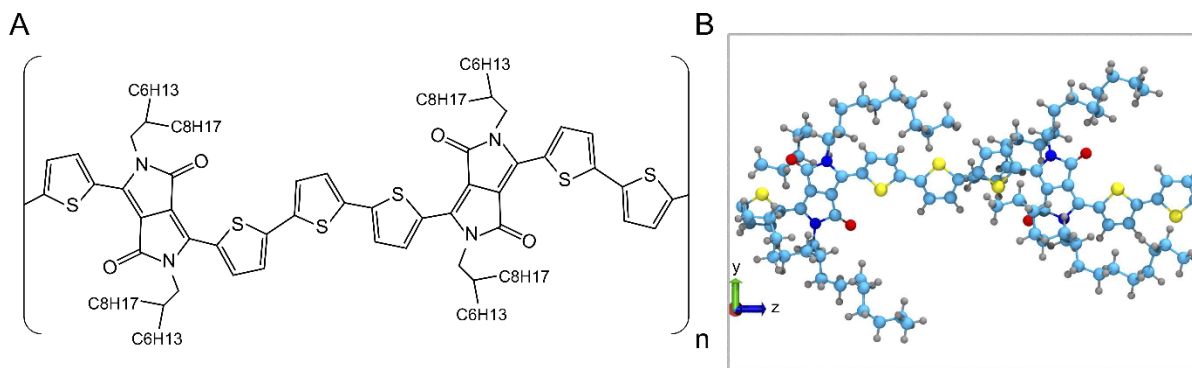
Figure 6.1. (A) Schematic chemical structure of the PDPP conjugated polymer model employed in the simulations. (B) Geometry of optimized structure (ground state) of the polymer model aligned in the y-z plane. Cyan, blue, gray, yellow, and red spheres represent C, N, H, S, and O atoms respectively.

6.3. Results

An illustrative schema of the current study is presented in Figure 6.2. First, as it is shown in Figure 6.2A, the energy gap of the current semiconducting polymer model is explored, and the results are compared to the experimental data. Next, the influence of charge-carrier injection,

mimicking the doping phenomenon, on the polymer model's fundamental electronic and optical properties is investigated. Doping is the process of adding impurities to the semiconductors to modify their electronic structure. The smaller energy gap between the conduction band (CB) and valence band (VB) facilitates moving electrons from HOMO to LUMO under excitation, increasing the electrical conductivity in semiconductors. Such a phenomenon is directly relevant to photovoltaic performance of these semiconducting materials. Through the injection of charge-carrier, a new energy level appears between VB and CB, which reduces the bandgap and increases the conductivity as shown in Figure 6.2B and C. Here, we explore the influence of charge-carrier-injection on the electronic properties of PDPP3T CP to provide useful insights into the optical properties at the excited state, allowing for tunable conductivity of these polymers. Additionally, the triplet state of the polymer model is probed to gain insights into the excitation of these semiconductors (Figure 6.2D). Next, we explore the response of geometry to electronic excitation, i.e., nuclear reorganization, induced by promoting electrons from HOMO to LUMO, and its influence on the bandgap of polymer model (Figure 6.2E). Finally, for further investigation of the ground state and absorption spectrum bandgap, k-points sampling (Figure 6.2F) is carried out over the Brillouin zone to sample the reciprocal space adequately.

123
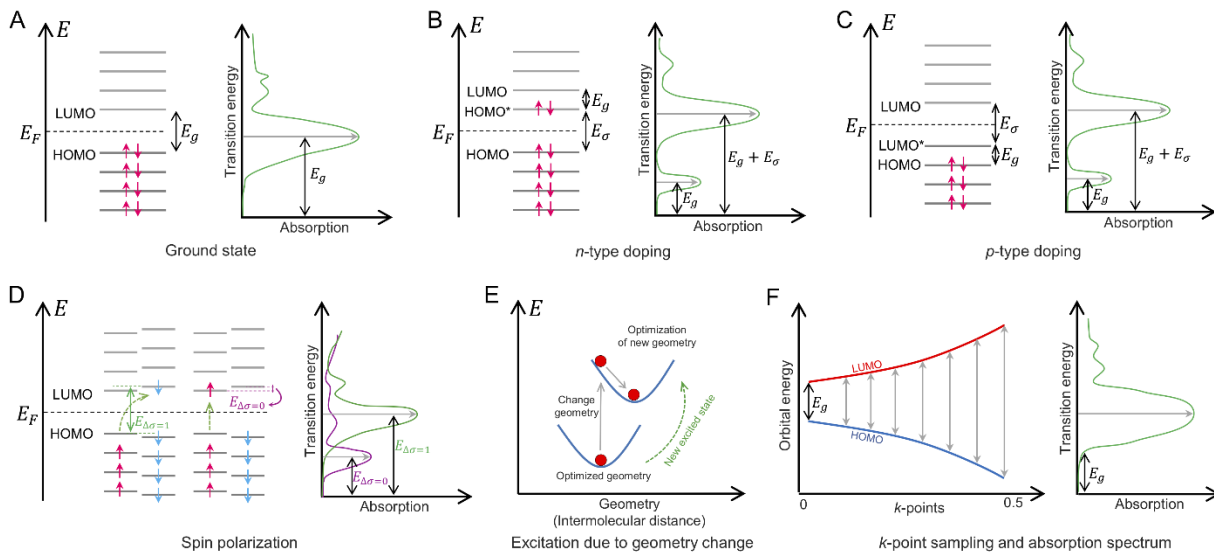
Figure 6.2. (A) A schematic of the ground state energy band and absorption spectra. (B) The energy band and absorption spectra schema due to n-type doping (electron donors). (C) The energy band and absorption spectra schema due to p-type doping (electron acceptors). (D) Schema of spin polarization process and corresponding absorption spectra. (E) A portrayal of geometry changes due to excitation and optimized geometry after the excitation. (F) A schematic representation of band structure with k-points sampling and corresponding absorption spectrum. Here, E_g, E_F, E_σ, and $E_{\Delta\sigma}$ represents bandgap energy, Fermi energy, and band energy gap of the excited state, respectively.

The density of states (DOS) and the band structures of the ground and excited states are reported in Figure 6.3. First, to study the ground state band structure and predict the bandgap, PBE functional is utilized to minimize the system's total energy. The DOS of near-gap orbitals are exhibited in Figure 6.3A, where a bandgap of 0.89 eV is predicted, smaller than the observed experimental bandgap of 1.3 eV obtained via optical absorption.[22] This implies that PBE functional underestimates the bandgap of the current polymer model. Next, for a more accurate prediction of the bandgap, hybrid HSE06 functional is tested for our calculations, which provides a better approximation of the bandgap compared to the experimental value. Using HSE06 functional, the calculated bandgap of 1.2 eV is predicted, as shown in Figure 6.3B, which agrees reasonably well with the experimental value, highlighting the capabilities of DFT calculations to predict the energy

124

gap of semiconductors. In the case of low-bandgap systems, electrons can be quickly promoted from the valence band to the conduction band, and the current can flow. Therefore, the bandgap is a major factor in determining semiconductors' electrical conductivity. The results of the injection of the negative and positive charge carriers on the energy gap are reported in Figure 6.3C and D. The electronic structure of injected polymer model is expected to imitate the behavior of doped semiconductors. As Figure 6.3C indicates, after the injection of two electrons into the system, the original LUMO orbital is populated via these two injected electrons and ended in a much smaller energy gap of 0.34 eV. This decrease of the bandgap indicates that injecting the electrons (n-type doping) can considerably improve the conductivity of the current model, which is consistent with the recent experimental study of the similar CP system.[72] Negative and positive injections here could correspond to chemical reduction and chemical oxidation in experiments, respectively.
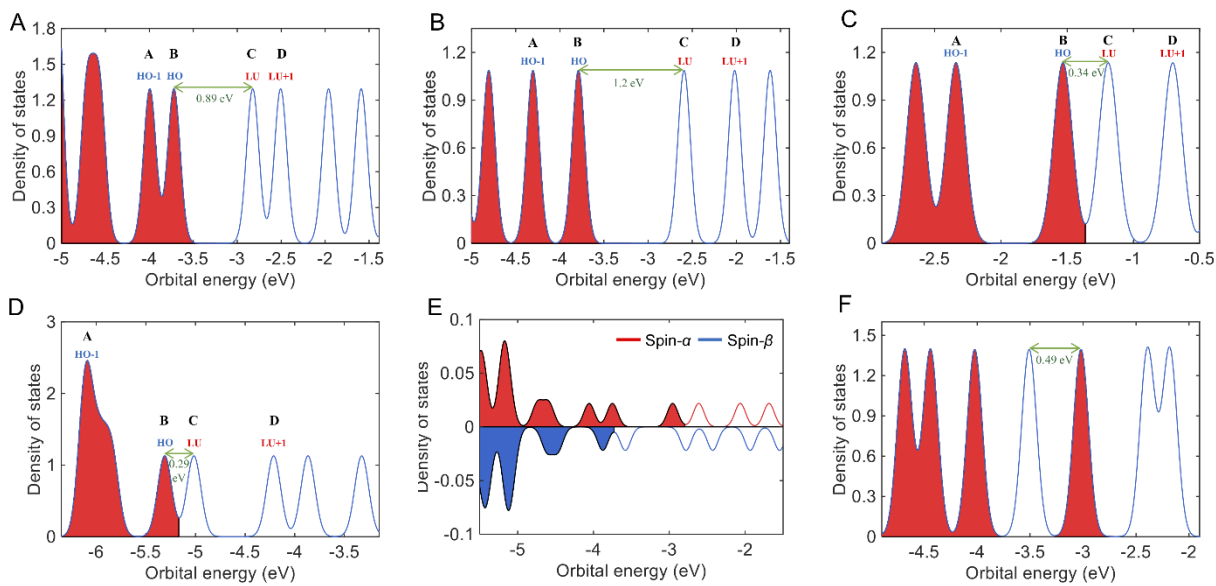
Figure 6.3. (A) DOS of the polymer model calculated by DFT via PBE exchange-correlation functional. Red shaded regions represent the occupied orbitals, and unshaded regions indicate unoccupied orbitals. Four frontier orbitals near the bandgap are labeled. (B) DOS of polymer model calculated by DFT via HSE06 hybrid functional in which bandgap is larger. (C) DOS of polymer model calculated by DFT for the injected electron doping of the conjugated polymer model (n-doping, negative polaron). Red shaded regions represent the occupied orbitals and unshaded regions indicate unoccupied orbitals. Four frontier orbitals near the bandgap are labeled. (D) DOS of polymer model calculated by DFT for the injected hole doping (p-doping, positive polaron) of the conjugated polymer model. (E) Triplet state DOS of the CP model. The red-shaded regions indicate the occupied orbitals with spin +1/2, and blue-shaded regions correspond to spin component -1/2. (F) DOS near the band edges of the CP model when an electron was promoted from HOMO to LUMO, mimicking the excited state.

Similarly, for the injection of positive charge carriers, mimicking p-type doping, we explore the influence of forming p-type regions on the energy gap of the current semiconducting CP. Figure 6.3D shows that injecting holes into the system considerably decreases the bandgap to 0.29 eV. Indeed, withdrawing two electrons from the system forms a p-type region and evacuates two electrons of HOMO that converts it into a new LUMO[*,] which leads to new energy levels and a smaller bandgap appearing. In similar experimental studies on PDPP3T polymer, it was found that p-type doping can significantly improve the conductivity of the system.[73,74]

Then, the triplet state results are presented in Figure 6.3E, where the effects for both spin up and down directions point out the bandgap of 0.35 eV and 0.29 eV, respectively, implying that the bandgap is decreased in the triplet state. To further explore the excited state, the influence of nuclear reorganization on the electronic properties is investigated as shown in Figure 6.3F, where two electrons are promoted from HOMO to LUMO. The optimized geometry under the new condition shows smaller bandgaps of 0.49 eV, which represents higher conductivity for this excited system.

The DOS of the positively charged, uncharged, and negatively charged polymer model is shown in Figure 6.4, calculated via PBE functional. In this figure, all DOS plots are shown for the same energy range to indicate how orbitals are occupied and how the energy level is changed over the charge injection. As we go across the progression of the systems with different charges, a larger number of orbitals get occupied. For the positively charged system, Figure 6.4A, 2 electrons are removed from the system, and HOMO appears on orbital 311. For the uncharged system shown in Figure 6.4B, HOMO resides on orbital 312. Eventually, for the negatively charged system, Figure 6.4C, 2 electrons are injected into the system and occupy the orbital 313 as HOMO. Interestingly, the energy of the orbitals changes as the system gets charged, which is attributed to electron-electron interaction. As more orbitals get occupied, Fermi energy shifts from lower to higher values. Since Principles of the Hohenberg-Kohn theorems of the DFT approach signify and prove the importance of the total energy of the electrons, it would be beneficial to review the total energy of these three systems. For the uncharged system, the total energy of -1519.71 eV is predicted. However, the positively charged system exhibit total energy of -1510.99 eV, as the model misses electron-electron interactions compared to the uncharged system. The negatively charged system reaches the total energy of -1524.054 eV since the model benefits from two more electrons.
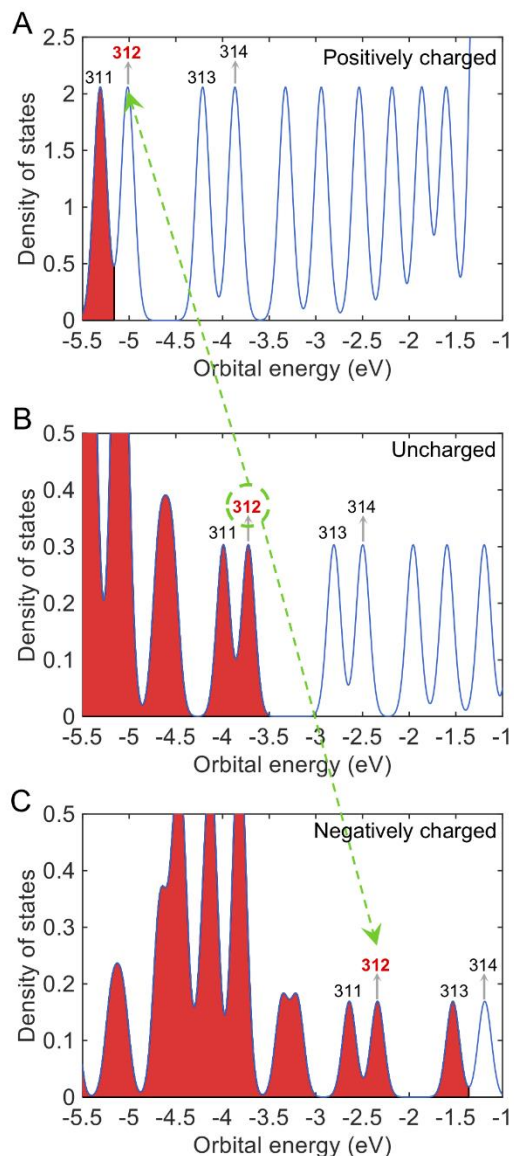
Figure 6.4. DOS of the (A) positively charged (B) uncharged and (C) negatively charged polymer models calculated via PBE functional. All three DOS are plotted for the same energy level to show how near-gap orbitals are populated and how the energy level is shifted upon the charge injection. Red shaded regions represent the occupied orbitals. The orbital number of four frontier orbitals near the bandgap is shown.

Figure 6.5 shows the *k*-points resolved band structure with 16 *k*-points for both PBE and HSE06 functionals in the DFT calculations. It appears that our PDPP-based CP model is a direct bandgap semiconductor. In the case of PBE functionals (Figure 6.5A), a direct bandgap of 0.79

eV is predicted, which underestimates the observed experimental values (as mentioned above). However, for HSE06 functional (Figure 6.5B), a direct gap of 1.2 eV is found to yield a good approximation compared to the experimental values.
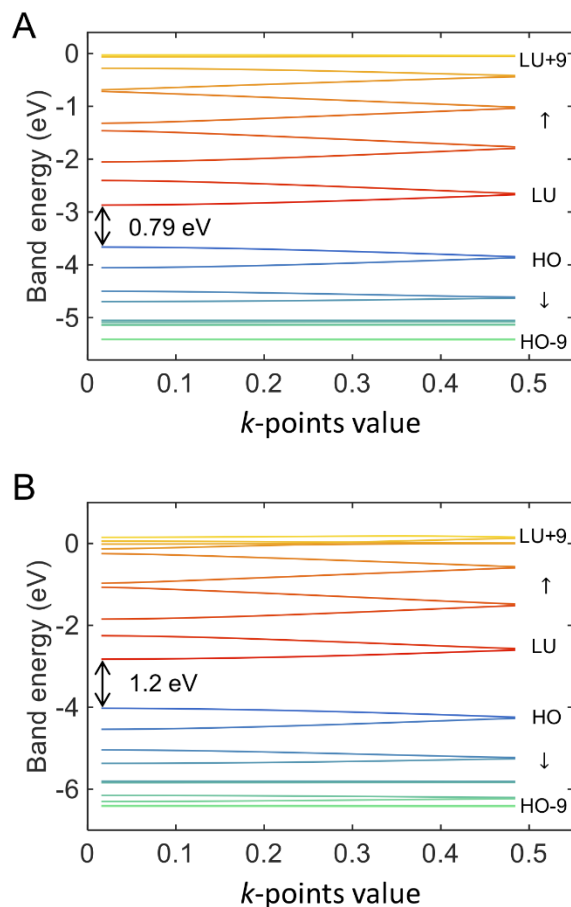
Figure 6.5. (A) The band structure of reference CP model calculated using PBE functional. A direct bandgap is predicted. (B) The band structure of the same model was calculated through HSE06 functional. In both cases, the x-axis represents k-point sampling.

The calculated absolute value squared of the four frontier KS orbitals are shown in Figure 6.6, calculated via HSE06 functional. A qualitative assessment of conductivity of a material is affected by two contributions: (I) charge mobility/localization/delocalization and (II) availability of charge carriers in a given band, related to the HOMO/LUMO energy gap. In current study, both contributions are discussed with more focus on the contribution (B). For the orbital HOMO-1 in

Figure 6.6A, maximal absolute value squared/charge density appears on the oxidized pyridine group and this localized orbital is not conducive. Figure 6.6B shows calculations for the HOMO, where the maximum absolute value squared/charge density resides on the oxidized pyridine group. However, there is substantial charge density on each thiophene group, and this delocalized nature of that orbital contributes to the polymer's conductive behavior. For the LUMO and LUMO+1 orbitals in Figure 6.6C and D, the maximal value shows up on the oxygen in the pyridine group, accompanied by a substantial absolute value squared/charge density on each thiophene and pyridine group. This delocalized nature of these orbitals is expected to contribute to the conductive behavior of the polymer.
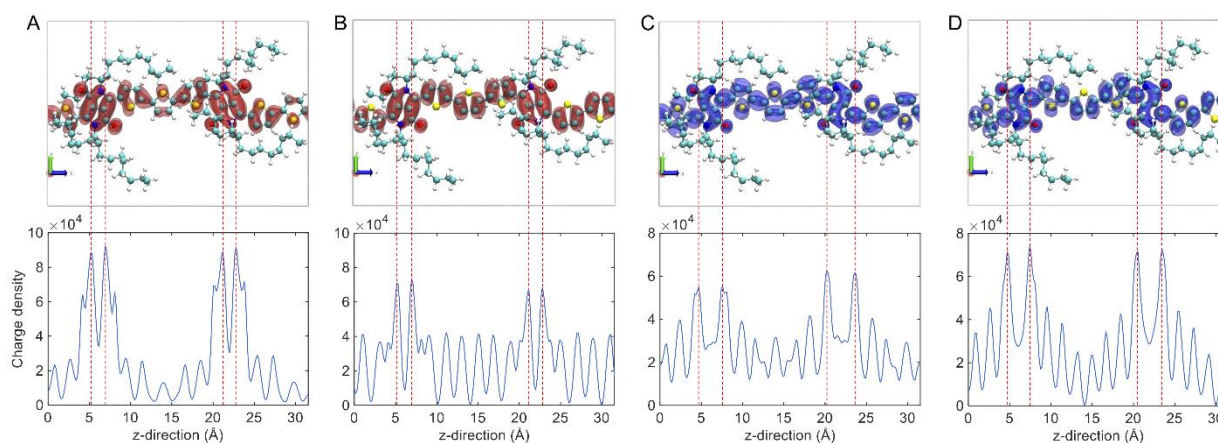
Figure 6.6. The charge density of the frontier molecular orbitals at the ground state via HSE06 hybrid functionals: (A) The orbital of 311, HOMO-1, (B) The orbital of 312, HOMO, (C) The orbital of 313, LUMO, and (D) The orbital of 314, LUMO+1. Shaded areas indicate the electron density. To plot the isosurfaces, an isovalue of 0.002 is used.

The absorption spectra of the current polymer model are reported in Figure 6.7. The fundamental absorption presented here shows the transition of an electron from the ground state to an excited electronic state. The absorption spectrum describes the probability of excitation at certain transition energy, which the re-population of orbitals is used for approximate excited state optimization. Here, we calculate the polymer model's oscillator strength and transition energies

for both ground and excited states. For PBE functional, as shown in Figure 6.7A, the first peak appears on 0.8 eV corresponding to the transition energy from HOMO to LUMO. Other absorption spectrum peaks for electron promotions from the other frontier orbitals are also labeled. In the same manner for the HSE06 hybrid functional, Figure 6.7B, the first peak equivalent to the smallest transition energy shows up on 1.2 eV, which is equal to the calculated bandgap between HOMO and LUMO for this functional. As discussed in Figure 6.7, the k-point sampling has been done with 16 k-points, and the averaged absorption spectra of both PBE and HSE06 functionals are reported in Figure 6.7C and D, respectively. In the case of k-point sampling using PBE functional, as shown in Figure 6.7C, the first peak of the absorption spectrum appears on transition energy 0.82 eV, which is close to the predicted direct bandgap value 0.79 eV (reported in Figure 6.7A). On the other hand, for k-point sampling using HSE06 functional, the minimum transition energy is around 1.32 eV. The absorption spectra of the excited state show the minimum transition energy 0.34 eV and 0.29 eV for n-type and p-type doping, respectively, which is found to be very close to their predicted bandgaps in Figure 6.3.
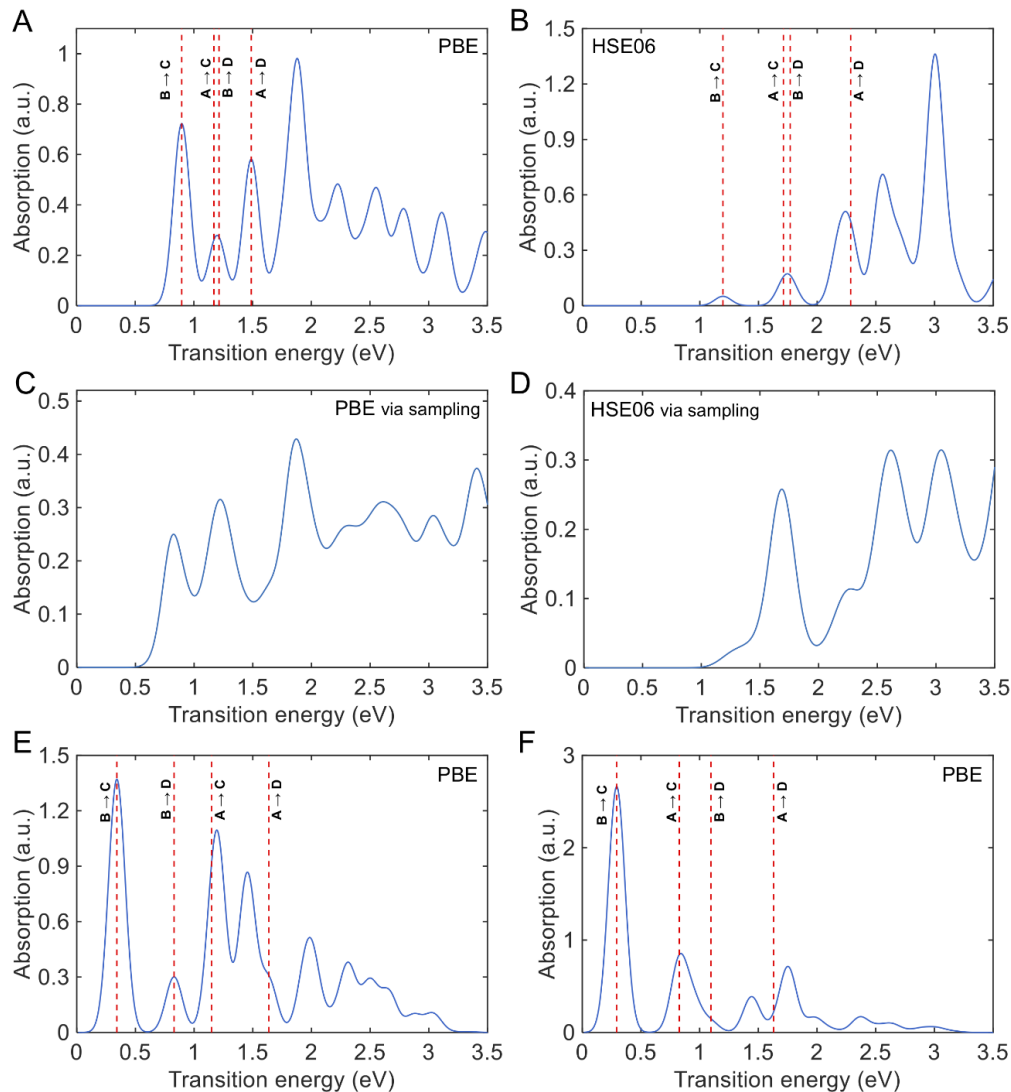
Figure 6.7. (A) Absorption spectra of CP model using PBE exchange-correlation functional. Dashed lines show the transition energy between selected orbitals where the lowest energy is predicted for the transition from HOMO to LUMO (B to C). Four frontier orbitals near the bandgap are labeled. (B) Absorption spectra vs. transition energy of the CP model calculated using the HSE06 functional. (D) Absorption spectra vs. transition energy graph for the reference model using PBE functional with *k*-point sampling of 16 k-points. (D) Absorption spectra vs. transition energy graph for the same model using HSE06 functional with k-point sampling of 16 k-points. (E) Absorption spectra vs. transition energy graph of the CP model in case of injected electron doping (n-type doping, negative polaron). Dashed lines show the transition energy between selected orbitals where the lowest energy is predicted for the transition from HOMO to LUMO (B to C). (F) Absorption spectra vs. transition energy graph for the CP model in case of injected hole doping (p-type doping, positive polaron).

The corresponding wavelength of fundamental absorption of semiconductors usually occurs in the visible and near IR spectral range. We evaluate the absorption spectra in terms of wavelength, Figure 6.8, to explore the ground state and the influence of excitation on its optical absorption and to compare our results to the available experimental findings. Figure 6.8A shows the absorption spectrum for PBE functional, in which maximum absorbance (λ_p) appears around 1400 nm, not surprising, far away from the reported experimental value of $\lambda_p \approx 800$ nm.[75] Furthermore, the absorption spectra using HSE06 functional as shown in Figure 6.8B, provide an improved approximation at $\lambda_p = 1036$ nm compared to the value from PBE functional; however, a considerable divergence to the experimental data is still remained. To improve the results, the averaged absorption spectrum over k-point sampling is calculated, resulting in a better approximation of λ_p, which alleviates the challenge of discrepancy between the computational results and experimental data. In the case of PBE functional (Figure 6.8C), we do not observe any improvement in the sampling results, comparing to the results at the gamma point. However, the sampling of HSE06 functional as shown in Figure 6.8D provides a much better approximation of $\lambda_p \approx 737$ nm, which is found to be in good agreement with the experimental data (marked by the black dashed line).

Moreover, Figure 6.8E and F show the wavelength of the absorption spectrum largely red-shifted for the injected charges, analogous to n-type and p-type doping, of the polymer model. The results imply that the wavelengths of doped PDPP3T absorption spectra will no longer remain in the visible/near IR spectral range and shift into the IR region. A similar trend for this polymer system was observed in experimental studies,[73,74] where the doped PDPP3T polymer exhibited a strong absorption near the IR area.
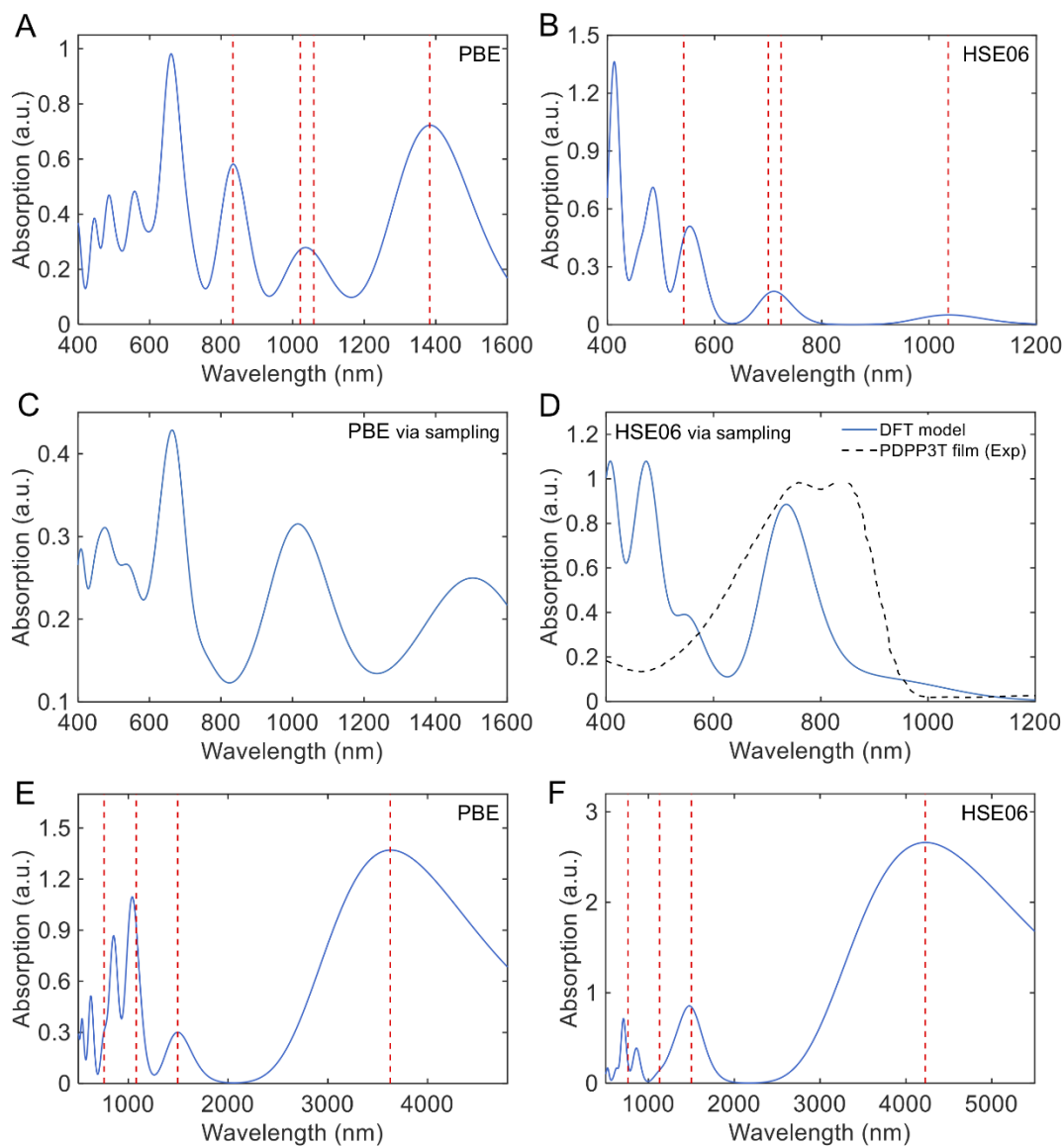
Figure 6.8. (A) Absorption spectra vs. wavelength graph of the CP model via PBE exchange-correlation functional. (B) Absorption spectra vs. wavelength plot for the CP model using HSE06 functional. (C) Absorption spectra vs. wavelength graph of the reference model using PBE functional with 16 k-points. (D) Absorption spectra vs. wavelength graph of the same model using the HSE06 functional with 16 k-points. The experimental results of the current polymer are indicated in black dashed line.[75] (E) Absorption spectra vs. wavelength of the CP model in case of injected electron doping (n-type, negative polaron). (F) Absorption spectra vs. wavelength graph of the CP model in case of injected hole doping (p-type, positive polaron).

6.4. Discussion

At a certain system size, the bandgap experiences saturation and becomes independent of further increase of the size of the model. In the case of the periodic model, the motion of electrons is restricted in the direction normal/orthogonal to the growth directions and the carriers (electrons) are free to move only in the growth directions (in direction of polymer backbone).

Trends in bandgap as function of method. Typically, GGA based on PBE exchange-correlation functional underestimates the bandgap. The underestimated bandgap can be improved by calculating electronic structure using a hybrid functional. In our study, band structure calculation with PBE functional underestimates the bandgap of PDPP3T polymer by around 0.41 eV. However, HSE06 functionals provide a precise prediction of 1.2 eV, reasonably close to the experimentally measured value of 1.3 eV.

Trends in bandgap as function of physical conditions. In the case of bandgap calculations, k-points sampling does not improve the results predicted from both functionals, where the results of the bandgap values for certain k-points are found slightly smaller than those for gamma point only calculations. Injection of additional electrons and holes (mimicking n-type and p-type doping) largely reduces the bandgap. This further implies that the increase of the concentration of injected charge carriers or dopants improves charge carrier mobility in the injected PDPP3T resulting in higher conductivities, which have been experimentally explored before. Generally, due to the charge injection, the polymer is considered to be oxidized or reduced, which means electrons are added to the π^* band or removed from the π band, in an analogous way as doping phenomenon; nevertheless, the polymer is not directly doped in the sense of chemical or electrochemical doping.[26,27] Besides, the injected PDPP3T polymer with a lower bandgap exhibits a shift of absorption spectrum into the IR area, resulting in a colorless semiconductor after

doping. This potentially makes them appropriate material candidates for the development of transparent electronic devices. For the absorption spectrum calculated with HSE06 hybrid functionals, k-points sampling substantially improve the results, where computed λ_p was found close to reported experimental values. Additionally, nuclear reorganization by promoting the electrons from HOMO to LUMO and also triplet state considerably reduces the bandgap of the polymer model.

Our results provide computational design guidance for the development of high-performance D-A semiconducting polymers. The bandgap results for HSE06 functional and k-point sampling of the Brillouin zone demonstrate that the current DFT approach can predict the bandgap of CPs and compute the absorption spectrum to a good approximation. Furthermore, the charge injection modeling mimicking the doping process is a crucial driving factor for obtaining low bandgap and high-mobility PDPP3T polymers.

6.5. Conclusions

In the present study, the fundamental electronic and optical properties of the PDPP3T CP are studied via the DFT-based computational approach. The energy gap and absorption spectrum of the ground and excited states are carried out by PBE and HSE06 hybrid functionals. HSE06 functional yields a greatly improved prediction of a bandgap of 1.2 eV, which is largely consistent with the experimentally reported value of 1.3 eV for the PDPP3T polymer model. For HSE06 DFT results, an explicit treatment of momentum dispersion provides appropriate agreement of the computed absorption spectrum with the experimental data. Additionally, we study the analogy between charge injection and n-type and p-type doping on the optoelectronic properties of the semiconducting polymer model. We observe that the injection of holes and electrons into the polymer can both effectively reduce the bandgap and shift the absorption spectrum into the IR

region, leading to a more conductive behavior, in good agreement with experimental observations. This observation is further confirmed by evaluations of nuclear reorganization and triplet state. Our results demonstrate the efficacy of introducing charge carriers into the PDPP3T as a computational design strategy to tune the optical and electronic properties and achieve a lower bandgap, which are useful in developing high-performance organic photovoltaic and optoelectronic devices.

6.6. References

1. Alesadi, A., Fatima, F., Xia, W. & Kilin, D. First-Principles Study on the Electronic Properties of PDPP-Based Conjugated Polymer via Density Functional Theory. *J. Phys. Chem. B* **125**, 8953–8964 (2021).

2. Mei, J., Diao, Y., Appleton, A. L., Fang, L. & Bao, Z. Integrated materials design of organic semiconductors for field-effect transistors. *J. Am. Chem. Soc.* **135**, 6724–6746 (2013).

3. Sirringhaus, H. 25th anniversary article: Organic field-effect transistors: The path beyond amorphous silicon. *Adv. Mater.* **26**, 1319–1335 (2014).

4. Xue, X. *et al.* Oriented Liquid Crystalline Polymer Semiconductor Films with Large Ordered Domains. *ACS Appl. Mater. Interfaces* **7**, 26726–26734 (2015).

5. Gu, X., Shaw, L., Gu, K., Toney, M. F. & Bao, Z. The meniscus-guided deposition of semiconducting polymers. *Nat. Commun.* **9**, 534 (2018).

6. Sirringhaus, H., Tessler, N. & Friend, R. H. Integrated optoelectronic devices based on conjugated polymers. *Science (80-.).* **280**, 1741–1744 (1998).

7. Yamashita, Y. *et al.* Mobility Exceeding 10 cm2/(V·s) in Donor-Acceptor Polymer Transistors with Band-like Charge Transport. *Chem. Mater.* **28**, 420–424 (2016).

8. Kim, G. *et al.* A thienoisoindigo-naphthalene polymer with ultrahigh mobility of 14.4 cm 2 /V·s that substantially exceeds benchmark values for amorphous silicon semiconductors. *J. Am. Chem. Soc.* **136**, 9477–9483 (2014).

9. Luo, C. *et al.* General strategy for self-assembly of highly oriented nanocrystalline semiconducting polymers with high mobility. *Nano Lett.* **14**, 2764–2771 (2014).

10. Meng, L. *et al.* Organic and solution-processed tandem solar cells with 17.3% efficiency. *Science (80-.).* **361**, 1094–1098 (2018).

11.   Zhugayevych, A. & Tretiak, S. Theoretical description of structural and electronic properties of organic photovoltaic materials. *Annu. Rev. Phys. Chem.* **66**, 305–330 (2015).

12.   Root, S. E., Savagatrup, S., Printz, A. D., Rodriquez, D. & Lipomi, D. J. Mechanical Properties of Organic Semiconductors for Stretchable, Highly Flexible, and Mechanically Robust Electronics. *Chem. Rev.* **117**, 6467–6499 (2017).

13.   Someya, T., Bao, Z. & Malliaras, G. G. The rise of plastic bioelectronics. *Nature* **540**, 379–385 (2016).

14.   Lipomi, D. J. & Bao, Z. Stretchable and ultraflexible organic electronics. *MRS Bull.* **42**, 93–97 (2017).

15.   Bao, Z. & Chen, X. Flexible and Stretchable Devices. *Adv. Mater.* **28**, 4177–4179 (2016).

16.   Oh, J. Y. & Bao, Z. Second Skin Enabled by Advanced Electronics. *Adv. Sci.* **6**, 1900186 (2019).

17.   Lipomi, D. J., Tee, B. C. K., Vosgueritchian, M. & Bao, Z. Stretchable organic solar cells. *Adv. Mater.* **23**, 1771–1775 (2011).

18.   Chortos, A., Liu, J. & Bao, Z. Pursuing prosthetic electronic skin. *Nat. Mater.* **15**, 937–950 (2016).

19.   Zhang, S. *et al.* Toward the Prediction and Control of Glass Transition Temperature for Donor–Acceptor Polymers. *Adv. Funct. Mater.* **2002221**, 2002221 (2020).

20.   Zhang, S. *et al.* Molecular Origin of Strain-Induced Chain Alignment in PDPP-Based Semiconducting Polymeric Thin Films. *Adv. Funct. Mater.* **31**, 2100161 (2021).

21.   Chen, H. *et al.* Highly π-Extended Copolymers with Diketopyrrolopyrrole Moieties for High-Performance Field-Effect Transistors. *Adv. Mater.* **24**, 4618–4622 (2012).

22.   Bijleveld, J. C. *et al.* Poly (diketopyrrolopyrrole− terthiophene) for Ambipolar Logic and Photovoltaics. *J. Am. Chem. Soc.* **131**, 16616–16617 (2009).

23.   Yim, K. *et al.* Controlling Electrical Properties of Conjugated Polymers via a Solution-Based p-Type Doping. *Adv. Mater.* **20**, 3319–3324 (2008).

24.   Salzmann, I., Heimel, G., Oehzelt, M., Winkler, S. & Koch, N. Molecular electrical doping of organic semiconductors: fundamental mechanisms and emerging dopant design rules. *Acc. Chem. Res.* **49**, 370–378 (2016).

25.   Jayasundara, W. S. R. & Schreckenbach, G. Theoretical Study of p-and n-Doping of Polythiophene-and Polypyrrole-Based Conjugated Polymers. *J. Phys. Chem. C* **124**, 17528–17537 (2020).

26.   Heeger, A. J. Semiconducting and metallic polymers: The fourth generation of polymeric materials. *Curr. Appl. Phys.* **1**, 247–267 (2001).

27.   Heeger, A. J., MacDiarmid, A. G. & Shirakawa, H. The Nobel Prize in chemistry, 2000: conductive polymers. *Stock. Sweden R. Swedish Acad. Sci.* 1–16 (2000).

28.   Kim, B. *et al.* Energy level modulation of HOMO, LUMO, and band-gap in conjugated polymers for organic photovoltaic applications. *Adv. Funct. Mater.* **23**, 439–445 (2013).

29.   Ma, X. *et al.* A strategy of enhancing the photoactivity of g-C3N4 via doping of nonmetal elements: a first-principles study. *J. Phys. Chem. C* **116**, 23485–23493 (2012).

30.   Medvedev, M. G., Bushmarinov, I. S., Sun, J., Perdew, J. P. & Lyssenko, K. A. Density functional theory is straying from the path toward the exact functional. *Science (80-.).* **355**, 49–52 (2017).

31.   Jones, R. O. Density functional theory: Its origins, rise to prominence, and future. *Rev. Mod. Phys.* **87**, 897 (2015).

32. Hohenberg, P. P hys. rev. 1964, 136, b864–b871; b) w. kohn, lj sham. *Phys. Rev* **140**, A1133–A1138 (1965).

33. Moussa, J. E., Schultz, P. A. & Chelikowsky, J. R. Analysis of the Heyd-Scuseria-Ernzerhof density functional parameter space. *J. Chem. Phys.* **136**, 204117 (2012).

34. Sholl, D. & Steckel, J. A. *Density functional theory: a practical introduction*. (John Wiley & Sons, 2011).

35. Perdew, J. P., Burke, K. & Ernzerhof, M. Generalized gradient approximation made simple. *Phys. Rev. Lett.* **77**, 3865 (1996).

36. Becke, A. D. Becke's three parameter hybrid method using the LYP correlation functional. *J. Chem. Phys* **98**, 5648–5652 (1993).

37. Adamo, C. & Barone, V. Toward reliable density functional methods without adjustable parameters: The PBE0 model. *J. Chem. Phys.* **110**, 6158–6170 (1999).

38. Perdew, J. P. Accurate density functional for the energy: Real-space cutoff of the gradient expansion for the exchange hole. *Phys. Rev. Lett.* **55**, 1665 (1985).

39. Heyd, J., Scuseria, G. E. & Ernzerhof, M. No Title. *J. Chem. Phys.* **118**, 8207 (2003).

40. Heyd, J., Scuseria, G. E. & Ernzerhof, M. No Title. *J. Chem. Phys.* **124**, 219906 (2006).

41. Heyd, J. & Scuseria, G. E. No Title. *J. Chem. Phys.* **120**, 7274 (2004).

42. Heyd, J. & Scuseria, G. E. No Title. *J. Chem. Phys.* **121**, 1187 (2004).

43. Heyd, J., Peralta, J. E., Scuseria, G. E. & Martin, R. L. No Title. *J. Chem. Phys.* **123**, 174101 (2005).

44. Heyd, J., Peralta, J. E., Scuseria, G. E. & Martin, R. L. Energy band gaps and lattice parameters evaluated with the Heyd-Scuseria-Ernzerhof screened hybrid functional. *J. Chem. Phys.* **123**, 174101 (2005).

45.   Paier, J. *et al.* Screened hybrid density functionals applied to solids. *J. Chem. Phys.* **124**, 154709 (2006).

46.   Siham, L., Bouchra, M., Latfa, L. & Ahmed, J. Electronic and photoelectronic properties of N-(5-indazolyl)-arylsulfonamides molecules: DFT/TD-DFT study. in *2020 IEEE 6th International Conference on Optimization and Applications (ICOA)* 1–6 (IEEE, 2020).

47.   Vu, Q.-T. *et al.* DFT Prediction of Factors Affecting the Structural Characteristics, the Transition Temperature and the Electronic Density of Some New Conjugated Polymers. *Polymers (Basel).* **12**, 1207 (2020).

48.   Kilina, S., Kilin, D. & Tretiak, S. Light-Driven and Phonon-Assisted Dynamics in Organic and Semiconductor Nanostructures. *Chem. Rev.* **115**, 5929–5978 (2015).

49.   Vu, K. B. *et al.* Conjugated polymers: A systematic investigation of their electronic and geometric properties using density functional theory and semi-empirical methods. *Synth. Met.* **246**, 128–136 (2018).

50.   Sun, H. & Autschbach, J. Electronic Energy Gaps for π-Conjugated Oligomers and Polymers Calculated with Density Functional Theory. *J. Chem. Theory Comput.* **10**, 1035–1047 (2014).

51.   Mabrouk, A., Azazi, A. & Alimi, K. Molecular structure–property engineering of low-band-gap copolymers, based on fluorene, for efficient bulk heterojunction solar cells: A density functional theory study. *Polym. Eng. Sci.* **53**, 1040–1052 (2013).

52.   Ferretti, A. *et al.* Ab initio complex band structure of conjugated polymers: Effects of hydrid density functional theory and GW schemes. *Phys. Rev. B* **85**, 235105 (2012).

53. Risko, C., McGehee, M. D. & Brédas, J.-L. A quantum-chemical perspective into low optical-gap polymers for highly-efficient organic solar cells. *Chem. Sci.* **2**, 1200–1218 (2011).

54. Zhang, L. *et al.* Calculation of band gap in long alkyl-substituted heterocyclic-thiophene-conjugated polymers with electron donor–acceptor fragment. *Sol. energy Mater. Sol. cells* **92**, 581–587 (2008).

55. Darling, S. B. Isolating the effect of torsional defects on mobility and band gap in conjugated polymers. *J. Phys. Chem. B* **112**, 8891–8895 (2008).

56. Gierschner, J., Cornil, J. & Egelhaaf, H. Optical bandgaps of π-conjugated organic materials at the polymer limit: experiment and theory. *Adv. Mater.* **19**, 173–191 (2007).

57. Yang, S., Olishevski, P. & Kertesz, M. Bandgap calculations for conjugated polymers. *Synth. Met.* **141**, 171–177 (2004).

58. Wang, J.-F. *et al.* Theoretical studies of the absorption and emission properties of the fluorene-based conjugated polymers. *Macromolecules* **37**, 3451–3458 (2004).

59. Ullah, H., Shah, A.-H. A., Bilal, S. & Ayub, K. Doping and dedoping processes of polypyrrole: DFT study with hybrid functionals. *J. Phys. Chem. C* **118**, 17819–17830 (2014).

60. Fatima *et al.* First-principles study of electron dynamics with explicit treatment of momentum dispersion on Si nanowires along different directions. *Mol. Phys.* **117**, 2293–2302 (2019).

61. Vogel, J., Inerbaev, T., Oncel, N. & Kilin, D. First-Principles Study of Charge Carrier Dynamics with Explicit Treatment of Momentum Dispersion on Si Nanowires along< 211> crystallographic Directions. *MRS Adv.* **3**, 3477–3482 (2018).

62.   Forde, A., Inerbaev, T. M., Oncel, N. & Kilin, D. S. Time-resolved Optical Properties of SiNW Oriented in< 211> Crystallographic Direction. *MRS Adv.* **4**, 2009–2014 (2019).

63.   Fatima *et al.* Photoexcited Electron Lifetimes Influenced by Momentum Dispersion in Silicon Nanowires. *J. Phys. Chem. C* **123**, 7457–7466 (2019).

64.   Cardona, M. & Peter, Y. Y. *Fundamentals of semiconductors*. (Springer, 2005).

65.   Kar, P. *Doping in conjugated polymers*. (John Wiley & Sons, 2013).

66.   Hohenberg, P. & Kohn, W. Inhomogeneous electron gas physical review 136. *B864* (1964).

67.   Kresse, G. & Furthmüller, J. Efficient iterative schemes for ab initio total-energy calculations using a plane-wave basis set. *Phys. Rev. B* **54**, 11169 (1996).

68.   Meng, Q., Chen, J. & Kilin, D. Proton reduction at surface of transition metal nanocatalysts. *Mol. Simul.* **41**, 134–145 (2015).

69.   Makov, G. & Payne, M. C. Periodic boundary conditions in ab initio calculations. *Phys. Rev. B* **51**, 4014 (1995).

70.   Neugebauer, J. & Scheffler, M. Adsorbate-substrate and adsorbate-adsorbate interactions of Na and K adlayers on Al (111). *Phys. Rev. B* **46**, 16067 (1992).

71.   Vezie, M. S. *et al.* Exploring the origin of high optical absorption in conjugated polymers. *Nat. Mater.* **15**, 746–753 (2016).

72.   Huseynova, G., Shin, E. Y., Park, W. T. & Noh, Y. Y. Lithium benzoate doped high performance n-type diketopyrrolopyrrole based organic thin-film transistors. *Dye. Pigment.* **162**, 243–248 (2019).

73.   Karpov, Y. *et al.* High Conductivity in Molecularly p-Doped Diketopyrrolopyrrole-Based Polymer: The Impact of a High Dopant Strength and Good Structural Order. *Adv. Mater.* **28**, 6003–6010 (2016).

74. Jung, I. H. *et al.* High thermoelectric power factor of a diketopyrrolopyrrole-based low bandgap polymer via finely tuned doping engineering. *Sci. Rep.* **7**, 44704 (2017).

75. Hofmann, A. I. *et al.* Chemical Doping of Conjugated Polymers with the Strong Oxidant Magic Blue. *Adv. Electron. Mater.* **6**, 1–8 (2020).

7. PHOTO-INDUCED CHARGE TRANSFER OF ORGANIC BULK HETEROJUNCTIONS VIA AB INITIO DYNAMICS

Organic conjugated polymers (CPs) are promising candidates for organic photovoltaic (OPV) devices due to their unique tunable mechanical and optoelectronic performance. Over the last decade, optoelectronic properties of narrow bandgap CPs as a blend with acceptor units are optimized mainly, leading to noticeable progress in OPV technology. However, their power conversion efficiency is still lower than their organic counterparts (i.e., silicon), limiting their practical usage. This chapter aims to employ *ab initio* molecular dynamics to explore photo-induced charge transfer (CT) of diketopyrrolopyrrole (DPP) based polymer as a blend with non-fullerene (i.e., ITIC) and fullerene (i.e., PCBM) acceptor units. Furthermore, we want to investigate whether or not the current computational approach can explore bulk heterojunctions (BHJ) electronic performance for OPV devices and narrow down the list of potential donor-acceptor candidates.[1]

7.1. Introduction

Over the past decades, the developing semiconducting CPs[2–7] has provoked noticeable progress in OPVs.[8–11] Generally, CPs are utilized as a blend with acceptor units to form the active layer's BHJ.[12] Currently, molecular engineering of CPs (i.e., donor) and acceptor units is one of the most important research directions to tune optoelectronic properties of OPVs, such as energy levels, absorption, and charge transfer (CT).[13–16] The rate of photo-induced CT at the interface of CPs and acceptors is a critical parameter that characterizes the generation/recombination of charge carriers through a non-radiative process, determining the open-circuit voltage and attained power conversion efficiency (PCE). Despite tremendous efforts, organic OPVs are still under development since they are limited to lower PCE than their inorganic counterparts. Furthermore,

due to the endless possibilities of molecular modifications and complexities of the CT mechanism, it is challenging to experimentally explore a library of donor-acceptor (D-A) blends, to reach the optimum interface.

To date, fullerene derivatives (i.e., [6,6]-phenyl-C61-butyric acid methyl ester (PCBM)) as electron acceptors are frequently implemented in high-performing OPVs devices.[17] However, the intrinsic deficiencies of fullerene-based acceptors, such as difficulty to tune energy levels, weak visible light absorption, and inherent tendency of easy aggregation, humper their improvement for OPVs devices.[18–20] Thus, non-fullerene acceptors, with synthetic flexibility and great potential to mitigate the aforementioned drawbacks of the fullerene acceptors are proposed as an alternative used in BHJ.[14] Non-fullerene acceptors have attracted a lot of attention from researchers in developing BHJ organic solar cells. It has been hypothesized that a BHJ involving non-fullerene acceptor under identical conditions will provide higher CT efficiency. Therefore, a critical prerequisite and comparative exploration must be implemented at the fundamental electronic level for both fullerene and non-fullerene CP blends to unravel the reason behind differences in the relaxation pathways CT rate at the interface. Hence, developing a computational framework to characterize/rank CT rate at the interface of different D-A blends would be noticeably advantageous for the community.

To address this, the underlying electronic ground state and formation of photo-induced CT at the interface need to be formulated.[21] Computationally efficient and precise density functional theory (DFT) techniques can be implemented to first explore the electronic structure of D-A blends.[22–24] Having DFT to provide optimized electronic states at the interface,[25] *ab initio* excited-state dynamics simulations can be implemented next to probe the mechanisms behind experimentally measured CT rates.[26] The dynamics of charge carriers are often taken into account

based on the reduced density matrix presented by the Redfield theory.[27] Then, the nonadiabatic couplings are performed to parametrize Redfield equations, from an on-the-fly coupling of the electron to lattice by the molecular dynamics trajectory developed upon DFT.[28] Recently, this methodology is successfully applied to investigate non-radiative relaxation dynamics of perovskite PVs[29–31] and silicon surfaces.[32] Hence, in this work, we employ this paradigm to investigate the CT at the interface of CPs with fullerene and non-fullerene acceptor units, seeking a materials-by-design framework to computationally narrow down the list of candidate interfaces for BHJ of OPVs.

In this work, we employ nonadiabatic molecular dynamics to investigate photo-induced CT of diketopyrrolopyrrole (DPP) based polymer[33] as a blend with non-fullerene (ITIC) and fullerene (PCBM) acceptor units. We study the non-radiative relaxation of photoexcited electrons and holes. Nonadiabatic couplings between electronic orbitals are computed based on nuclear trajectories obtained from *ab initio* calculations. We calculate the CT rates of charge carriers over time, where the difference between the CT of electron and hole can qualitatively represent the current density at zero voltage. The current density measurement at the interface of different blends is utilized to characterize the PCE qualitatively. Our study illustrates the potential of the present computational methodology to explore the performance of D-A candidates for the next generation of OPV devices.

7.2. Methods

This chapter's theoretical methods are logically organized into three sections: ground state DFT, nonadiabatic calculations, and computational details.

7.2.1. Ground State DFT

In this study, the atomic model is represented by the initial position of each ion, $\vec{R}_I$. The electronic structure is then determined through the solution of the self-consistent equation of density functional theory (DFT)[34] via Vienna Ab initio Simulation Package (VASP).[35] This approach is established based on a fictitious one-electron Kohn-Sham (KS) equation. The fundamental details of the DFT approach and exchange-correlation functionals used in this section are explained in Chapter 2.

7.2.2. Nonadiabatic Calculations

To explore CT dynamics at the interface of the conjugated polymer and acceptor unit, we utilize *ab initio* molecular dynamics (MD) with nonadiabatic couplings between nuclear and electronic degrees of freedom where the couplings provide dissipative transitions.[26,36–38] The nonadiabatic couplings are used to parameterize the Redfield theory[27] for the dynamics of the excited state. Then, dissipative electronic transitions are implemented to propagate the time evolution of the density matrix $\frac{d\rho_{ij}}{dt}$:

$$\frac{d\rho_{ij}}{dt} = \frac{-i}{\hbar} \sum_k (F_{ik}\rho_{kj} - \rho_{ik}F_{kj}) + \left(\frac{d\rho_{ij}}{dt}\right)_{diss} \tag{28}$$

where F_{ik} stands for matrix element of the KS Hamiltonian and term $\left(\frac{d\rho_{ij}}{dt}\right)_{diss}$ provides electronic energy dissipation due to a heat bath generated by electron-phonon interactions. The iterative solution of equation (28) along the MD trajectory calculates dynamic charge density distribution, rate of transitions between electronic states with corresponding orbital energy ε_i, and rate of CT at the interface. The non-equilibrium charge distribution as a function of time and energy is calculated as follows:

$$n^{(a,b)}(\varepsilon, t) = \sum_i \rho_{ii}^{(a,b)}(t)\delta(\varepsilon - \varepsilon_i) \tag{29}$$

where $n^{(a,b)}(\varepsilon, t)$ stands for the non-equilibrium charge distribution and (a, b) corresponds to the initial photoexcitation from state a to b, chosen based on the value of oscillator strength. The change in occupancy of electronic state populations from the equilibrium distribution is characterized by:

$$\Delta n^{(a,b)}(\varepsilon, t) = n^{(a,b)}(\varepsilon, t) - n^{equil}(\varepsilon) \tag{30}$$

where $n^{equil}(\varepsilon)$ stands for the equilibrium charge distribution. The $\Delta n > 0$ describes the population gain, and $\Delta n < 0$ indicates the population loss. Employing equation (30) to track the occupation of KS orbitals over time, the changes in charge distribution, as a function of z-coordinates, can be tracked as:

$$\Delta n_{CB}^{(a,b)}(z, t) = \sum_{i,j \in CB} \rho_{ij}(t) \int dx \int dy (\varphi_i^*(\vec{r})\varphi_j(\vec{r})) \tag{31}$$

$$\Delta n_{VB}^{(a,b)}(z, t) = \sum_{i,j \in VB} \rho_{ij}(t) \int dx \int dy (\varphi_i^*(\vec{r})\varphi_j(\vec{r})) \tag{32}$$

where the KS orbitals are projected onto the z-axis by integrating over x- and y-components. The energy expectation values of hot electrons (the same way for the holes) are given by:

$$\langle \Delta\varepsilon_e \rangle(t) = \sum_{i \geq LU} \rho_{ii}(t)\varepsilon_i(t) \tag{33}$$

The equation (33) equation can be rewritten in the dimensionless form of energy:

$$\langle E_e \rangle(t) = \frac{\langle \Delta\varepsilon_e \rangle(t) - \langle \Delta\varepsilon_e \rangle(\infty)}{\langle \Delta\varepsilon_e \rangle(0) - \langle \Delta\varepsilon_e \rangle(\infty)} \tag{34}$$

To calculate the rates of charge carrier relaxation to band edges, the energy expectation value is converted into dimensionless energy, and energy relaxation is fitted to a single-exponential decay to solve for the rate constant:[31]

$$k_e = \left\{ \int_0^\infty \langle E_e \rangle(t)\, dt \right\}^{-1} \tag{35}$$

Next, the expectation value of hot electron and hole position in the space can be calculated as follows:

$$\langle z^e \rangle(t) = \int dz \Delta n_{CB}^{(a,b)}(z,t)z \tag{36}$$

$$\langle z^h \rangle(t) = \int dz \Delta n_{VB}^{(a,b)}(z,t)z \tag{37}$$

where in the dimensionless form we have:

$$\langle Z^e \rangle(t) = \frac{\langle z^e \rangle(t) - \langle z^e \rangle(\infty)}{\langle z^e \rangle(0) - \langle z^e \rangle(\infty)} \tag{38}$$

$$\langle Z^h \rangle(t) = \frac{\langle z^h \rangle(t) - \langle z^h \rangle(\infty)}{\langle z^h \rangle(0) - \langle z^h \rangle(\infty)} \tag{39}$$

Finally, the total charge of the dipole over time is:

$$\langle \Delta Z \rangle(t) = \langle Z^e \rangle(t) - \langle Z^h \rangle(t) \tag{40}$$

The derivative of the total charge of the dipole over time indicates the current density that flows through the interface:

$$Current\ density(t) = j(t) = \frac{d}{dt}\langle \Delta Z \rangle(t) \tag{41}$$

where the maximum results of the current density *j(t)* over time are considered here to characterize the CT at the interface.

7.2.3. Computational Details

The periodic model of CP consists of two monomers, which are connected upon approximately 180° rotation relative to each other. This orientation is chosen to make adjacent thiophene groups more stable and preserve the linear structure of the backbone, while the same-oriented successive monomers indicated curvature of the backbone within the conjugated plane.[39] The chemical structures of CP and acceptors are generated by the Materials Studio package and

pre-optimized via force field calculations. The backbone of the CP is stretched in the y-direction. The side groups of C_6H_{13} and C_8H_{17} are grafted to both sides of the monomer. The pre-optimized structures of the acceptor units are located next to the CP in the z-direction. Before running dynamic calculations, all models are optimized by VASP to reach the ground state. For dynamics, all models are heated to a thermostat followed by MD simulations at 300K. All simulations are performed via gamma point calculations. It should be noted that our nonadiabatic calculations are computed as an average over micro canonical ensemble where MD trajectories are sampled at several hundreds of time steps to ensure representation of as many possible states that the real system might experience. Indeed, we couple electronic and nuclear degrees of freedom with adiabatic MD simulations and calculate nonadiabatic couplings between adiabatic states using an "on-the-fly" procedure. All *ab initio* MD simulations of our atomic models are performed based on PBE functionals using plane-wave basis sets.

7.3. Results

The DOS and the band structures of the ground states of the acceptor units and the CP blends are reported in Figure 7.1. To predict the bandgap which has significant importance in PV-related applications, HSE06 functional is utilized to evaluate the electronic configuration of the system. The DOS in the vicinity of the gap of DPP is exhibited in Figure 7.1A, where a bandgap of 1.29 eV is predicted, in good agreement with the reported experimental bandgap of 1.3 eV,[40], implying that HSE06 functional appropriately predicts the ground state electronic structure of the DPP. For the PCBM and ITIC acceptor units, a bandgap of 2.03 eV and 1.13 eV is predicted, respectively, see Figure 7.1B and **C**. Furthermore, as shown in Figure 7.1D, DPP:PCBM blend shows a bandgap of 1.08 eV, indicating that adding PCBM acceptor units to the DPP polymer improves charge mobility, ending in a lower bandgap compared to the pure DPP system. In the

same manner for DPP:ITIC blend, Figure 7.1E, a bandgap of 0.45 eV is predicted, much smaller than the calculated value for DPP:PCBM blend. This implies that ITIC has better potential to tune/lower the bandgap of the DPP polymer.
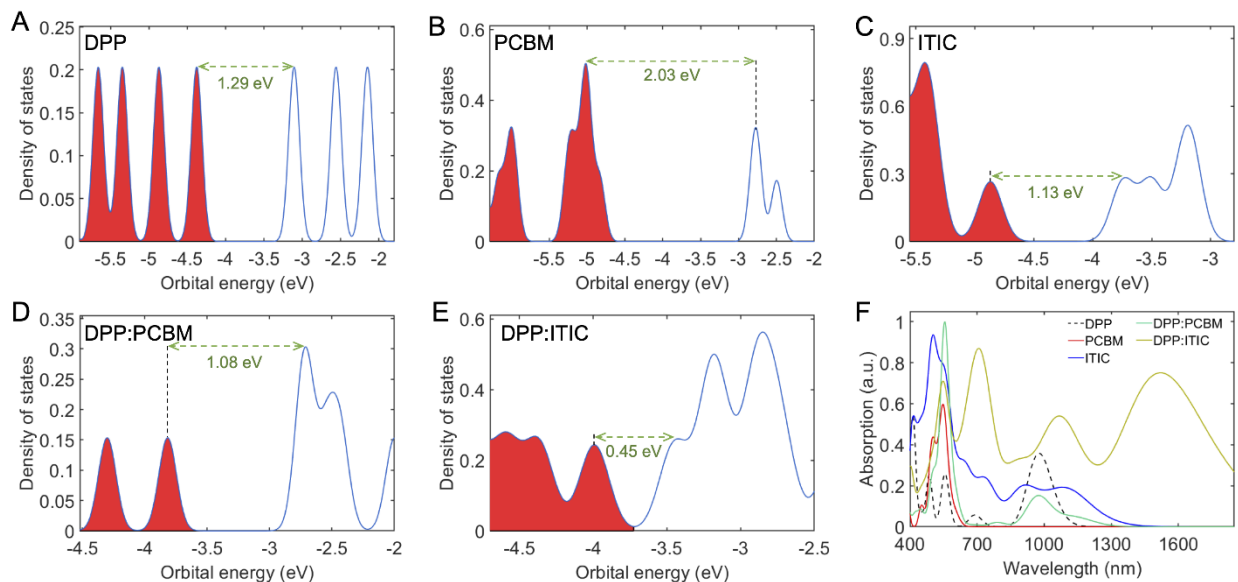
Figure 7.1. (A) Density of states (DOS) of DPP polymer model. Red shaded regions indicate the occupied orbitals and unshaded regions represent unoccupied orbitals. (B) DOS's of the PCBM standalone unit, (C) ITIC standalone unit (D) DPP:PCBM blend, and (E) DPP:ITIC blend. (F) Absorption spectrum of DPP polymer, acceptor units, and blends. Ground state calculations are performed via HSE06 functionals. Green arrows indicate bandgap.

The corresponding wavelength of fundamental absorption of semiconductors usually occurs in the visible and near IR spectral range. We evaluate the absorption spectra, Figure 7.1F, to explore the acceptor unit's influence on the DPP polymer's absorbance. For the pure DPP, the maximum absorbance (λ_p) appears around 979 nm, larger than the observed experimental value of $\lambda_p \approx 800$ nm.[41] Despite utilizing HSE06 functional, a considerable divergence in the experimental data is still observed. In our previous paper,[25] we showed that for such a 1D model, one needs to employ some numerical treatments such as k-point sampling to mitigate the discrepancy between the computational results and experimental data. As shown in Figure 7.1F,

ITIC shows more substantial absorbance than the PCBM unit, in agreement with experimental observations.[14] Accordingly, for both DPP:PCBM and DPP:ITIC, a red-shifted trend in absorption spectrum is observed, where DPP:ITIC blend exhibits much larger absorption, which no longer remains in the visible/near IR spectral range and shifts into the IR region. Jiang and coworkers[42] experimentally measured a broad photo-response from 300 nm to 900 nm for a DPP:ITIC solar cell. Our DFT calculations highlight the higher potential of the ITIC to extend the absorption spectrum of the DPP polymer into the red and near-IR range, close to solar radiation emitted by the sun at sea level.

The calculated ground state partial charge densities of the HOMO and LUMO Kohn-Sham (KS) orbitals are shown in Figure 7.2, where the HSE06 functional is employed for the DFT calculations. For the DPP:ITIC blend, Figure 7.2A, the partial charge density of the HOMO orbital resides in the DPP backbone, and this delocalized conjugated state is found to be conductive. Interestingly, the LUMO orbital of DPP:ITIC, Figure 7.2B, shows up on the ITIC acceptor unit, again delocalized through the backbone. The appearance of the HOMO on the donor and LUMO on the acceptor unit unravels the CT potential in the blend at the lower excitations. Indeed, HOMO and LUMO are considered to characterize interface energetics since these levels essentially govern charge transport and optical excitations. In the same manner for DPP:PCBM, HOMO orbital appears on the DPP backbone with a delocalized-conductive behavior, see Figure 7.2C. Accordingly, as it is exhibited in Figure 7.2D, LUMO orbital resides on the PCBM acceptor unit, which depicts the CT potential of the DPP:PCBM blend.
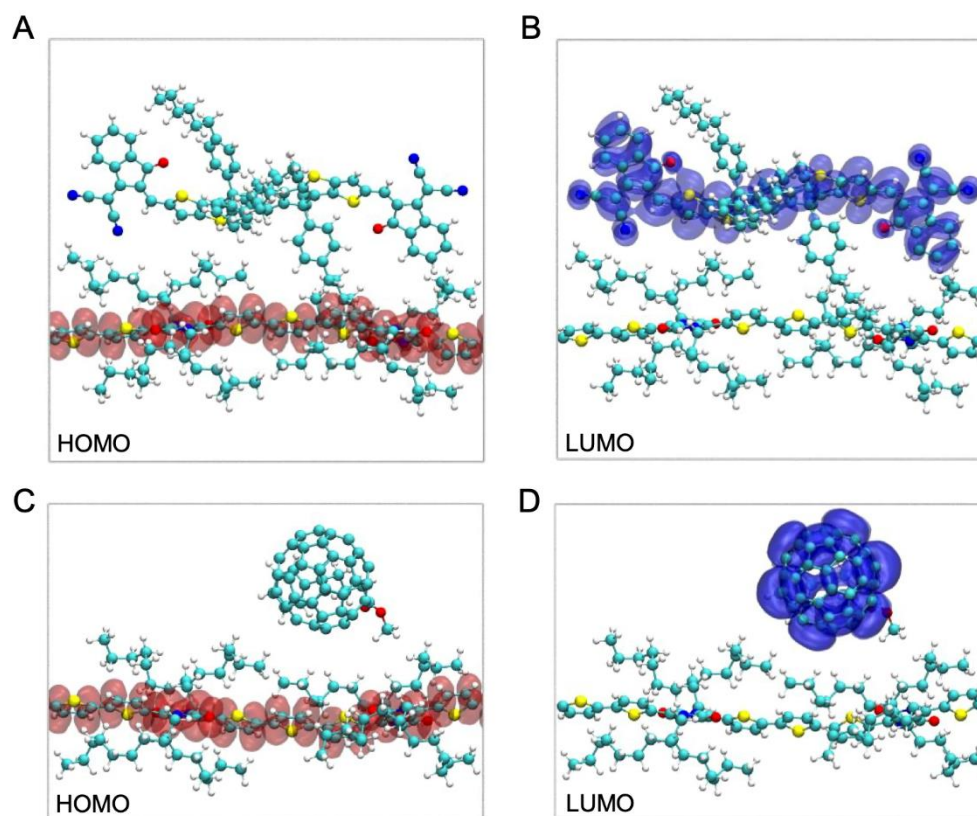
Figure 7.2. The partial charge density distribution of the HOMO and LUMO orbitals at the ground state: (A) The orbital of HOMO, for DPP:ITIC. (B) The orbital of LUMO, for DPP:ITIC. (C) The orbital of HOMO, for DPP:PCBM. (D) The orbital of LUMO, for DPP:PCBM. Shaded areas indicate the electron density. Calculations are performed via HSE06 functionals.

Figure 7.3 indicates three representative charge carrier dynamics upon photoexcitation for specific initial electronic transition for the DPP:PCBM interface with zero external electric fields. The initial transition is an instantaneous photoexcitation, which promotes a system to a non-equilibrium state by creating a hole in an initially occupied orbital and promoting an electron to an unoccupied orbital of the model. In the present study, selected transitions are characterized by high values of oscillator strengths, which are more probable to occur. All three considered transitions, Figure 7.3A-C, indicate that hole relaxation is faster than electron relaxation, and at the end of relaxation, hot electron relaxes on the PCBM acceptor unit and hot hole resides on the backbone of the DPP model. For this blend, all initial excitations start literally at PCBM, for both

electron and hole. Furthermore, for the initial excitation of $HO - 8 \rightarrow LU + 7$, Figure 7.3B, during

the initial stage of dynamics, the electron temporarily transfers to the DPP. At the later time of

relaxation, the electron returns back to the PCBM; however, such "swinging" of electrons back

and forth could be potentially undesirable for practical PV applications.

Figure 7.3. The charge carrier dynamics of DPP:PCBM blend upon photoexcitation for three representative initial transitions which possess higher oscillator strength; (A) $HO - 3 \rightarrow LU + 2$, (B) $HO - 8 \rightarrow LU + 7$, (C) $HO - 5 \rightarrow LU + 5$. For all initial transitions, both excited electron and hole are located on PCBM. The left panels indicate the distribution of charge as a function of energy and time. Dashed and solid lines indicate expectation values for energy, calculated in an energy space distribution for conduction and valence bands, respectively. Middle panels represent charge density distribution as a function of time and position in the space. Electrons, equilibrium distribution, and holes are represented in yellow, green, and blue, respectively. The offset between solid and dashed lines corresponds to the electric dipole. The periodic cell is shown in the right panels where the PCBM acceptor is located at the top and the DPP polymer at the bottom.

Figure 7.4 shows three representative charge carrier dynamics upon photoexcitation for DPP:ITIC blend. The distribution of charge as a function of time and energy following the initial photoexcitation from $HO - 4 \rightarrow LU + 2$, Figure 7.4A, shows the hole relaxation is much faster than electron relaxation. As it is demonstrated, the hole relaxes after around 0.7 ps, while the electron relaxation process starts after around 1.35 ps. The described charge carrier dynamics in space and time for the blend show that the electron relaxes on the ITIC, and holes are concentrated on the DPP backbone. The hot charge carrier dynamics for the $HO - 14 \rightarrow LU + 19$, Figure 7.4B, transition is plotted where charge distribution declares the electron relaxation takes place between 31 ps to 63 ps, while the corresponding value for hole relaxation lies around 1 ps. After complete relaxation, the charge carrier dynamics description plot in the space shows the electrons concentration on ITIC and holes concentration on DPP. For the $HO - 2 \rightarrow LU + 1$ transition, Figure 7.4C, the similar behavior is observed where the hole relaxes after 2 ps faster than electron relaxation. At this transition state, electrons reside on the ITIC while holes are concentrated on the DPP backbone. For all transitions of DPP:ITIC, initial excitations appear on both DPP and ITIC unit, implying the potential of both of them to serve as a light absorber. All excitations show the initial electron-hole pair at ITIC, where the electron stays while holes transfer to DPP. In this case, the swinging of electrons (back and forth) is less pronounced at the interface than DPP:PCBM.
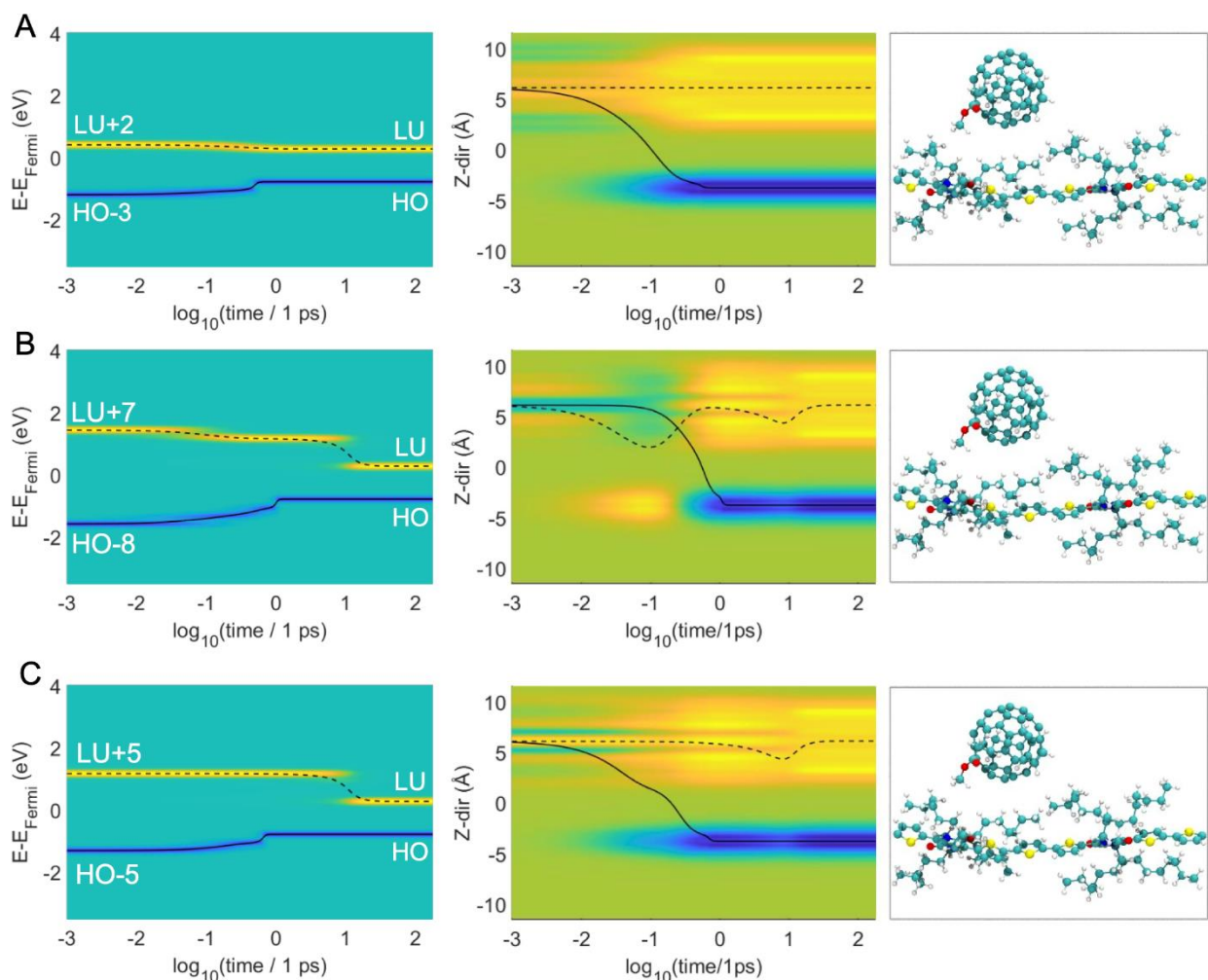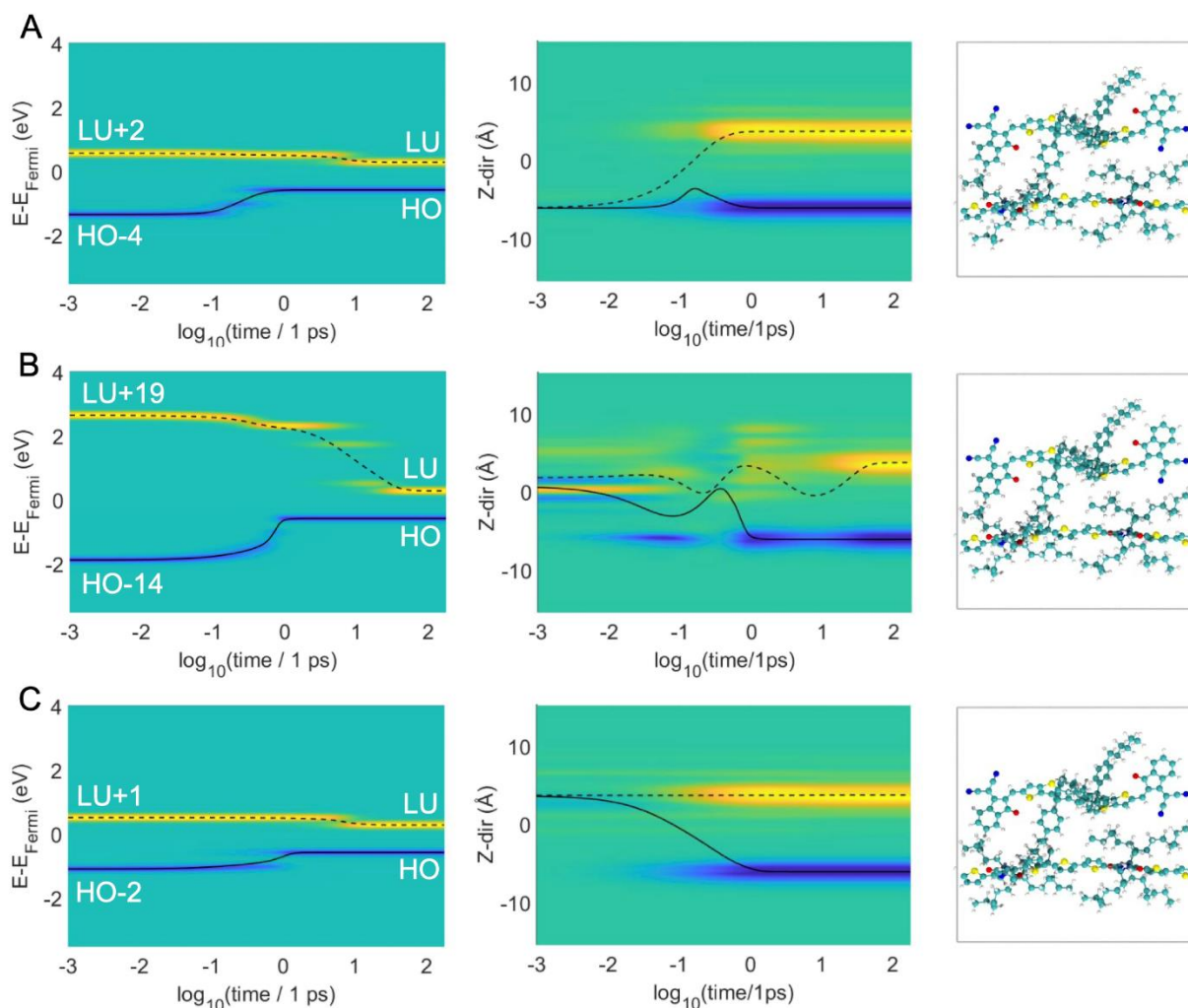
Figure 7.4. The charge carrier dynamics of DPP:ITIC blend upon photoexcitation for three representative initial transitions which possess higher oscillator strength; (A) $HO-4 \rightarrow LU+2$, (B) $HO-14 \rightarrow LU+19$, (C) $HO-2 \rightarrow LU+1$. For panel A, initial excitation appears on DPP and for panels B and C initial excitation is observed on ITIC unit. The left panels indicate the distribution of charge as a function of energy and time. Dashed and solid lines indicate expectation values for energy, calculated in an energy space distribution for conduction and valence bands, respectively. Middle panels represent charge density distribution as a function of time and position in the space. Electrons, equilibrium distribution, and holes are represented in yellow, green, and blue, respectively. The offset between solid and dashed lines corresponds to the electric dipole. The periodic cell is shown in the right panels where the ITIC acceptor is located at the top and DPP polymer at the bottom.

Furthermore, to facilitate a better understanding of the CT between donor-acceptor units, we monitor the difference between expectation values of the spatial position of the charge carriers over time (i.e., electric dipole). These calculations unravel how quickly charge carriers are being

separated. Generally, if the dipole values do not vary over time, no CT will happen at the interface and the blend would not be appropriate to be utilized in a PV device. In addition, by definition, the derivative of the dipole over time represents the current density. For DPP:PCBM system, for the transition $HO - 3 \rightarrow LU + 2$, Figure 7.5A, the inversed rate of the CT is observed at around 0.12 ps, which is an average time of transfer. It can be approximately assessed as the red line in Figure 7.5, the point where the dipole is making a halfway from the initial to the final value. For all transitions, the instant of time where half of the charge has been transferred through its way often coincides with the maximal derivative of the dipole (reported as current density). For this transition, a maximum current density of 8.47 is computed. For the transition, $HO - 8 \rightarrow LU + 7$, Figure7.5B, the inversed rate of the CT is calculated around 0.57 ps where the maximum current density of 19.08 is calculated. Eventually, $HO - 5 \rightarrow LU + 5$, Figure7.5C, transition indicate the maximum current density of 9.56. A summary of dipole and maximum current density values is reported in Table 7.1. For the DPP:PCBM interface, those three selected initial transitions exhibit an average current density of 12.37.

Figure 7.5. The dipole electric and current density of DPP:PCBM for three representative initial transitions; (A) $HO-3 \rightarrow LU+2$, (B) $HO-8 \rightarrow LU+7$, (C) $HO-5 \rightarrow LU+5$. The offset between the hot electron and hole expected position in the space corresponds to the electric dipole. Derivative of the total charge of the dipole over time indicates the current density.

Table 7.1. The values of transition energy, wavelength, electron and hole cooling rate (k_e and k_h), maximum current density, and averaged values of current density at different initial transitions of DPP:PCBM and DPP:ITIC interfaces. The maximum instantaneous value of the current density is achieved for DPP:ITIC interface, ~1.4 times larger than the one for DPP:PCBM.

Interface	Initial transition	Transition energy (eV)	Wavelength λ (nm)	k_e (1/ps)	k_h (1/ps)	*Maximum current density j(t)*
	$HO-3 \rightarrow LU+2$	1.720	720.9	2.98	2.88	8.47
	$HO-8 \rightarrow LU+7$	2.937	422.2	0.12	1.89	19.08
DPP:PCBM	$HO-5 \rightarrow LU+5$	2.686	461.5	0.09	2.41	9.56
	Average values (std)	---	---	1.06 (1.66)	2.39 (0.49)	12.37 (5.83)
	$HO-4 \rightarrow LU+2$	1.831	677.2	0.17	3.31	12.93
	$HO-14 \rightarrow LU+19$	4.655	266.35	0.09	1.77	26.75
DPP:ITIC	$HO-2 \rightarrow LU+1$	1.410	879.2	0.14	1.49	5.96
	Average values (std)	---	---	0.13 (0.04)	2.19 (0.98)	15.21 (10.58)

160

The dipole and current density of DPP:ITIC blend over time are reported in Figure 7.6. As it is shown in Figure 7.6A, the transition $HO - 4 \rightarrow LU + 2$ exhibits an inversed rate of the CT around 0.2 ps and a maximum current density of 12.93. For this transition, both DPP and ITIC can serve as efficient light absorbers. The transition $HO - 14 \rightarrow LU + 19$, Figure 7.6B, implies an inversed rate of the CT around 0.87 ps and maximum current density of 26.75. Finally, for the transition $HO - 2 \rightarrow LU + 1$, Figure 7.6C, inversed rate of the CT is calculated around 0.29 ps where maximum current density exhibits a value of 5.65. As it is summarized in Table 7.1, an average value of 15.21 is calculated for the three aforementioned transitions of DPP:ITIC blend. This averaged current density value of DPP:ITIC interface is higher than the 12.37 value of DPP:PCBM, implying the potential of the ITIC acceptor unit to provide more efficient CT than the PCBM unit.
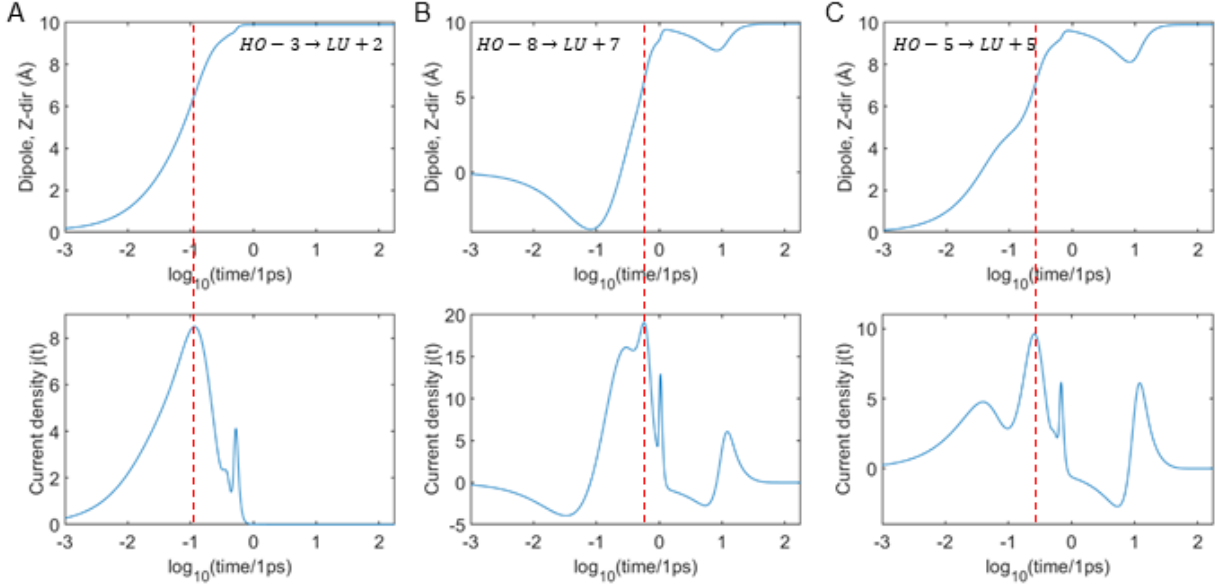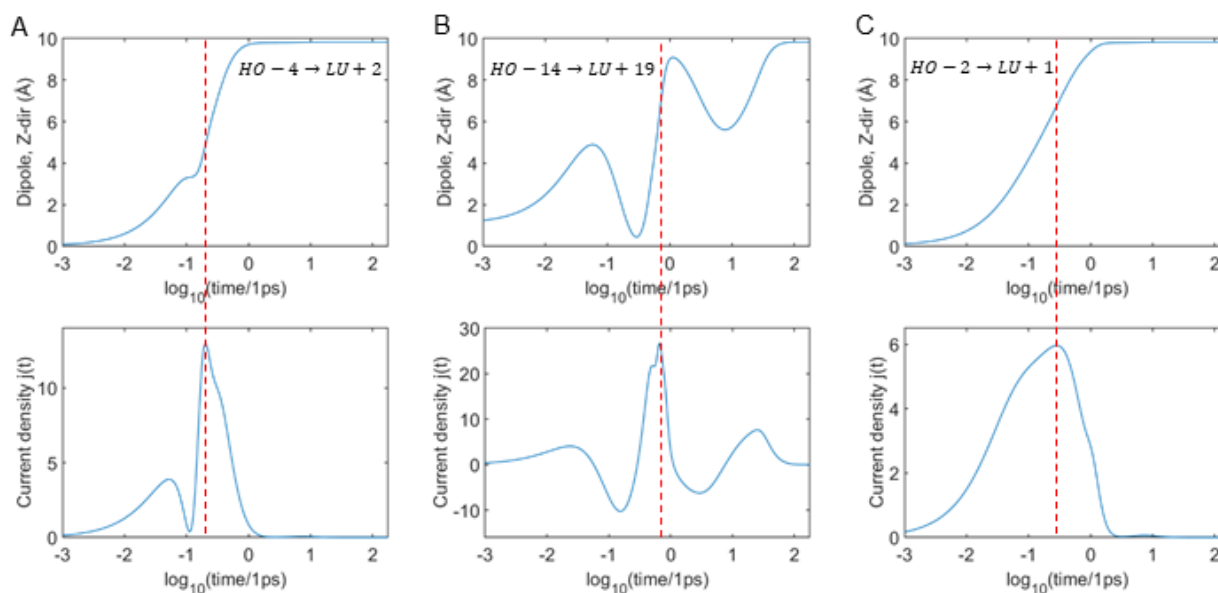

Figure 7.6. The dipole electric and current density of DPP:ITIC for three representative initial transitions; (A) $HO - 4 \rightarrow LU + 2$, (B) $HO - 14 \rightarrow LU + 19$, (C) $HO - 2 \rightarrow LU + 1$. The offset between the hot electron and hole expected position in the space corresponds to the electric dipole. Derivative of the total charge of the dipole over time indicates the current density.

7.4. Discussion

Engineered interfaces between organic conjugated materials are of great importance for PV devices' function and efficiency, where understanding the interface properties will facilitate the development of the next generation of OPVs. According to previous studies, CPs as a blend with non-fullerene acceptor units indicate an improved power conversion efficiency in BHJ solar cells compared to fullerene-based interfaces. Here, our first principle calculations allow interpreting both ground state static observables and dynamics CT at the interface of both non-fullerene and fullerene blends at a fundamental electronic level. Under the same condition, the ITIC acceptor indicates stronger absorbance than PCBM; consequently, the combined absorbance of the DPP:ITIC captures preferable regions of the solar spectrum to achieve enhanced light-harvesting ability. The bandgap of DPP:ITIC is found to be noticeably smaller than DPP:PCBM, which is more favorable for OPVs since a smaller bandgap maximizes PCE.

For the CPs as long-chain molecules, our results indicate the formation of delocalization HOMO orbital along with the conjugated backbone, which can form one-dimensional bands and facilitate the mobility of charge carriers. On the other hand, for the electron acceptors, a delocalized LUMO orbital on the ITIC unit similarly offers a preferable circumstance for the proper charge carriers' mobility. Interestingly, mobility is expected to contribute to mobility. This delocalized state on the ITIC fused-ring structure can easily form π-π stacking with aromatic rings of the DPP's backbone (i.e. where the delocalized HOMO resides) which advantageously facilitates CT.[14] On the contrary, for DPP:PCBM interface, despite the localization of the LUMO orbital on the buckyball of the PCBM unit, the cage-like fused-ring structure of the acceptor unit cannot provide an optimized interface (i.e., to facilitate CT) with DPP for the CT compared to ITIC. The organic BHJ devices need to possess an increased interface between donor and acceptor for charge

separation to address the limitations due to low exciton diffusion lengths in organic materials.[12,43–46] This increased area of interface between the donor and acceptor directly improves solar cell efficiencies suggesting a preferable charge separation throughout the BHJ.

For both DPP:PCBM and DPP:ITIC interfaces, nonadiabatic couplings indicate that electrons and holes have fast sub-picosecond carrier cooling. For all initial transitions, expectedly, the photoexcited electrons exhibit a long decay of hot carriers near the LUMO state. This is due to a large nonresonant sub gap above the conduction band edge and the transitions between electronic levels, experiencing a phonon bottleneck mechanism.[47,48] On the contrary, hole levels in the valence band, are often spaced more densely, and the transition between electronic levels is quicker since there are a lot of nuclear phonon modes in resonance with them. A similar trend is observed by Hamada and coworkers,[49] in which time-resolved microwave conductivity (TRMC) measurements show a slower relaxation for the electrons compared to the holes in non-Fullerene acceptor solar cells.

In addition, our calculations on the dynamics of charge carriers indicate that, under the same condition, changing the acceptor unit from PCBM to ITIC induces drastic qualitative changes in the pattern of CT at the interface of studied organic blends. There are three critical observations from these dynamics calculations: (I) The amount of the charge transferred at the DPP:ITIC interface is higher than DPP:PCBM at several probable excitations scenarios due to a more optimized interface to form π-π stacking. (II) CT at the DPP:ITIC interface is more stable and the swinging of the charge carriers is less pronounced. (III) For DPP:ITIC blend the initial excitation observed on both donor and acceptor units; alternatively, both DPP and ITIC can serve as light absorbers. For this blend, multiple channels of CT lead to a generation of charge separation as a prerequisite for efficient PV cells.

7.5. Conclusion

In this study, we utilize density functional theory (DFT) and density matrix theory to provide an insightful understanding of the optoelectronic properties of fullerene vs non-fullerene acceptors which are currently a major focus of the semiconductor's community. The key structure-property relationships and donor-acceptor matching properties are investigated. We explore the patterns of photo-induced charge transfer (CT) of diketopyrrolopyrrole (DPP) based polymer as a blend with non-fullerene (ITIC) and fullerene (PCBM) acceptor units. DPP:ITIC blend exhibits stronger near-IR absorption compared to DPP:PCBM system. For both models, the partial charge density of the HOMO orbitals appears on the CP backbone, while for LUMO it resides on the acceptor units, implying the potential for the donor-acceptor CT. The delocalized partial charges on both DPP (i.e., donor) and ITIC (i.e., acceptor unit) is preferable to form π-π stacking and indicate a more favorable circumstance for the CT. The non-radiative dynamics of photoexcited charge carriers indicate that hole relaxation in energy and space is faster than electron relaxation. Furthermore, we establish a predictive computational framework to qualitatively characterize the power conversion efficiency (PCE) of different blends based on transfer rates of charge carriers over time, i.e., difference between the transfer rate of electron and hole that represent the current density at zero voltage. CT rate calculations indicate that CPs blend with ITIC offers a better PV effect compared to PCBM-based blend. Our first principle calculations indicate that for DPP:ITIC system, CT is faster, swinging of charge carriers is less dominant, and both DPP and ITIC can serve as light absorbers. Our results demonstrate the efficacy of the current approach as a computational design strategy to assess fundamental optoelectronic properties and CT capability of the newly designed donor-acceptor organic blends before any synthesis process, which would be advantageous for the development of the next generation of organic photovoltaics (OPVs).

7.6. References

1. Alesadi, A., Xia, W. & Kilin, D. Photo-Induced Charge Transfer of Fullerene and Non-Fullerene Conjugated Polymer Blends via Ab Initio Excited-State Dynamics. *J. Phys. Chem. C* **126**, 12015–12024 (2022).

2. Mei, J., Diao, Y., Appleton, A. L., Fang, L. & Bao, Z. Integrated materials design of organic semiconductors for field-effect transistors. *J. Am. Chem. Soc.* **135**, 6724–6746 (2013).

3. Sirringhaus, H. 25th anniversary article: Organic field-effect transistors: The path beyond amorphous silicon. *Adv. Mater.* **26**, 1319–1335 (2014).

4. Sirringhaus, H., Tessler, N. & Friend, R. H. Integrated optoelectronic devices based on conjugated polymers. *Science (80-.).* **280**, 1741–1744 (1998).

5. Zhang, S. *et al.* Molecular Origin of Strain-Induced Chain Alignment in PDPP-Based Semiconducting Polymeric Thin Films. *Adv. Funct. Mater.* **31**, 2100161 (2021).

6. Zhang, S. *et al.* Toward the Prediction and Control of Glass Transition Temperature for Donor–Acceptor Polymers. *Adv. Funct. Mater.* **2002221**, 2002221 (2020).

7. Alesadi, A. *et al.* Machine learning prediction of glass transition temperature of conjugated polymers from chemical structure. *Cell Reports Phys. Sci.* 100911 (2022).

8. Zhan, X. & Zhu, D. Conjugated polymers for high-efficiency organic photovoltaics. *Polym. Chem.* **1**, 409–419 (2010).

9. Saito, M., Ohkita, H. & Osaka, I. π-Conjugated polymers and molecules enabling small photon energy loss simultaneously with high efficiency in organic photovoltaics. *J. Mater. Chem. A* **8**, 20213–20237 (2020).

10.   Fan, B. *et al.* Tailoring regioisomeric structures of π-conjugated polymers containing monofluorinated π-bridges for highly efficient polymer solar cells. *ACS Energy Lett.* **5**, 2087–2094 (2020).

11.   Li, Y. Molecular design of photovoltaic materials for polymer solar cells: Toward suitable electronic energy levels and broad absorption. *Acc. Chem. Res.* **45**, 723–733 (2012).

12.   Yu, G., Gao, J., Hummelen, J. C., Wudl, F. & Heeger, A. J. Polymer photovoltaic cells: enhanced efficiencies via a network of internal donor-acceptor heterojunctions. *Science (80-.).* **270**, 1789–1791 (1995).

13.   Choi, J., Kim, W., Kim, S., Kim, T. S. & Kim, B. J. Influence of Acceptor Type and Polymer Molecular Weight on the Mechanical Properties of Polymer Solar Cells. *Chem. Mater.* (2019). doi:10.1021/acs.chemmater.9b03333

14.   Lin, Y. *et al.* An electron acceptor challenging fullerenes for efficient polymer solar cells. *Adv. Mater.* **27**, 1170–1174 (2015).

15.   Yang, Y. *et al.* Side-Chain Isomerization on an n-type Organic Semiconductor ITIC Acceptor Makes 11.77% High Efficiency Polymer Solar Cells. *J. Am. Chem. Soc.* **138**, 15011–15018 (2016).

16.   Doumon, N. Y. *et al.* Photostability of Fullerene and Non-Fullerene Polymer Solar Cells: The Role of the Acceptor. *ACS Appl. Mater. Interfaces* **11**, 8310–8318 (2019).

17.   He, Y. & Li, Y. Fullerene derivative acceptors for high performance polymer solar cells. *Phys. Chem. Chem. Phys.* **13**, 1970–1983 (2011).

18.   Zhao, W. *et al.* Fullerene-free polymer solar cells with over 11% efficiency and excellent thermal stability. *Adv. Mater.* **28**, 4734–4739 (2016).

19. Hou, J., Inganäs, O., Friend, R. H. & Gao, F. Organic solar cells based on non-fullerene acceptors. *Nat. Mater.* **17**, 119–128 (2018).

20. Yan, C. *et al.* Non-fullerene acceptors for organic solar cells. *Nat. Rev. Mater.* **3**, 1–19 (2018).

21. Han, Y., Micha, D. A. & Kilin, D. S. Ab initio study of the photocurrent at the Au/Si metal-semiconductor nanointerface. *Mol. Phys.* **113**, 327–335 (2015).

22. Moussa, J. E., Schultz, P. A. & Chelikowsky, J. R. Analysis of the Heyd-Scuseria-Ernzerhof density functional parameter space. *J. Chem. Phys.* **136**, 204117 (2012).

23. Sholl, D. & Steckel, J. A. *Density functional theory: a practical introduction*. (John Wiley & Sons, 2011).

24. Perdew, J. P., Burke, K. & Ernzerhof, M. Generalized gradient approximation made simple. *Phys. Rev. Lett.* **77**, 3865 (1996).

25. Alesadi, A., Fatima, F., Xia, W. & Kilin, D. First-Principles Study on the Electronic Properties of PDPP-Based Conjugated Polymer via Density Functional Theory. *J. Phys. Chem. B* **125**, 8953–8964 (2021).

26. Forde, A. & Kilin, D. Hole transfer in dye-sensitized cesium lead halide perovskite photovoltaics: Effect of interfacial bonding. *J. Phys. Chem. C* **121**, 20113–20125 (2017).

27. Redfield, A. G. On the theory of relaxation processes. *IBM J. Res. Dev.* **1**, 19–31 (1957).

28. Hammes-Schiffer, S. & Tully, J. C. Proton transfer in solution: Molecular dynamics with quantum transitions. *J. Chem. Phys.* **101**, 4657–4667 (1994).

29. Han, Y. & Kilin, D. S. Nonradiative Relaxation Dynamics of a Cesium Lead Halide Perovskite Photovoltaic Architecture: Effect of External Electric Fields. *J. Phys. Chem. Lett.* **11**, 9983–9989 (2020).

30. Forde, A., Inerbaev, T. & Kilin, D. Spectral Signatures of Positive and Negative Polarons in Lead-Halide Perovskite Nanocrystals. *J. Phys. Chem. C* **124**, 1027–1041 (2019).

31. Forde, A., Inerbaev, T., Hobbie, E. K. & Kilin, D. S. Excited-State Dynamics of a CsPbBr3 Nanocrystal Terminated with Binary Ligands: Sparse Density of States with Giant Spin-Orbit Coupling Suppresses Carrier Cooling. *J. Am. Chem. Soc.* **141**, 4388–4397 (2019).

32. Han, Y. *et al.* Hot Carrier Dynamics at Ligated Silicon(111) Surfaces: A Computational Study. *J. Phys. Chem. Lett.* **12**, 7504–7511 (2021).

33. Chen, H. *et al.* Highly π-Extended Copolymers with Diketopyrrolopyrrole Moieties for High-Performance Field-Effect Transistors. *Adv. Mater.* **24**, 4618–4622 (2012).

34. Hohenberg, P. & Kohn, W. Inhomogeneous electron gas physical review 136. *B864* (1964).

35. Kresse, G. & Furthmüller, J. Efficient iterative schemes for ab initio total-energy calculations using a plane-wave basis set. *Phys. Rev. B* **54**, 11169 (1996).

36. Chen, J., Schmitz, A. & Kilin, D. S. Computational simulation of the p-n doped silicon quantum dot. *Int. J. Quantum Chem.* **112**, 3879–3888 (2012).

37. Kilin, D. S. & Micha, D. A. Relaxation of photoexcited electrons at a nanostructured Si (111) surface. *J. Phys. Chem. Lett.* **1**, 1073–1077 (2010).

38. Han, Y., Micha, D. A. & Kilin, D. S. Ab initio study of the photocurrent at the Au/Si metal–semiconductor nanointerface. *Mol. Phys.* **113**, 327–335 (2015).

39. Vezie, M. S. *et al.* Exploring the origin of high optical absorption in conjugated polymers. *Nat. Mater.* **15**, 746–753 (2016).

40. Bijleveld, J. C. *et al.* Poly (diketopyrrolopyrrole− terthiophene) for Ambipolar Logic and Photovoltaics. *J. Am. Chem. Soc.* **131**, 16616–16617 (2009).

41. Hofmann, A. I. *et al.* Chemical Doping of Conjugated Polymers with the Strong Oxidant Magic Blue. *Adv. Electron. Mater.* **6**, 1–8 (2020).

42. Jiang, X. *et al.* Non-fullerene organic solar cells based on diketopyrrolopyrrole polymers as electron donors and ITIC as an electron acceptor. *Phys. Chem. Chem. Phys.* **19**, 8069–8075 (2017).

43. Waldauf, C., Scharber, M. C., Schilinsky, P., Hauch, J. A. & Brabec, C. J. Physics of organic bulk heterojunction devices for photovoltaic applications. *J. Appl. Phys.* **99**, 104503 (2006).

44. Halls, J. J. M. *et al.* Efficient photodiodes from interpenetrating polymer networks. *Nature* **376**, 498–500 (1995).

45. Kannan, B., Castelino, K. & Majumdar, A. Design of nanostructured heterojunction polymer photovoltaic devices. *Nano Lett.* **3**, 1729–1733 (2003).

46. Haugeneder, A. *et al.* Exciton diffusion and dissociation in conjugated polymer/fullerene blends and heterostructures. *Phys. Rev. B* **59**, 15346 (1999).

47. Urayama, J., Norris, T. B., Singh, J. & Bhattacharya, P. Observation of phonon bottleneck in quantum dot electronic relaxation. *Phys. Rev. Lett.* **86**, 4930 (2001).

48. Kilina, S. V, Neukirch, A. J., Habenicht, B. F., Kilin, D. S. & Prezhdo, O. V. Quantum zeno effect rationalizes the phonon bottleneck in semiconductor quantum dots. *Phys. Rev. Lett.* **110**, 180404 (2013).

49. Hamada, F. & Saeki, A. Mobility Relaxation of Holes and Electrons in Polymer:Fullerene and Polymer : Non-Fullerene Acceptor Solar Cells. *ChemSusChem* **14**, 3528–3534 (2021).

8. CONCLUSION AND FUTURE OUTLOOKS

In the previous chapters, we reported the results of our studies on thermomechanical properties and optoelectronics of conjugated polymers (CPs) and organic bulk heterojunctions (BHJ). In this chapter, we summarize our findings and their impacts on the development of CPs and then review the possible lines for future research. Then, a list of the publications derived from this work is reported at the end of this chapter.

8.1. Summary

The computational works presented in this dissertation, aimed to provide a deep understanding of glass transition behavior, mechanical performance, and optoelectronic properties of CPs. At first, we want to emphasize the extensive experiments, multiscale modeling, and data-driven approaches that have been utilized in this study. In Chapter 2, we introduced multiscale modeling frameworks that are used in this dissertation. We first reviewed the classical molecular dynamics (MD) simulation method and relevant computational details. For all atomistic (AA)-MD simulations, we employ the general Amber force field (GAFF), which is mainly developed for organic molecules and can be an ideal choice for the simulation of organic CPs. To conduct a parametric study on the influence of different molecular parameters, such as chain rigidity and grafting density on the thermomechanical properties of CPs, we utilize generic coarse-grained (CG)-MD simulations, where the force field components are introduced in Chapter 2. Finally, density functional theory (DFT) approaches are employed to explore the optoelectronic properties of CPs.

Having CG-MD models, we studied the glass-transition behavior of polydiketopyrrolopyrrole (PDPP)-based CPs in Chapter 3, where new models for predicting glass transition temperature (T_g) of side-chain-engineered CPs were reported. Our CG-MD simulation

examined and validated the experimental observations on the side-chain length dependence of polymer T_g, and provided insights into the influence of side-chain group and grafting density on chain mobility. Both experimental and simulation results reported highlighted the role of side chains on the T_g in which increasing side-chain length showed a decreasing influence on T_g. We expect these methods to guide the application-driven materials-by-design for CPs via molecular engineering, i.e., high T_g and stiff polymers, low T_g and soft polymers. We believe our study shed light on the future development of newly engineered CPs with tailored thermal performance.

In Chapter 4, we developed an integrated data-driven study to predict T_g of CPs directly from the geometry of the repeat unit. Despite the critical role of T_g in the applicability of the CPs, it is very challenging to predict T_g of CPs due to the heterogeneous nature of CPs' chain architectures and diverse chemical building blocks. In this chapter, we presented a predictive modeling framework to predict T_g for a wide range of CPs through the integration of machine learning (ML), AA-MD simulations, and experiments. With nearly 154 T_g data collected from experiments and simulations, a predictive model based on ML was developed by taking simplified "geometry" of six chemical structures (i.e., side-chain fraction, isolated rings, fused rings, bridged rings, double/triple bonds, and halogen atoms) as input molecular features. Among those features, we identified side-chain fraction, isolated rings, fused rings, and bridged rings features as the dominant factors for T_g. MD simulations were then performed to unravel the fundamental roles of those chemical building blocks in dynamical heterogeneity and local mobility of CP chains at a molecular level, supported by the quasielastic neutron scattering (QENS) experiment. The simulations revealed that aromatic rings and side chains have the highest and lowest local mobility, unraveling their dominant role in the ML model. Remarkably, the developed ML model was demonstrated for its capability to predict T_g's of several new high-performance solar cell materials

to a good approximation. The established predictive framework would be an essential milestone for the design and prediction of T_g of complex CPs, paving the way for addressing device stability issues that have hampered the field from developing stable organic electronics.

Chapter 5 focused on the mechanical properties of CPs and their deformation mechanism under tensile strain. We systematically investigated the mechanical properties and chain deformation mechanism of PDPP-based CPs and the thermomechanical-structure-property-morphology performance relationships based on experimental measurements and CG-MD simulations. Our CG-MD simulations and experimental techniques indicated the reducing influence of the side-chain length on the elastic modulus, in which elastic modulus and T_g were found linearly correlated. CG-MD simulations showed more significant alignment parameter values for the side chain at higher strains, compared to backbones orientation, due to the differences in the rigidity of the backbones compared to the side chains of CPs. Next, detailed molecular orientation analysis found macroscopic thin-film deformation closely correlated with their microscopic origin. Two primary strain-induced deformation mechanisms were addressed: highly oriented crystalline domains and substantial chain slippage in the amorphous domain. The lamellar rotation was identified to be the main alignment pathway for crystallites, in which the backbone orientation was much lower due to the nonlinearity of PDPP chains. The backbone rotation was identified to be part of the whole chain deformation, with their aromatic planes rotated towards the parallel-to-strain direction. We believe the fundamental understanding of the chain deformation mechanism reported in Chapter 5 for PDPP-based polymers can facilitate the application of semi-rigid CPs stretchable electronic devices.

In Chapter 6, we employed quantum mechanics simulations to probe the optoelectronic properties of PDPP-based CPs under excitation. Optoelectronic properties influenced by charge

172

injection or doping are crucial to control the charge carrier mobility in organic semiconductors. This chapter focused on first-principle methods to predict the bandgap and absorption spectrum of CPs. These properties were explored as a function of electronic configurations, including modeling of injection and withdrawing electrons. We utilized Heyd-Scuseria-Ernzerhof (HSE06) and Perdew-Burke-Ernzerhof (PBE) functionals to predict the band gap and compute the absorption spectrum of DPP-based CPs (or PDPP3T). Our DFT results pointed out that utilizing the HSE06 functional in conjunction with k-point sampling of the Brillouin zone can appropriately predict the bandgap and absorption spectrum of the PDPP3T in good agreement with experimental data. Moreover, we explored the influence of doping, i.e., mimicking n-type and p-type doping by injecting and withdrawing electrons, on the electronic properties of these polymer models. Our results indicated that the injection of charge carriers into the PDPP3T polymer model greatly affects the electrical properties ended in a low bandgap and high-mobility PDPP3T polymers, offering the potential to tailor the material electronic performance for organic photovoltaic and optoelectronic device applications.

Finally, in Chapter 7, we studied photovoltaic (PV) performance and charge carrier dynamics of CPs as a blend with organic acceptor molecules. Although the optoelectronic properties of narrow bandgap CPs as a blend with acceptor units have been significantly optimized, their power conversion efficiency (PCE) is still lower than their organic counterparts (i.e., silicon), limiting their practical usage. In this chapter, we employed *ab initio* excited state dynamics to explore photo-induced charge transfer (CT) of PDPP-based CPs as a blend with non-fullerene (i.e., ITIC) and fullerene (i.e., PCBM) acceptor units. The results of charge carrier dynamics induced by selected photoexcitation showed that hole density redistribution in space is much faster than electron relaxation. We then tracked the relaxation rates of charge carriers over time, where the

derivative of the difference between the rate of electron and hole can qualitatively represent the current density at zero voltage. This can be utilized to characterize the CT performance of CPs blended with different acceptor units. Relaxation rate results indicated that CPs blend with ITIC offers a better PV performance, illustrating the potential of our approach to explore bulk heterojunctions (BHJ) electronic performance for OPV devices and narrowing down the list of potential donor-acceptor candidates.

8.2. Outlook into Future

After reviewing our significant findings in this section, we want to discuss the limitations and future directions of multiscale molding and data-driven approaches used in this dissertation and suggest potential opportunities to improve the current guidelines for developing the next generation of CPs.

First, generic CG-MD simulations utilized in this dissertation do not have a specific understanding of polymer chain chemistry. Although this generic CG modeling has been successful in the parametric study of CPs, it also revealed clear limitations in providing quantitative prediction of the physical properties. This limitation provokes the idea of developing chemically specific transferable CG-MD models for CPs that can benefit the polymer community. Chemically specific CG models can provide quantitative property calculation at much larger lengths and time scales while preserving computational efficiency. This modeling strategy enables probing the dynamics of the polymer systems up to several hundred nanoseconds which is not accessible by AA-MD simulations.

Next, AA-MD simulations developed upon GAFF showed a reliable performance and appropriate accuracy to predict T_g of CPs, in good agreement with experimental measurements. GAFF utilized in this study showed the capability of capturing essential structural features of CPs

chains such as alkyl side chains and backbone moieties (e.g., addition of thiophene rings to the backbone of the repeat unit). However, there is more potential for the application of GAFF and AA-MD to characterize T_g of CPs. In this dissertation, Chapter 4, we calculate T_g of nearly 20 CPs and organic acceptor molecules via AA-MD, and results showed good agreement with experimental data. However, due to the endless possibility of molecular modifications still, there are many newly designed CPs whose their T_g is still unknown, and AA-MD models can play a vital role in characterizing these materials' glass transition behavior.

Moreover, in Chapter 4, we employed AA-MD simulations to calculate segmental dynamics of building blocks to unravel the role of mobility of different chemical elements on the T_g. The results of segmental dynamics were impressive when compared to neutron scattering technique and ML outputs. This reliable computational measurement provokes the idea of investigating further the morphology and chain conformation of CPs via AA-MD via GAFF force field. In particular, the role of segmental dynamics on the morphology of the CPs as a blend with acceptor units is still less investigated. AA-MD simulations can play an important role in calculating critical structural-molecular properties such as segmental mobility, $\pi-\pi$ stacking, and dihedral distribution to address this critical issue.

Next, we used previously published literature, our experimental measurements, and AA-MD simulations to collect a diverse dataset for the data-driven approach utilized in this dissertation. We want to highlight again that a sufficient volume of high-quality data is vital to train an ML model effectively. The data available in the field of CPs is much less compared to non-conjugated polymers, and this shortage of data can potentially make any data-based prediction less accurate. To the best of our knowledge, the dataset that we collected to train our ML model for T_g prediction is the most complete and diverse one reported yet. However, we admit that our

dataset has room for improvement to have a more unbiased and accurate prediction. For example, as discussed in Chapter 4, minimal reliable data points have been reported for some molecular features in our CPs dataset, e.g., halogen atoms. Thus, the ML model trained to those limited data points may be biased and not generalize new or out-of-sample CPs composed of halogen atoms. However, we believe the ML framework that we established in this study has the potential to be improved upon the availability of larger T_g dataset of CPs in the future. Moreover, the ML model proposed in this dissertation just focused on the structure-property relationship of CPs and can make property calculations while the chemical structure of the repeat unit is available. However, reversed design-based structure-property computational tools will be greatly advantageous for the development of CPs. Indeed, using more complex ML approaches such as neural networks, predictive models can be developed to take the property of interest (e.g., T_g and band gap) as the input and propose the chemical structure of the monomer. As of now, CPs are being designed mainly based on the empirical rules from classical polymer physics. Therefore, developing a rational design platform based on physically-informed ML techniques to suggest potential chemical structures suitable for specific physical properties will ease the design of new CPs.

Finally, for the quantum simulations that we performed to characterize the PV performance and CT in Chapter 7, despite the insightful observation of the charge carrier dynamics, we want to admit that the geometries of our computational models are idealized to overcome the computational cost. One challenging follow-up project can be developing condensed 3-dimensional periodic models of organic BHJ to sample multiple CT interfaces between donor and acceptor units and enhance the reliability of the simulations. We believe packing multiple donor and acceptor units in a condensed simulation cell based on the experimentally recommended D-A weight ratio will provide more insightful computational models to explore CT.

8.3. List of Publications

Most of the materials presented in this dissertation were previously published in peer-reviewed journals. The readers are directed to those articles for further details that may have been omitted in advocacy for clarity and simplicity of this presentation. A list of the relevant publications is presented below:

1. **Alesadi, A**., Cao, Z., Li, Z., Zhang, S., Zhao, H., Gu, X. and Xia, W., 2022. Machine learning prediction of glass transition temperature of conjugated polymers from chemical structure. *Cell Reports Physical Science*, p.100911.

2. **Alesadi, A**., Xia, W. and Kilin, D., 2022. Photo-Induced Charge Transfer of Fullerene and Non-Fullerene Conjugated Polymer Blends via Ab Initio Excited-State Dynamics. *The Journal of Physical Chemistry C*, 126(29), pp.12015-12024. (**cover article**)

3. **Alesadi, A**., Fatima, F., Xia, W. and Kilin, D., 2021. First-Principles Study on the Electronic Properties of PDPP-Based Conjugated Polymer via Density Functional Theory. *The Journal of Physical Chemistry B*, 125(31), pp.8953-8964. (**cover article**)

4. Zhang, S., **Alesadi, A**., Mason, G.T., Chen, K.L., Freychet, G., Galuska, L., Cheng, Y.H., St. Onge, P.B.J., Ocheje, M.U., Ma, G. and Qian, Z., 2021. Molecular Origin of Strain‑Induced Chain Alignment in PDPP‑Based Semiconducting Polymeric Thin Films. *Advanced Functional Materials*, 31(21), p.2100161.

5. Karuth, A., **Alesadi, A**., Xia, W. and Rasulev, B., 2021. Predicting glass transition of amorphous polymers by application of cheminformatics and molecular dynamics simulations. *Polymer*, 218, p.123495. (***contributed equally**)

6. Zhang, S., **Alesadi, A**., Selivanova, M., Cao, Z., Qian, Z., Luo, S., Galuska, L., Teh, C., Ocheje, M.U., Mason, G.T. and St. Onge, PBJ, 2020. Toward the prediction and control of glass transition temperature for donor–acceptor polymers. *Advanced Functional Materials*, 30(27), p.2002221. (***contributed equally**)

7. **Alesadi, A**. and Xia, W., 2020. Understanding the role of cohesive interaction in mechanical behavior of a glassy polymer. *Macromolecules*, 53(7), pp.2754-2763.